Impact of longwave enhancement by forests on snow cover in a global climate model

Markus Todt

A thesis submitted in partial fulfilment of the requirements of the University of Northumbria at Newcastle for the degree of Doctor of Philosophy

Research undertaken in the Department of Geography, Faculty for Engineering and Environment

January 2019

Abstract

Boreal forests cover about a fifth of seasonally snow-covered land over the Northern Hemisphere. Skill in modelling snow cover has been shown to be lower for forested than for open areas, which was attributed to more complex processes in forests. One of these processes is the enhancement of longwave radiation beneath forest canopies, which has been found to impact the surface energy balance and rates of snowmelt. Single-layer vegetation schemes, as used in the Community Land Model version 4.5 (CLM4.5), have been found to overestimate diurnal cycles in vegetation temperature and sub-canopy longwave radiation. However, simulation of longwave enhancement and its impact on snow cover has not yet been assessed in a global climate model. Forest stand-scale forcing was used for the simulation of sub-canopy longwave radiation by CLM4.5 and to drive SNOWPACK, a snow model featuring a two-layer canopy module, as a benchmark model for CLM4.5. Simulated sub-canopy longwave radiation and longwave enhancement were subsequently assessed using measurements from forest stands located within seasonally snow-covered regions, which vary in vegetation density and cover the range of boreal plant functional types in CLM4.5. CLM4.5 was found to overestimate the diurnal range of sub-canopy longwave radiation and longwave enhancement, and simulation errors increased with decreasing cloudiness and increasing vegetation density. Implementation of a parameterization of heat storage by biomass reduced simulation errors, but only marginally affected the amplitude of diurnal ranges. In contrast, SNOWPACK simulated a small diurnal range of sub-canopy longwave radiation across the range of vegetation density. A simple correction was derived from stand-scale simulations and implemented in global simulations of CLM4.5 in order to scale diurnal cycles of sub-canopy longwave radiation and assess the consequent impact on snow cover. Overestimated diurnal cycles of sub-canopy longwave radiation were found to result in underestimated averages of longwave enhancement over the snow cover season, as nighttime underestimation outweighed daytime overestimation. This underestimated energy input to snow resulted in an underestimation of snow temperatures and a general delay of meltout across snow-covered forests. However, the impact of overestimated diurnal cycles on daily average longwave enhancement was found to change throughout the snowmelt season, due to increasing insolation and day length, which results in spatial differences in its impact on meltout. These findings indicate that multiple vegetation layers are indispensable for accurate simulation of longwave enhancement and its impact on snow cover, thereby contributing to the growing evidence of limitations in modelling vegetation as a single layer.

Contents

1 Introduction **1**

1.1 Rationale 1

1.2 Review of vegetation-snow-atmosphere interactions and their representation in models 2

1.3 Research questions and objectives 9

1.4 Thesis structure 11

2 Theoretical background **13**

2.1 Sub-canopy longwave radiation and longwave enhancement 13

2.2 Modelling vegetation temperature and sub-canopy longwave radiation . . 15

2.2.1 Community Land Model (CLM) 15

2.2.2 SNOWPACK 20

3 Synthesis of forest-stand measurements of longwave enhancement **23**

3.1 Forest stands 23

3.1.1 Alptal, Switzerland 23

3.1.2 Seehornwald, Switzerland 24

3.1.3 Sodankylä, Finland 25

3.1.4 Cherskiy, Russia 26

3.1.5 Abisko, Sweden 27

3.1.6 Yakutsk, Russia 28

3.1.7 Borden, Canada 28

3.2 Observations of longwave enhancement and net snow surface radiation . . 29

3.3 Discussion 34

4 Forest stand-scale evaluation **37**

4.1 Toy Model setup 37

4.2 Forcing and evaluation data 39

4.3 Site comparison 48

4.4 Comparison of sub-canopy longwave radiation simulated by CLM4.5 and SNOWPACK with observations 51

4.5 Simulation of longwave enhancement by CLM4.5 55

4.6 Impact of biomass heat storage on simulation of longwave enhancement by CLM4.5 59

4.7 Influence of vegetation density on simulation error 63

4.8 Sensitivity studies 65

4.8.1 Interception of precipitation for SNOWPACK 65
4.8.2 Approximations of forcing data and parameters 65
4.8.3 Sensitivity to plant area index (PAI) 74
4.9 Discussion 78
4.10 Conclusion 80

5 Impact of deficient longwave enhancement on snow cover in global land-only simulations of CLM4.5 81
5.1 Methodology 81
5.1.1 Correction of sub-canopy longwave radiation in CLM4.5 81
5.1.2 Global offline simulations with CLM4.5 82
5.2 Calculation of correction factors 83
5.3 Effect of correction in offline simulations of CLM4.5 86
5.3.1 Sub-canopy longwave radiation – case study Alptal, Switzerland . 86
5.3.2 Longwave enhancement and limited spatial variability in ε_{sky} . . 91
5.3.3 Snow cover and snowmelt 92
5.4 Discussion 95
5.5 Conclusions 99

6 Impact of deficient longwave enhancement on snow cover in global coupled land-atmosphere simulations of CLM4.5 100

7 Discussion and outlook 107

8 Summary 116

References 118

List of Figures

2.1 Maps of relevant PFTs in CLM4.5 17
2.2 Comparison of radiation schemes between CLM4.5 and SNOWPACK . . 19
3.1 Rail setup at Alptal, Switzerland 23
3.2 Rail setup at Seehornwald, Switzerland 24
3.3 Pine forest near Sodankylä, Finland 25
3.4 Radiometers at larch forest near Cherskiy, Russia 26
3.5 Birch forest near Abisko, Sweden 27
3.6 Larch forest near Yakutsk, Russia 28
3.7 Mixed forest near Borden, Canada 29
3.8 Observations of longwave enhancement at forest stands 31
3.9 Observations of snow surface net radiation at forest stands 32
3.10 Observations of daily average snow surface net radiation at forest stands . 33
4.1 Toy Model workflow 38
4.2 Fractional stem area index (SAI) for grid cells of forest stands 40
4.3 PDF of ground albedo measurements at Seehornwald, Switzerland 41
4.4 PDF of ground albedo measurements at Cherskiy, Russia 43
4.5 Comparison of air temperatures and insolation across forest stands 48
4.6 Comparison of effective emissivity of the sky across forest stands 49
4.7 Comparison of absorption and emission factors in CLM4.5 and SNOWPACK across forest stands 50
4.8 Comparison of observed and simulated sub-canopy longwave radiation for CLM4.5 and SNOWPACK 51
4.9 Comparison of vegetation temperatures at Sodankylä, Finland 52
4.10 Calibration of SNOWPACK for Seehornwald, Switzerland 53
4.11 Calibration of SNOWPACK for Sodankylä, Finland 54
4.12 Systematic errors in sub-canopy longwave radiation simulated by CLM4.5 56
4.13 Comparison of observed and simulated longwave enhancement for CLM4.5 57
4.14 PDFs of longwave enhancement from observations and simulations . . . 60
4.15 RMSE and MB of Toy Model sites 61
4.16 Impact of biomass heat storage on sub-canopy longwave radiation simulated by CLM4.5 62
4.17 Average diurnal ranges of vegetation temperatures simulated by CLM4.5 . 64
4.18 Sensitivity of Toy Model results to approximations for Alptal, Switzerland 65
4.19 Sensitivity of Toy Model results to approximations for Seehornwald, Switzerland 66

4.20 Sensitivity of Toy Model results to approximations for Sodankylä, Finland 67
4.21 Sensitivity of Toy Model results to approximations for Cherskiy, Russia . 69
4.22 Sensitivity of Toy Model results to approximations for Abisko, Sweden . 71
4.23 Sensitivity of Toy Model results to approximations for Yakutsk, Russia . . 71
4.24 Sensitivity of Toy Model results to approximations for Borden, Canada . . 73
4.25 Sensitivity of Toy Model results to plant area index (PAI) 77
5.1 PFT coverage by and weighted PAI of evergreen needleelaf trees as well as grid-cell elevation across snow-covered Northern Hemisphere 83
5.2 Simulation error by CLM4.5 as ratio of longwave radiation emitted from vegetation with superimposed regression estimates 84
5.3 Regression coefficients for calculation of correction 85
5.4 Comparison of corrected and uncorrected simulations of sub-canopy longwave radiation with observations for grid cell of Alptal, Switzerland . . . 87
5.5 Comparison of corrected and uncorrected simulations of longwave enhancement with observations for grid cell of Alptal, Switzerland 89
5.6 Comparison of simulated and observed longwave enhancement for grid cell of Alptal, Switzerland as a function of ε_{sky} 90
5.7 Frequency of overcorrection in global simulations 91
5.8 Impact of correction on longwave enhancement and snow cover in offline simulations 93
5.9 Change in cold content and snow off date due to correction in offline simulations across Siberia 94
6.1 Impact of correction on longwave enhancement and snow cover in coupled simulations 101
6.2 Comparison of effective emissivity of the sky between offline and coupled simulations 102
6.3 Change in snow cover due to correction in coupled simulations as function of PFT coverage 106

List of Tables

2.1 Canopy top and bottom heights in CLM4.5 16
3.1 Overview of forest stands 30
4.1 Characteristics of forest stand sites 46
4.2 Measurements and approximations of forcing variables for Toy Model . . 47
4.3 RMSE and MB for sub-canopy longwave radiation simulated by CLM4.5 58
4.4 RMSE and MB for impact of biomass heat storage on sub-canopy longwave radiation simulated by CLM4.5 63
4.5 Sensitivity of Toy Model results to approximations for Sodankylä, Finland 68
4.6 Sensitivity of Toy Model results to approximations for Cherskiy, Russia . 69
4.7 Sensitivity of Toy Model results to approximations for Abisko, Sweden . 70
4.8 Sensitivity of Toy Model results to approximations for Borden, Canada . . 72
4.9 Sensitivity of Toy Model results (RMSE) to plant area index (PAI) 75
4.10 Sensitivity of Toy Model results (MB) to plant area index (PAI) 76
5.1 Regression coefficients used for calculation of correction factors 86

List of Abbreviations

AMIP	Atmosphere Model Intercomparison Project
BDBS	Broadleaf Deciduous Boreal Shrub
BDBT	Broadleaf Deciduous Boreal Tree
C3AG	C3 Arctic Grass
CAM(5)	Community Atmosphere Model, version 5
CCSM(4)	Community Climate System Model, version 4
CESM(1.2)	Community Earth System Model, version 1.2
CLM(4,4.5)	Community Land Model, version 4 or 4.5
CMIP(3,5)	Climate Model Intercomparison Project, phase 3 or 5
CORR	CLM/CESM simulation with correction factors implemented
CTRL	CLM/CESM simulation without correction factors
HadISST	Hadley Centre Sea Ice and Sea Surface Temperature data set
IPCC AR5	Intergovernmental Panel on Climate Change, Assessment Report 5
IPSL-ESM	Institute Pierre Simon Laplace Earth System Model
ISBA-LSM	Interactions between the Soil–Biosphere–Atmosphere Land Surface Model
LAI	Leaf Area Index
LiDAR	Light Detection And Ranging
MB	Mean Bias
MODIS	Moderate Resolution Imaging Spectroradiometer
NCAR	National Center for Atmospheric Research
NDBT	Needleleaf Deciduous Boreal Tree
NEBT	Needleleaf Evergreen Boreal Tree
NETT	Needleleaf Evergreen Temperate Tree
NH	Northern Hemisphere
ORCHIDEE	Organising Carbon and Hydrology In Dynamic Ecosystems
PAI	Plant Area Index
PDF	Probability Density Function
PFT	Plant Functional Type
RMSE	Root-Mean-Square Error
SAI	Stem Area Index
SCE	Snow Cover Extent
SCF	Snow Cover Fraction
SnowMIP(2)	Snow Model Intercomparison Project, phase 2

Acknowledgements

First, I would like to thank Dr. Nick Rutter, Dr. Chris Fletcher, and Dr. Leanne Wake for their guidance and support, for providing calmness and optimism when I was lacking such, and generally for being role models in my development as a researcher. Thank you for providing all the opportunities I had over the last three years and for creating jovial work environments at Northumbria and Waterloo. Needless to say, this thesis would not have been possible without their help.

This thesis would also not have been possible without data from forest stands across the Northern Hemisphere, and I am grateful to everyone who was involved in collecting those measurements. Particular thanks are extended to: Dr. Heather Kropp and Dr. Mike Loranty at Colgate University for providing data from Cherskiy; Dr. Paul Bartlett for providing data from Borden; Dr. Clare Webster for providing data from Seehornwald; Dr. Tobias Jonas for providing data from Alptal and Dr. Patrick Schleppi for providing measurements of ground water from Alptal; Dr. Nick Rutter for providing data from Abisko and Sodankylä as well as Annika Kristoffersson at the Swedish Polar Research Secretariat for providing measurements from Abisko; and Takeshi Ohta for helping with data from Yakutsk, which are available online at http://www.jamstec.go.jp/iorgc/hcorp/data/database/cdc/siberia/sub4.html where the site is listed as Larch Forest of Spasskaya Pad. Thanks are also extended to the National Center for Atmospheric Research and the Eidgenössische Forschungsanstalt für Wald, Schnee und Landschaft - Institut für Schnee- und Lawinenforschung for providing public access to their models – CESM1.2 at https://svn-ccsm-release.cgd.ucar.edu/model_versions/cesm1_2_0/ and SNOWPACK at https://models.slf.ch/p/snowpack/.

I would again like to thank Dr. Mike Loranty, whose funding from the The Picker Interdisciplinary Science Institute at Colgate University allowed for some truly creative project meetings – one last cheers to Harvey at this point – and supported me during this research. I would also like to thank Dr. Chris Derksen, Dr. Lawrence Mudryk, and Dr. Libo Wang for their feedback at those aforementioned project meetings. Thanks are also extended to the Canadian Sea Ice and Snow Evolution (CanSISE) network, which supported this research as well.

A big thanks to Sina Panitz and Jack Longman for their hospitality and friendship upon my arrival in Newcastle as well as to Chad Thackeray and Yaasiin Oozeer for their help, company, and travel advice across the big pond. I also want to thank my family, who supported me during these three years and only got the occasional visit in return. Finally, I want to thank my dearest Leanne, who helped me so much more during this last year than she realizes.

Declaration of Authorship

I declare that the work contained in this thesis has not been submitted for any other award and that it is all my own work. I also confirm that this work fully acknowledges opinions, ideas and contributions from the work of others. Any ethical clearance for the research presented in this thesis has been approved.
I declare that the Word Count of this Thesis is 36,421 words.

Name: Markus Todt

Signature:

Date: 29 January 2019

At the time of submission, the contents of two chapters in this thesis have been published in peer-reviewed journals:

Chapter 4 is published as: Todt, M., N. Rutter, C. G. Fletcher, L. M. Wake, P. A. Bartlett, T. Jonas, H. Kropp, M. M. Loranty, and C. Webster (2018), Simulation of Longwave Enhancement in Boreal and Montane Forests, *Journal of Geophysical Research: Atmospheres*, 123 (24), 13,731–13,747, doi:10.1029/2018JD028719.

Chapters 5 is published as: Todt, M., N. Rutter, C. G. Fletcher, and L. M. Wake (2019), Simulated single-layer forest canopies delay Northern Hemisphere snowmelt, *The Cryosphere Discussions*, doi:10.5194/tc-2018-270, in review.

1 Introduction

1.1 Rationale

Observed Northern Hemisphere (NH) spring snow cover extent (SCE) has declined rapidly since the start of the 21st century at a rate exceeding that for annual minimum sea ice extent (*Derksen and Brown*, 2012) and this decline in SCE is projected to continue, or even accelerate, over the remainder of the 21^{st} century (*Brutel-Vuilmet et al.*, 2013; *Thackeray et al.*, 2016). Both decreasing snow cover and sea ice are part of a larger change of the cryosphere with consequent environmental, ecological, and socio-economic impacts (*Jeffries et al.*, 2013). This change is associated with arctic amplification, a positive feedback loop resulting in a faster increase of temperatures in polar regions compared to the global average. Surface-albedo feedbacks, i.e. temperature changes due to albedo changes caused by retreating (or advancing) snow and sea ice, constitute the second largest contribution to arctic amplification (*Pithan and Mauritsen*, 2014). In recent decades, the total impact of cryospheric cooling on the Earth's radiation budget has declined with similar overall contributions from snow cover and sea ice (*Flanner et al.*, 2011). The decline in NH spring SCE cannot be explained solely by natural factors as a combination of natural and anthropogenic forcing is necessary to simulate such strong multi-decadal trends (*Rupp et al.*, 2013).

Significant challenges persist in the representation of SCE in the current generation of climate models. Both observed trend and interannual variability in boreal spring SCE exceed the range of historical simulations from the Climate Model Intercomparison Project's fifth phase (CMIP5) suite of models, reducing confidence in future projections (*Derksen and Brown*, 2012; *Brutel-Vuilmet et al.*, 2013; *Rupp et al.*, 2013; *Mudryk et al.*, 2014; *Thackeray et al.*, 2016). This issue was also addressed in the Intergovernmental Panel on Climate Change's Fifth Assessment Report (IPCC AR5; *Flato et al.*, 2013, Chapter 9.4.4.1, page 790) stating that "there is a significant inter-model scatter of spring snow cover extent in some regions" (*Brutel-Vuilmet et al.*, 2013) and that the "recent negative trend in spring snow cover is underestimated by the CMIP5 (and CMIP3) models (Derksen and Brown, 2012), which is associated with an underestimate of the boreal land surface warming (Brutel-Vuilmet et al., 2013)." Imperfect model physics and large inter-model spread may partly be due to modelling of processes within boreal forests. Snow Model Intercomparison Project's second phase (SnowMIP2) revealed higher modelling skill for open than for forested sites, which was attributed to more complex snow processes in forested areas (*Essery et al.*, 2009; *Rutter et al.*, 2009). This is particularly concerning considering that boreal forests are estimated to make up almost one fifth of the NH seasonally

snow-covered region (*Rutter et al.*, 2009). Therefore, continual assessment and consequent improvement of parameterizations and modelling of vegetation-snow-atmosphere processes is of paramount importance. This thesis contributes to the assessment of snow-vegetation-atmosphere interactions in global climate models by focussing on longwave radiation beneath forest canopies, its simulation by a state-of-the-art land surface model and influence on snow cover and snowmelt. In this chapter, objectives and research questions of this thesis are derived from the existing literature and it is outlined how this thesis will answer the posed questions.

1.2 Review of vegetation-snow-atmosphere interactions and their representation in models

Although surface air temperature exhibits the biggest influence on snowmelt onset (*Wang et al.*, 2013), *Wang et al.* (2015) found shortwave and longwave radiation displaying a complex behaviour that determines years of negative SCE anomalies. Early on, low-SCE years are characterized by negative shortwave radiation anomalies and positive cloudiness and longwave radiation anomalies, but signs of anomalies subsequently reverse. As insolation is low during boreal winter due to low solar elevation angles, increased cloudiness and thus higher longwave radiation result in positive anomalies of radiative energy input, which causes reduced snow cover and consequently reduced surface albedo. When insolation increases later in the snow season and dominates the surface energy balance, reduced albedo leads to anomalously high absorption, so that positive anomalies of shortwave radiation further enhance negative SCE anomalies. Therefore, low-SCE years are characterized by a feedback that combines the impact of longwave and shortwave radiation at different periods of the snow season, which highlights the varying importance of radiation components for snow cover and snowmelt throughout the snow season. Future warming will result in an earlier onset of snowmelt, happening under conditions of lower solar elevation and consequently less energy input, which will likely lead to decreasing melt rates (*Musselman et al.*, 2017; *Wu et al.*, 2018). This will affect the contribution of radiation components to snowmelt due to their changing importance throughout the snow cover season and suggests that longwave radiation could become a more prominent driver of snowmelt.

Net radiation is the dominating surface energy balance term in boreal forests as turbulent fluxes are suppressed beneath the canopy causing forests to act as cold air sinks (*Price*, 1988; *Link and Marks*, 1999b; *Webster et al.*, 2016a). Apart from wind speed, shortwave radiation is the main meteorological variable controlling snowmelt that is altered by forest coverage (*Ohta et al.*, 1990). Trees, evergreen even more so than deciduous,

shade the ground, which causes a reduced supply of energy to the snow. In doing so, trees absorb a substantial amount of shortwave radiation due to their low albedo and emit longwave radiation based on their temperatures. Therefore, trees act as radiators transforming shortwave radiation into longwave radiation, which results in an altered effect on the snow surface energy balance compared to open areas. This varied impact is further complicated as snow exhibits distinctly different absorptions of shortwave and longwave radiation that are described by albedo and emissivity, respectively.

Longwave radiation emitted from forest canopies towards the ground frequently exceeds atmospheric longwave radiation. This process is called longwave enhancement and can lead to a positive impact of forest cover on snowmelt when outweighing reduced shortwave radiation. Extensive observations of sub-canopy longwave radiation in dense subalpine and alpine forests revealed longwave enhancement of up to 150% (*Webster et al.*, 2016a,b). Comparison of sub-canopy and atmospheric longwave radiation for less dense forest stands exhibited smaller, but still substantial enhancement of longwave radiation beneath forest canopies (*Rowlands et al.*, 2002; *Sicart et al.*, 2004; *Essery et al.*, 2008). These studies have also highlighted the increase of longwave enhancement with decreasing cloudiness, which is due to decreasing atmospheric longwave radiation as well as increasing insolation and consequently increasing vegetation temperatures under clearer skies. In contrast, enhancement of longwave radiation is small and longwave radiation can even be reduced beneath forest canopies for overcast conditions, when vegetation temperature and radiative temperature of the sky are similar. While observations have shown trunks heating up due to insolation and consequently increased emission of longwave radiation (*Rowlands et al.*, 2002; *Pomeroy et al.*, 2009), diurnal variations in tree temperatures depend on exposure to shortwave radiation and thus vegetation density (*Webster et al.*, 2016a). Moreover, longwave enhancement has been shown to result in substantial positive net longwave radiation at the ground when snow cover is prevalent, reaching ten-minute averages of up to 40 Wm^{-2} under clear skies and during snowmelt (*Webster et al.*, 2016a). In contrast, net longwave radiation fluxes of about -100 Wm^{-2} are typical for snow under clear-sky conditions in unforested areas. Similar contrasts in net longwave radiation of the snow surface between forested and unforested sites have been observed for evergreen Canadian boreal forests (*Harding and Pomeroy*, 1996; *Ellis et al.*, 2010). Positive net longwave radiation fluxes are due to snow surface temperature being limited to $0^{\circ}\mathrm{C}$ while vegetation temperatures increase with solar elevation and season, which indicates longwave enhancement is a crucial process that can contribute to ripening or melting of snow cover.

Early studies on the impact of trees on snow cover used geometrical models at the stand

scale (*Hardy et al.*, 1997; *Link and Marks*, 1999b; *Woo and Giesbrecht*, 2000), the results of which were then implemented in snow models (*Link and Marks*, 1999a; *Giesbrecht and Woo*, 2000). Vegetation enhancing snowmelt has been reported for a subarctic open woodland during overcast days and early in the snowmelt season when solar elevation was low (*Woo and Giesbrecht*, 2000), which is similar to the mechanism described by *Wang et al.* (2015). While the impact of shading by trees increases with insolation and thus becomes more important later in the snowmelt season, snow beneath the tree had already completely melted for that study before shading could have become detrimental to snowmelt. Studies have used different approaches to quantify the conditions under which forest coverage enhances snowmelt. *Yamazaki and Kondo* (1992) varied idealized meteorological forcing, canopy density, and snow albedo for coupled one-dimensional canopy and snow models, which revealed a general decrease of snowmelt with increasing canopy density except for high snow albedo. A modelling study, which was based on observations in larch forest stands of different vegetation densities, confirmed the impact of vegetation density on snowmelt depending on snow albedo (*Suzuki and Ohta*, 2003). These findings are supported by a sensitivity study of daytime net radiation to meteorological conditions and forest canopy density, which used a simple model based on meteorological observations (*Sicart et al.*, 2004). Forest cover was found to enhance melt under clear-sky conditions due to low atmospheric longwave radiation as well as early in the snowmelt season, when snow albedo was high and insolation was low. Moreover, it was found that snow albedo was more important than forest density in determining acceleration or delay of snowmelt by the presence of trees. *Strasser et al.* (2011) used measurements of meteorological forcing covering several snow seasons to drive simulations of evergreen needleleaf trees. Forest cover was generally found to result in less snow accumulation on the ground, due to sublimation of snow intercepted by the canopy, and to extend snow cover duration as canopy coverage shades the ground reducing energy input. However, canopy interception consistently reduced accumulation throughout the snow season while the impact of shading changed with solar elevation and thus increased throughout the snowmelt season. For little snow cover and little insolation, reduced accumulation outweighed reduced energy input and forest cover caused melt-out events. Comparison between paired forested and unforested sites has revealed the impact of forest cover on snowmelt to depend on winter air temperatures, while the temporally changing importance of shortwave radiation and longwave radiation was confirmed (*Lundquist et al.*, 2013). When snowmelt occurs early, due to high air temperatures and mid-winter melt events, solar angles are still low. Consequently, longwave enhancement outweighs shading and forests accelerate snowmelt compared to open areas. In summary, several stand-scale studies have highlighted the

impact of forest coverage on snowmelt varying regionally, depending on forest density and meteorological conditions as the respective contributions by shortwave and longwave radiation change throughout the snow cover season.

Complex processes between atmosphere, snow, and vegetation lead to less skill in modelling snow cover for forested than for open areas, which was identified by Snow Model Intercomparison Project's second phase (SnowMIP2; *Essery et al.*, 2009; *Rutter et al.*, 2009). In addition to altering energy fluxes that reach the snow surface, forest canopies influence mass fluxes by interception and subsequent unloading, evaporation, or sublimation of snowfall, which impacts surface albedo, vegetation temperatures, and consequently land-atmosphere interactions. As boreal forests consist mostly of evergreen needleleaf trees, they possess the ability to intercept a substantial amount of snowfall, causing a temporary spike in surface albedo, which reverts back to the darker canopy albedo after snow is removed (*Schmidt and Gluns*, 1991; *Betts and Ball*, 1997; *Storck et al.*, 2002). As the darker canopy vegetation masks the bright snow surface beneath, boreal forests exhibit a substantially lower surface albedo than open areas during snow coverage, and this effect is known as snow albedo masking or forest masking (*Robinson and Kukla*, 1985; *Essery*, 2013). Simulations from the suites of models submitted to Climate Model Intercomparison Project's third phase (CMIP3) and fifth phase (CMIP5) exhibited large biases in surface albedo over snow-covered forested regions with consequently detrimental impact on the simulation of snow-albedo feedback, i.e. acceleration of snowmelt due to decreasing albedo caused by snow retreat (*Roesch*, 2006; *Qu and Hall*, 2014). Comparison of different types of vegetation masking parameterizations in climate models yielded only slight differences in albedo and parameterizations compared reasonably well to observations, leaving parameter choices as possible causes for poor albedo simulations (*Essery*, 2013). *Loranty et al.* (2014) found boreal tree coverage to vary widely between CMIP5 models and to differ considerably from observations. Observations showed an approximately linear decrease of albedo with increasing tree coverage and this relation varied widely between models, which was attributed to varying representations of tree coverage in models. Generally, simulated surface albedo displayed a positive bias, especially over densely forested regions. *Wang et al.* (2016) examined the relationship between plant area index (PAI) and surface albedo and analyzed the representation of leaf area index (LAI) in CMIP5 models. A saturation effect for surface albedo was found at high PAI values, so that surface albedo is more sensitive to smaller PAI values and thus low biases in PAI, which implies distinct differences in surface albedo even between sparse forests and open areas. The comparison of several CMIP5 models revealed a large spread in winter LAI and surface albedo for evergreen needleleaf forests,

due to individual outliers, as well as significant correlations between LAI and surface albedo biases. These findings further emphasize the influence of spread in tree cover fraction on surface albedo simulation reported by *Loranty et al.* (2014).

CMIP5 models exhibit larger biases for surface albedo than for snow cover during the Northern Hemisphere snow season (*Thackeray et al.*, 2015). These biases are only weakly correlated, which indicates that deficient surface albedo simulations do not strictly originate from the simulated presence of snow and that additional factors contribute to those deficiencies in surface albedo simulations. Correlation between snow cover fraction and surface albedo is weaker for observations than for simulations, which implies that parameterizations used within models rely heavily on the presence of snow and undervalue the contribution from snow and snow-vegetation processes. Simulated surface albedo over boreal forests peaks too high and too early during winter, especially in Community Land Model version 4 (CLM4) (*Thackeray et al.*, 2014), which is the land component of the National Center for Atmospheric Research's (NCAR) Community Climate System Model version 4 (CCSM4) that was part of the CMIP5 suite of models (*Gent et al.*, 2011). In CLM4, the early peak in surface albedo results in a slower reduction of surface albedo during snowmelt season and consequently an underestimation of snow-albedo feedback. Detailed analysis of snow cover reveals a higher and longer-lasting peak of surface albedo with little to no variations, which is attributed to the parameterization of snow unloading in CLM4 (*Thackeray et al.*, 2014). This parameterization prohibits unloading for air temperatures below $0^{\circ}\mathrm{C}$, which suppresses variations in surface albedo, and prescribes instant, total unloading when $0^{\circ}\mathrm{C}$ is reached, which causes a more rapid reduction of surface albedo compared to observations. However, $0^{\circ}\mathrm{C}$ can be reached fairly early in winter during short events of higher insolation. This unloading parameterization is improved upon in CLM5, which was released in February 2018 as the land component of Community Earth System Model version 2, and is accompanied by an elaboration of the parameterization of canopy interception (presentation by *Perket et al.*, 2015). This interception parameterization differentiates between rain and snow, with different storage capacities, and includes unloading due to temperature and wind. Nevertheless, deficient simulation of surface albedo over boreal forests by CLM4 and CCSM4 is not only due to parameterization of canopy interception, as both models exhibit biases in snow cover timing during snow accumulation and snowmelt season (*Thackeray et al.*, 2014, 2015).

Due to its impact on mass and energy fluxes, canopy interception and unloading have been a major focus of improvements in parameterizations of snow-vegetation processes. Unloading schemes depend on different meteorological variables, however, the most suitable parameterization was found to change from site to site due to local meteorological

conditions, with the best cross-site unloading parameterization being based on wind speed (*Bartlett and Verseghy*, 2015). The dependence of model quality on local meteorological conditions was already encountered during SnowMIP2 (*Rutter et al.*, 2009). A novel interception parameterization based on airborne LiDAR data resulted in an improvement over classical interception parameterizations due to a change in the interception efficiency distribution, which represents the effects of snow bridging and branch bending (*Moeser et al.*, 2015). This new scheme partially utilises different canopy descriptors than classical parameterizations, such as distance to canopy and total open area, and was implemented in the Factorial Snow Model (*Essery*, 2015) and compared against the standard interception parameterization (*Hedstrom and Pomeroy*, 1998). Although still biased, the new parameterization performed considerably better, especially regarding spatial patterns of interception and snow depth, with interception magnitude and variability being closer to observations (*Moeser et al.*, 2016). Higher variance in simulated interception was found for sublimation and unloading, and the choice of different canopy-characterizing parameters compared to classical schemes yielded a better representation of structural forest heterogeneity. However, these canopy-characterizing parameters complicate the comparison between sites and interception models and still present difficulties in application at larger scales, thereby illustrating one of the major obstacles to improvement of land surface modelling. Moreover, representation of the vertical canopy structure has been found to affect simulations of canopy interception and its impact on snow cover (*McGowan et al.*, 2016). Vertical distribution of biomass determines where the majority of snowfall is intercepted and subsequently how much intercepted snow is exposed to the atmosphere. Top-heavy canopies lead to higher evaporation and sublimation losses and consequently less and shorter snow cover beneath the canopy.

The implementation of multiple vegetation layers in one-dimensional land models is not a novel approach per se. *Yamazaki et al.* (1992) developed a one-dimensional canopy model that subdivided the canopy into a trunk space and a crown space, the latter of which was further subdivided into two separate layers. Both crown layers featured individual energy balances and thus energy fluxes and temperatures. This two-layer canopy model was subsequently coupled to a one-dimensional snow model in order to explore the influence of canopy cover on snowmelt (*Yamazaki and Kondo*, 1992). After the addition of heat storage and interception of precipitation by vegetation, the two-layer canopy model was coupled to one-dimensional snow and soil models in order to simulate snow cover in a low-density larch forest (*Yamazaki*, 2001). However, one-layer and two-layer canopy models were not compared regarding the impact on snow cover. Global land models usually rely on a so-called "big-leaf" approach, which represents vegetation as

a single layer, due to computational costs. *Bonan et al.* (2014) introduced a multi-layer canopy to CLM4.5 in order to improve the simulation of canopy physiology and stomatal conductance. Subsequently, this multi-layer canopy was expanded by subdividing the roughness layer of CLM4.5, with separate temperatures for each layer, which resulted in improvements of turbulent fluxes as well as radiative temperature (*Bonan et al.*, 2018). However, these studies only performed simulations for single months and individual sites ranging from grassland to forest stands. Recently, the ORCHIDEE (Organising Carbon and Hydrology In Dynamic Ecosystems) land surface model, land component of the Institute Pierre Simon Laplace (IPSL) Earth System Model, was advanced from a big-leaf approach by implementation of a multi-layer energy budget scheme (*Chen et al.*, 2016; *McGrath et al.*, 2016; *Ryder et al.*, 2016). This scheme allows for within-canopy shortwave radiation, longwave radiation, and turbulent fluxes based on vertical profiles of LAI, with consequent influence on vertical profiles of canopy physiology. While this new ORCHIDEE-CAN (ORCHIDEE-CANopy) land surface model was tested at individual sites with separate parameters for each site, parameters will be generalized for plant functional types in the future in order to run global simulations.

So far, only one study has focused on the evaluation of sub-canopy longwave radiation simulated by single-layer vegetation and its potential improvement by increasing the complexity of canopy representation. *Gouttevin et al.* (2015) introduced heat storage by biomass and a second layer to the canopy module of one-dimensional snow model SNOWPACK. Subdivision of vegetation into two layers allowed for separate energy balances, separate vegetation temperatures, and consequently interaction between vegetation layers. While the original one-layer version of SNOWPACK exhibited overestimated diurnal cycles of sub-canopy longwave radiation, with overestimations during the day and more pronounced underestimations during the night, the increasing complexity of vegetation parameterization displayed a substantial improvement of simulated sub-canopy longwave radiation. Implementation of heat storage and release by biomass resulted in thermal inertia that delayed and slightly reduced the diurnal cycle of sub-canopy longwave radiation. Addition of a second layer was found to have a larger impact on sub-canopy longwave radiation, substantially reducing the diurnal cycle, which was attributed to sheltering by the upper layer and consequently reduced radiative cooling during the night. Nevertheless, introduction of both biomass heat storage and a second vegetation layer resulted in improved simulation skill for sub-canopy longwave radiation. Observational studies have shown differences in temperatures between tree components, especially during periods of high insolation when trunks exhibit higher temperatures than both needles and air (*Rowlands et al.*, 2002; *Pomeroy et al.*, 2009; *Webster et al.*, 2016a), which high-

lights the necessity of complex vegetation representation as well as the importance of vegetation density. Therefore, physical representation of tree components is important to accurately simulate variations in vegetation temperatures and consequently emittance of longwave radiation.

1.3 Research questions and objectives

Skill in modelling snow cover has been identified to be lower for forested than for open areas, which was attributed to complex processes between atmosphere, snow, and vegetation (*Essery et al.*, 2009; *Rutter et al.*, 2009). Although several studies have demonstrated the enhancement of longwave radiation beneath forest canopies (*Rowlands et al.*, 2002; *Sicart et al.*, 2004; *Essery et al.*, 2008; *Pomeroy et al.*, 2009; *Howard and Stull*, 2013; *Lundquist et al.*, 2013; *Webster et al.*, 2016a), as yet there have been no efforts to assess simulation of this process by global climate models. The essentially unknown accuracy of longwave enhancement in global climate models raises two questions.

1. How well is longwave enhancement simulated in global climate models? Can increasing complexity of canopy representation improve simulation of longwave enhancement in global climate models?
2. What impact do potential deficiencies in simulated longwave enhancement have on snow cover across the Northern Hemisphere?

In order to answer these questions, this thesis uses the Community Land Model version 4.5 (CLM4.5), land component of Community Earth System Model version 1.2 (CESM1.2) whose precursor version Community Climate System Model version 4 (CCSM4) was part of the CMIP5 suite of models (*Gent et al.*, 2011). CLM4.5 and CESM1.2 are publicly available online and widely used in the scientific community. CLM4.5 represents vegetation by a single layer, which is a common approach for global land models, and both CLM4 and CCSM4 exhibit deficient snow cover timing over boreal forests (*Thackeray et al.*, 2014, 2015). In contrast, simulation of sub-canopy longwave radiation has been improved in one-dimensional model SNOWPACK by increasing the complexity of canopy representation (*Gouttevin et al.*, 2015).

Since evaluation of simulated longwave enhancement is not practicable on a global scale, as detailed observational products for vegetation temperature or sub-canopy longwave radiation are neither existent nor feasible, simulations and model parameterizations can only be assessed using data from observational sites. Note that usage of forest stand-scale data does not downscale processes to individual trees. Vegetation at those observational sites is characterised by LAI, canopy coverage, etc. and is thus still conceptualized as

a vegetation layer. Therefore, stand-scale representation is the same as for a grid cell and application of a large-scale modelling scheme is equally valid for these sites. Past model intercomparisons have used offline simulations, i.e. uncoupled model components, or extensive point-scale forcing data (*Henderson-Sellers et al.*, 1995; *Rutter et al.*, 2009), while success in increasing process-level understanding was achieved by focussing on and comparing forest albedo masking or specific snow parameterizations (*Essery*, 2013; *Essery et al.*, 2013; *Lafaysse et al.*, 2017). A similar approach is used to answer Research Question 1 by creating a toy model to simulate forest stand-scale sub-canopy longwave radiation by CLM4.5 and to compare CLM4.5 with SNOWPACK. This approach uses these models outside of their parent model frameworks enabling application of the same stand-scale forcing data and simplifying comparison, modification, and tracking the effect of changes. Consequently, the objectives for answering Research Question 1 are to:

i. present an overview of measurements of sub-canopy longwave radiation and longwave enhancement across forests of different vegetation types and densities

ii. construct a toy model to use stand-scale observations for evaluation of simulation of sub-canopy longwave radiation and longwave enhancement by CLM4.5 and direct comparison to sub-canopy longwave radiation simulated by SNOWPACK

iii. evaluate the addition of a biomass heat storage parameterization within CLM4.5.

In order to avoid implementing multiple vegetation layers in a global land model and associated computational costs, an alternative method is necessary to answer Research Question 2. A correction to sub-canopy longwave radiation is developed based on conclusions from answering Research Question 1 and guided by the effect of separate vegetation layers on sub-canopy longwave radiation, which is subsequently implemented in CLM4.5.While simulation of sub-canopy longwave radiation and longwave enhancement by land surface models had so far been assessed using forest stand-scale forcing and evaluation data, land-only and coupled simulations of CLM4.5 are used to assess the impact of deficiencies in longwave enhancement on global snow cover and snowmelt. Therefore, the following objectives are set in order to answer Research Question 2:

i. creation of a correction of sub-canopy longwave radiation simulated by one-layer vegetation in CLM4.5

ii. demonstration of the correction effect on diurnal cycles and daily averages of longwave enhancement

iii. evaluation of the impact of corrected longwave enhancement on snow cover and snowmelt across the Northern Hemisphere.

1.4 Thesis structure

How Research Questions 1 and 2 are answered as well as the structure of this thesis are described in the following:

Chapter 1: Introduction
This current chapter serves as an introduction to the importance of forests for global snow cover, shortcomings in simulation of snow cover related to forest coverage, and vegetation-snow-atmosphere processes. Current knowledge is presented relevant to the process of longwave enhancement and its simulation in land models. Research questions are derived from the current state of knowledge, and chapters that answer these research questions are outlined.

Chapter 2: Theoretical background
Longwave enhancement and sub-canopy longwave radiation as well as their calculations are explained in detail, as is effective emissivity of the sky, a measure of cloudiness used throughout this thesis. CESM/CLM and SNOWPACK, the models used for this thesis, are introduced and their representations of vegetation are compared. Calculations of vegetation temperature and sub-canopy longwave radiation in CLM and SNOWPACK are described with emphasis on radiative fluxes and the differences between these two models.

Chapter 3: Synthesis of forest-stand measurements of longwave enhancement
In order to answer Research Question 1, forest stand-scale measurements of sub-canopy longwave radiation are necessary for evaluation of simulations. This chapter presents forest stands, from which measurements are used for this thesis, and describes radiometer arrays that had previously been deployed to measure sub-canopy longwave radiation. Additionally, measurements are used to give an overview of longwave enhancement across forest stands and meteorological conditions, and the influence of forest cover on net radiation of the snow surface is illustrated.

Chapter 4: Forest stand-scale evaluation
Research Question 1 is addressed by developing a framework to drive simulations of sub-canopy longwave radiation by CLM4.5 and SNOWPACK with forest stand-scale data. Simulation of sub-canopy longwave radiation by CLM4.5 and SNOWPACK is assessed and compared for evergreen forest stands, and longwave enhancement simulated by CLM4.5 is assessed across evergreen and deciduous forest stands. SNOWPACK's

parameterization of biomass heat storage is implemented in CLM4.5 in order to test its impact on simulated sub-canopy longwave radiation. Sensitivity of simulation errors to forcing data and decisions, vegetation density, and calibration parameters of SNOWPACK is investigated. This chapter has been published as *Todt et al.* (2018).

Chapter 5: Impact of deficient longwave enhancement on snow cover in global land-only simulations of CLM4.5

Research Question 2 is addressed by deriving an empirical correction of sub-canopy longwave radiation from stand-scale simulations and subsequently implementing this correction in global simulations of CLM4.5. Reduced diurnal cycles of sub-canopy longwave radiation are compared with observations from one of the forest stands described in Chapter 3. Impact of correction on longwave enhancement and snow cover is assessed in global land-only simulations. Development and implementation of correction as well as assessment of impact on land-only simulations of CLM4.5 is currently under open review (*Todt et al.*, 2019).

Chapter 6: Impact of deficient longwave enhancement on snow cover in global coupled land-atmosphere simulations of CLM4.5

Impact of corrected longwave enhancement on snow cover found in Chapter 5 is validated using global coupled land-atmosphere simulations due to a lack of variability in meteorological conditions of land-only simulations.

Chapter 7: Discussion and outlook

Results from Chapters 3 to 6 are summarized and discussed in the wider context of scientific literature, and contribution to the existing knowledge is highlighted.

Chapter 8: Summary

The thesis is concluded by a brief summary of its main results and future research priorities.

2 Theoretical background

2.1 Sub-canopy longwave radiation and longwave enhancement

Longwave enhancement is the process of vegetation changing, usually increasing, longwave radiation reaching the ground relative to atmospheric forcing. As such longwave enhancement can be non-existent in two cases, either if there is no vegetation coverage and longwave radiation reaching the ground is the very atmospheric forcing or if longwave radiation emitted by vegetation is equal to atmospheric forcing. In order to quantify this effect, a longwave enhancement factor LWE is calculated as the ratio between downward longwave radiation below the canopy LW_{bc} and downward longwave radiation above the canopy LW_{ac}

$$LWE = \frac{LW_{bc}}{LW_{ac}} = \frac{LW_{sub}}{LW_{atm}}, \tag{2.1}$$

which are equivalent to sub-canopy longwave radiation LW_{sub} and atmospheric longwave radiation LW_{atm}, respectively. A longwave enhancement factor of 1 indicates no vegetation or no impact of vegetation cover, whereas values of more or less than 1 indicate increase and decrease, respectively, of sub-canopy longwave radiation due to vegetation. Although generally larger than 1, longwave enhancement values can be smaller when cloud cover increases atmospheric longwave radiation and limits insolation. Since atmospheric longwave radiation is an input variable to land surface models, from either observations or an atmospheric model, simulated longwave enhancement depends on simulated sub-canopy longwave radiation.

Sub-canopy longwave radiation is generally calculated as a weighted sum of atmospheric longwave radiation and longwave radiation emitted by the vegetation. The weighing factor is a parameter describing fractions of vegetation and sky of a particular location, e.g. canopy coverage for models or estimated from sky-view fraction for observational sites. Labelling this parameter vegetation fraction f_{veg}, sub-canopy longwave radiation is calculated as

$$LW_{sub} = (1 - f_{veg})\, LW_{atm} + f_{veg}\, LW_{veg}, \tag{2.2}$$

with longwave radiation emitted from vegetation LW_{veg}. Combining Equations (2.1) and (2.2) demonstrates that simulated longwave enhancement only depends on the representation of and longwave radiation attributed to vegetation.

Longwave radiation LW emitted by a grey body, i.e. a body that absorbs and emits less energy than a black body, is described by the Stefan-Boltzmann law and calculated as

$$LW = \varepsilon\, \sigma\, T^4, \tag{2.3}$$

with ε, a value between 0 and 1, being the emissivity of the body, Stefan-Boltzmann constant $\sigma \cong 5.67 \cdot 10^{-8}\ \mathrm{Wm^{-2}K^{-4}}$, and surface temperature of the body T. Therefore, sub-canopy longwave radiation and thus longwave enhancement are directly linked to vegetation surface temperatures.

Longwave enhancement depends on meteorological conditions as these influence both atmospheric longwave radiation (directly) and vegetation temperatures (indirectly). Clear skies lead to higher insolation and consequently higher vegetation temperatures, while atmospheric longwave radiation is reduced, especially during clear-sky nights. In contrast, atmospheric longwave radiation is increased for overcast conditions but little insolation restricts heating-up of vegetation during overcast days. As atmospheric longwave radiation and vegetation temperatures react contrarily to those meteorological changes, longwave enhancement is highly impacted by them (Equation (2.1)).

A measure of meteorological conditions is effective emissivity of the sky, ε_{sky}, which quantifies the contrast between atmospheric longwave radiation and (near-)surface air temperature:

$$\varepsilon_{sky} = \frac{LW_{atm}}{\sigma\, T_{air}^4} \tag{2.4}$$

with (near-)surface or above-canopy air temperature T_{air}. While brightness temperature of the sky, i.e. the temperature corresponding to measured atmospheric longwave radiation, might be close to (near-)surface air temperatures for overcast conditions, contrasts are stark for clear-sky conditions as atmospheric longwave radiation is decreased but (near-)surface air temperatures are increased due to higher insolation. Note that the effective emissivity of the sky can reach values larger than 1 for overcast conditions. This is reminiscent of longwave enhancement, which can reach values of less than 1 for overcast conditions, and indeed effective emissivity of the sky is similar to the inverse of longwave enhancement only differing in the usage of air or vegetation temperature.

2.2 Modelling vegetation temperature and sub-canopy longwave radiation

2.2.1 Community Land Model (CLM)

Community Land Model (CLM) is a global land surface model and the land component of Community Earth System Model (CESM), a global climate model developed by the National Center for Atmospheric Research (NCAR). The precursor version of CESM, Community Climate System Model version 4 (CCSM4), as well as its land component Community Land Model version 4 (CLM4) were part of Climate Model Intercomparison Project's fifth phase (CMIP5) suite of models (*Gent et al.*, 2011). Both CESM/CCSM and CLM have recently participated in a range of model intercomparisons and model evaluation studies, with assessment and inter-model comparison of simulated snow cover on point scales (*Essery et al.*, 2009; *Rutter et al.*, 2009; *Essery et al.*, 2013; *Chen et al.*, 2014) and on global scales (*Thackeray et al.*, 2016; *Mudryk et al.*, 2017). Moreover, CESM/CCSM and CLM have been assessed regarding the simulation of surface albedo and snow albedo feedback (*Qu and Hall*, 2007, 2014; *Thackeray et al.*, 2015) as well as regarding the simulation of surface albedo over boreal forests in particular (*Essery*, 2013; *Li et al.*, 2016; *Wang et al.*, 2016). As their names suggest, CESM and CLM are publicly available to the scientific community. The availability of CESM and CLM and their vast usage for evaluations and intercomparisons make these models a suitable choice for the purpose of this thesis. At the start of this PhD project, CESM version 1.2 (CESM1.2) and CLM version 4.5 (CLM4.5) were the latest released versions. Description of CLM4.5 is given by *Oleson et al.* (2013), and representation of vegetation and calculation of sub-canopy longwave radiation within CLM4.5 are described in the following.

Sub-grid hierarchy in CLM4.5 consists of 3 levels. On the broadest scale, CLM4.5 subdivides grid cells based on 5 land units – vegetated, crop (turned off by default), glacier, lake, and urban. Vegetated land units are subsequently subdivided based on plant functional types (PFTs), with up to 16 possible PFTs as well as bare soil. Vegetation-specific variables and parameters, such as sub-canopy longwave radiation, vegetation temperature, and vegetation density, are differentiated for each PFT present in a grid cell. State variables of the ground are captured by soil and snow columns, which consist of 15 soil layers, increasing in thickness from top to bottom, and up to 5 layers of snow depending on snow depth. All PFTs within one vegetated land unit share a single column of snow and soil, which allows for competition for water between PFTs. Consequently, fluxes from vegetation to the ground are weighted averages over all PFTs and changes in fluxes from an individual PFT affect snow cover beneath every PFT in a particular vegetated

Table 2.1: Canopy top and bottom heights for boreal plant functional types in CLM4.5 (*Bonan et al.*, 2002). Values are identical for NEBTs and NETTs.

	NEBTs	**NDBTs**	**BDBTs**	**BDBSs**	**C3AGs**
Canopy Top Height [m]	17	14	20	0.5	0.5
Canopy Bottom Height [m]	8.5	7	11.5	0.1	0.01

land unit.

CLM4.5 distinguishes between five boreal PFTs – needleleaf evergreen boreal trees (henceforth, NEBTs), needleleaf deciduous boreal trees (henceforth, NDBTs), broadleaf deciduous boreal trees (henceforth, BDBTs), broadleaf deciduous boreal shrubs (henceforth, BDBSs), and C3 arctic grasses (henceforth, C3AGs). Transitions between biomes are smooth in CLM4.5 as fractional coverage by PFTs allows for vegetation types blending into each other and consequently, temperate PFTs blend into boreal forests. For this thesis, only needleleaf evergreen temperate trees (henceforth, NETTs) are of interest in addition to boreal PFTs, and fractional coverages by these six PFTs are shown in Figure 2.1. Present-day PFT coverage in CLM4.5 is derived from the Moderate Resolution Imaging Spectroradiometer (MODIS) vegetation product as described by *Lawrence and Chase* (2007), but understory vegetation of forests is assumed as trees instead of grasses (*Oleson et al.*, 2013). Transient land cover simulations are possible for CLM4.5, however, PFT coverages were kept constant for simulations in this thesis.

Vegetation structure of each PFT is described by 4 variables – leaf area index (LAI), stem area index (SAI), canopy top height, and canopy bottom height. Both LAI and SAI express vegetation density as one-sided area of vegetation per unit ground surface area and are used to distinguish between green foliage and stems, branches, and dead leaves, respectively, e.g. for estimates of albedo or photosynthesis. By default, the biogeochemistry model in CLM4.5 is inactivate and parameters for vegetation structure are not calculated prognostically. This is adopted for simulations in this thesis and consequently, canopy heights are invariant in time and space, listed in Table 2.1 for boreal PFTs, while LAI and SAI values repeat fixed seasonal cycles. These seasonal cycles are linearly interpolated from monthly estimates in order to get daily values of LAI and SAI. Monthly values of LAI are derived from MODIS satellite data (*Lawrence and Chase*, 2007) and subsequently, SAI is calculated from LAI (*Zeng et al.*, 2002). Furthermore, each PFT in CLM4.5 has a prescribed set of parameters for root distribution controlling water uptake from the soil; aerodynamic parameters determining resistances to heat, moisture, and momentum transfer; photosynthetic parameters determining stomatal resistance, photo-

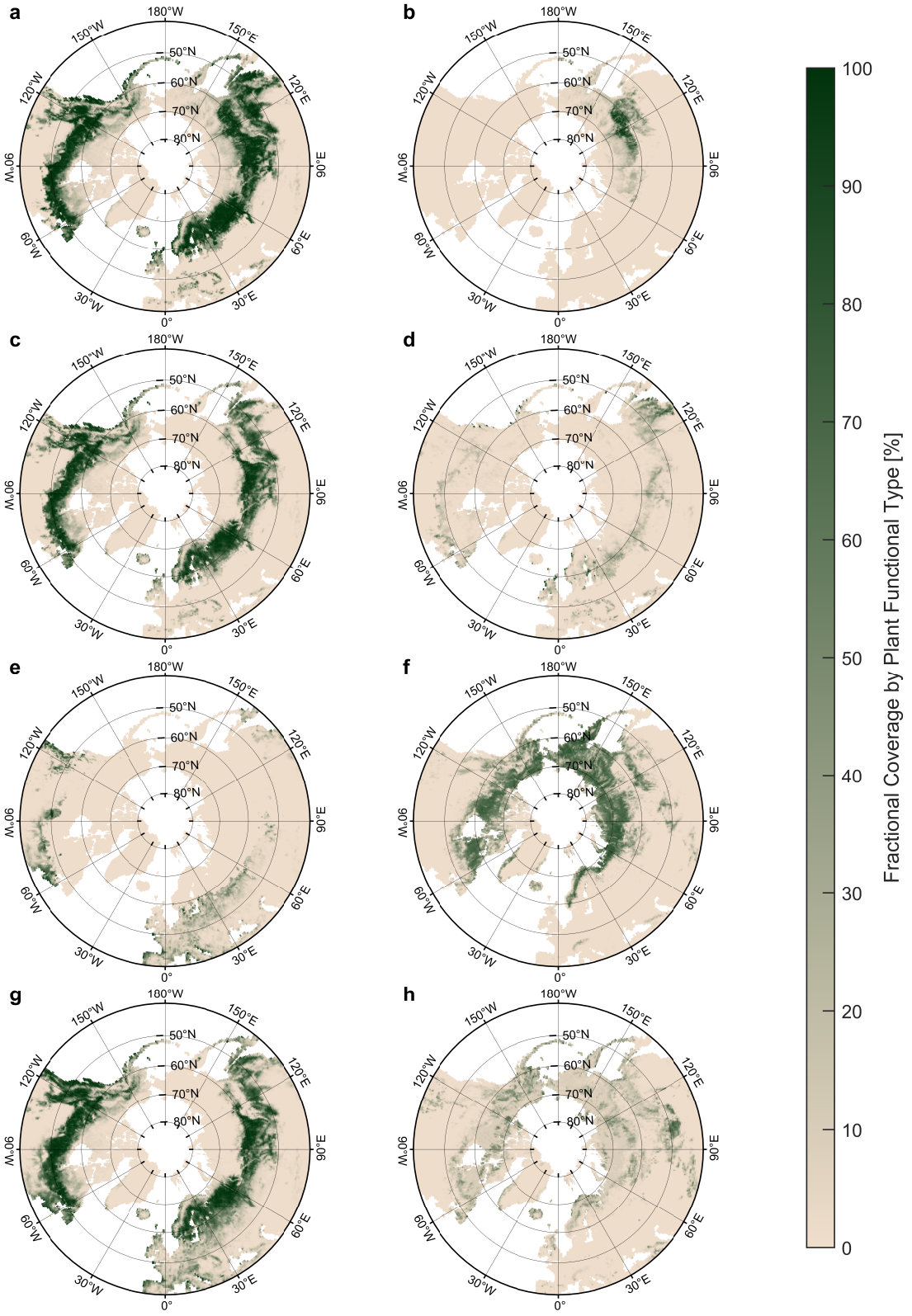

Figure 2.1: Coverage of vegetated land units by plant functional types for perennially snow-covered areas based on CLM4.5's high-resolution surface dataset ($0.3125° \times 0.2346°$): sum (**a**) of needleleaf deciduous boreal trees (**b**), needleleaf evergreen boreal trees (**c**), and broadleaf deciduous boreal trees (**d**); needleleaf evergreen temperate trees (**e**) and sum of needleleaf evergreen boreal and temperate trees (**g**); broadleaf deciduous boreal shrubs (**f**); and C3 arctic grasses (**h**).

synthesis, and transpiration; and optical properties for leaves and stems determining reflection, transmittance, and absorption of insolation, which are weighted by LAI and SAI (*Oleson et al.*, 2013). As for canopy top and bottom heights, these parameters are invariant in time and space.

Vegetation in CLM4.5 is parameterized as a single layer using a big-leaf approach (*Oleson et al.*, 2013), and the radiation scheme for vegetation is displayed in Figure 2.2. Generally, sub-canopy longwave radiation LW_{sub} is a weighted sum of atmospheric longwave radiation LW_{atm} and longwave radiation emitted by vegetation LW_{veg} (Equation (2.2)). In CLM4.5, vegetation emissivity ε_v used for weighing depends on LAI and SAI and is calculated as

$$\varepsilon_v = 1 - e^{-(LAI+SAI)}. \tag{2.5}$$

Usage of the term "emissivity" in CLM4.5 is misleading, since ε_v represents a combination of emissivity as used for the Stefan-Boltzmann law, which is an intrinsic property of material, and a scaling/weighing parameter based on vegetation density. This suggests that the actual emissivity of vegetation is assumed to be 1 and that ε_v solely represents vegetation coverage. However, there is no explanation for this in the technical description of CLM4.5 (*Oleson et al.*, 2013), and this thesis will stick to the naming convention of CLM4.5. Using the Stefan-Boltzmann law and Equation (2.2), sub-canopy longwave radiation in CLM4.5 is calculated as

$$LW_{sub} = (1 - \varepsilon_v)\, LW_{atm} + \varepsilon_v\, \sigma\, T_{veg}^4 \tag{2.6}$$

with vegetation temperature T_{veg}. This vegetation temperature is calculated by updating vegetation temperature from the previous time step via change in vegetation temperature from the previous to the current time step as

$$T_{veg}^4 = \big(T_{veg}(t-1)\big)^4 + 4\,\big(T_{veg}(t-1)\big)^3\,\big(T_{veg}(t) - T_{veg}(t-1)\big). \tag{2.7}$$

Calculation of vegetation temperatures in CLM4.5 is based on an energy balance, in which net radiation equals turbulent heat fluxes:

$$SW_{net} + LW_{net} = H + L \tag{2.8}$$

with net shortwave radiation SW_{net}, net longwave radiation LW_{net}, sensible heat flux H, and latent heat flux L. Radiative transfer of direct and diffuse shortwave radiation is calculated via a two-stream approximation for visual and near-infrared bands (*Sellers*, 1985; *Oleson et al.*, 2013) and depends on solar angle, vegetation density, ground albedo, intercepted precipitation, and PFT-specific optical properties. These properties are reflectivity and transmissivity, differentiated for visual and near-infrared bands as well as leaves and

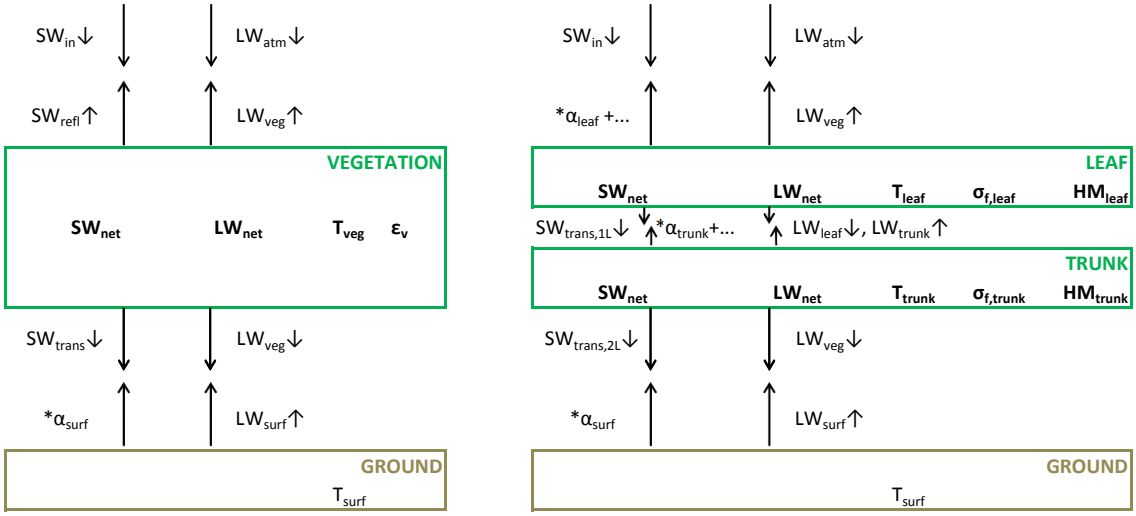

Figure 2.2: Radiation schemes of the big-leaf approach used in CLM4.5 (left) and interactive two-layer canopy used in SNOWPACK (right). Figures are adapted from *Oleson et al.* (2013) and *Gouttevin et al.* (2015), respectively. Dots "..." denote multiple reflections of shortwave radiation between layers in SNOWPACK. Note that $LW_{veg}\uparrow$ and $LW_{veg}\downarrow$ are equal by design in CLM4.5 but not in SNOWPACK, due to differing contributions from the vegetation layers. Also, $LW_{veg}\downarrow$ differs between CLM4.5 and SNOWPACK as seen in Equations (2.6) and (2.13).

stems, and departure of leaf angles from a random distribution. CLM4.5 considers a single reflection of shortwave radiation from the ground to the canopy. Note that CLM4.5 still lacks parameterizations for unloading of canopy interception when air temperatures are below $0^{\circ}\mathrm{C}$, as described for CLM4 by *Thackeray et al.* (2014), and that canopy interception is not distinguished between rain and snow. Net longwave radiation is calculated as

$$\begin{aligned} LW_{net} &= \varepsilon_v\, \varepsilon_g\, \sigma\, T_{surf}^4 \;+\; \varepsilon_v \left(1 + (1-\varepsilon_g)\,(1-\varepsilon_v)\right) LW_{atm} \\ &- \left(2 - \varepsilon_v\,(1-\varepsilon_g)\right) \varepsilon_v\, \sigma\, T_{veg}^4 \end{aligned} \tag{2.9}$$

with (ground) surface temperature T_{surf} and emissivity of the ground ε_g. Ground emissivity is a weighted sum of soil and snow emissivities, which are 0.96 and 0.97, respectively. In Equation (2.9), the first term represents longwave radiation emitted from the ground and absorbed by the vegetation; the second term represents atmospheric longwave radiation absorbed by the vegetation; and the third term represents longwave radiation emitted from the vegetation. Calculation of turbulent heat fluxes in CLM4.5 is based on Monin-Obukhov similarity theory and described by *Oleson et al.* (2013).

2.2.2 SNOWPACK

SNOWPACK is a one-dimensional snow model that was developed by Eidgenössische Forschungsanstalt für Wald, Schnee und Landschaft - Institut für Schnee- und Lawinenforschung (*Bartelt and Lehning*, 2002; *Lehning et al.*, 2002a,b), and to which a canopy module has been added. *Gouttevin et al.* (2015) improved the canopy module from a one-layer big-leaf vegetation scheme by addition of biomass heat storage and partitioning of the vegetation canopy into two interacting layers, an upper layer and a lower layer associated with different vegetation parts (leaves and trunk, respectively). SNOWPACK was developed for avalanche warning and is thus mostly limited to alpine environments. so that currently only evergreen needleleaf canopies are represented. As SNOWPACK is designed to run at individual locations, vegetation parameters are hard-wired and most of the input is site-specific. SNOWPACK is used in this thesis as a comparison and potential guideline for CLM4.5, and the radiation scheme for vegetation in SNOWPACK is displayed in Figure 2.2.

Sub-canopy longwave radiation in SNOWPACK is a combination of longwave radiation emitted by, and atmospheric longwave radiation passing through, the vegetation layers. Absorption factors determine the fractions of these components for each layer and are also used for shortwave radiation in contrast to the two-stream approximation used in CLM4.5. Absorption factor σ_f for longwave and diffuse shortwave radiation is calculated as a combination of absorption factors for both vegetation layers:

$$1 - \sigma_f = (1 - \sigma_{f,leaf})\,(1 - \sigma_{f,trunk}), \tag{2.10}$$

which are calculated as

$$\sigma_{f,leaf} = 1 - e^{-k_{LAI}\ f_{LAI}\ LAI} \tag{2.11}$$

and

$$\sigma_{f,trunk} = 1 - e^{-k_{LAI}\ (1-f_{LAI})\ LAI} \tag{2.12}$$

and adjusted for direct shortwave radiation using solar elevation angle. Absorption is spread across both vegetation layers depending on total LAI, i.e. the sum of both layers, with f_{LAI} determining the fraction assigned to the upper (leaf) layer. Calculation of total absorption σ_f is similar to the calculation of vegetation emissivity ε_v in CLM4.5 but additionally comprises an extinction coefficient k_{LAI}, the value of which is typically between 0.4 and 0.8 (*Gouttevin et al.*, 2015). The improved canopy module of SNOWPACK was calibrated at the subalpine site of Alptal, Switzerland with parameters set to $f_{LAI} = 0.5$ and $k_{LAI} = 0.75$, and emissivities of both vegetation layers were set to 1 to suppress multiple reflections. Calculation of sub-canopy longwave radiation is similar to Equation (2.6)

but absorption factors determine contributions of individual vegetation layers to LW_{veg}:

$$LW_{sub} = (1 - \sigma_f)\, LW_{atm} + (1 - \sigma_{f,trunk})\, \sigma_{f,leaf}\, \sigma\, T_{leaf}^4 + \sigma_{f,trunk}\, \sigma\, T_{trunk}^4 \quad (2.13)$$

with vegetation temperatures of the respective layers T_{leaf} and T_{trunk} using the Stefan-Boltzmann equation. For the calibrated value of $f_{LAI} = 0.5$, absorption factors of both layers are equal and the lower layer exhibits a higher impact on sub-canopy longwave radiation than the upper layer.

Vegetation temperatures in SNOWPACK are calculated via energy balances for each layer, in which net radiation equals turbulent and biomass heat fluxes:

$$SW_{net} + LW_{net} = H + L + BM \quad (2.14)$$

with biomass heat flux BM. Net radiation exceeding turbulent heat fluxes results in net energy uptake and a positive biomass heat flux indicating heat storage. When turbulent heat fluxes exceed net radiation, biomass heat flux is negative indicating a release of heat. Biomass heat flux BM_i of vegetation layer i (leaf or trunk) is parameterized by a temperature change for time step Δt and heat mass of vegetation:

$$BM_i(t) = HM_i\, \frac{T_i(t) - T_i(t-1)}{\Delta t}. \quad (2.15)$$

Heat mass HM_i is calculated as

$$HM_{leaf} = LAI\, e_{leaf}\, \rho_{biomass}\, C_{p,biomass} \quad (2.16)$$

and

$$HM_{trunk} = 0.5\, B\, z_{can}\, \rho_{biomass}\, C_{p,biomass}, \quad (2.17)$$

depending on biomass specific heat mass $C_{p,biomass}$ = 2800 $\mathrm{Jkg^{-1}K^{-1}}$, biomass density $\rho_{biomass}$ = 900 $\mathrm{kg\ m^{-3}}$, typical leaf thickness e_{leaf} = 0.001m, LAI, canopy height z_{can}, and dimensionless stand basal area B. Net shortwave radiation is calculated as

$$SW_{net,leaf} = SW_{in}\, (1 - \alpha_{leaf})\, \sigma_{f,leaf} \left(1 + \frac{\alpha_{surf}\, (1 - \sigma_{f,leaf})\, (1 - \sigma_{f,trunk})}{1 - \sigma_{f,leaf}\, \alpha_{surf}\, \sigma_{f,trunk}}\right) \quad (2.18)$$

and

$$SW_{net,trunk} = SW_{in}\, (1 - \sigma_{f,leaf})\, (1 - \alpha_{trunk})\, \sigma_{f,trunk} \quad (2.19)$$

for the leaf layer and trunk layer, respectively, with insolation SW_{in}, (ground) surface albedo α_{surf}, albedo of the leaf layer α_{leaf}, and albedo of the trunk layer α_{trunk}. Note that only shortwave radiation transmitted by the upper layer is assumed to reach the lower layer. The second term in brackets in Equation (2.18) represents multiple reflections

between upper layer and ground surface, which are assumed to be unaffected by the lower layer. Net longwave radiation is calculated as

$$LW_{net,leaf} = \sigma_{f,leaf} \left(LW_{atm} + \varepsilon_g \, \sigma \, T_{surf}^4 \, (1 - \sigma_{f,trunk}) + \sigma_{f,trunk} \, \sigma \, T_{trunk}^4 - 2 \, \sigma \, T_{leaf}^4 \right) \tag{2.20}$$

and

$$LW_{net,trunk} = \sigma_{f,trunk} \left(LW_{atm} \, (1 - \sigma_{f,leaf}) + \varepsilon_g \, \sigma \, T_{surf}^4 + \sigma_{f,leaf} \, \sigma \, T_{leaf}^4 - 2 \, \sigma \, T_{trunk}^4 \right) \tag{2.21}$$

for the leaf layer and trunk layer, respectively. Note that by default, vegetation emissivities as well as ground emissivity are set to 1 in order to suppress multiple reflections (*Gouttevin et al.*, 2015), however, ground emissivity can be modified in SNOWPACK and is included in this thesis for comparison with CLM4.5. Turbulent fluxes are calculated using bulk formulations, with latent heat fluxes being assumed to occur only at the leaf level and consequently restricted to the upper layer (*Gouttevin et al.*, 2015). Interaction between the two layers in SNOWPACK is included in: 1) net shortwave radiation via shading of the lower layer by the upper layer; and 2) net longwave radiation as a layer emits longwave radiation upward and downward impacting the respective layer above or below.

3 Synthesis of forest-stand measurements of longwave enhancement

Evaluation of simulated longwave enhancement can only be performed on a process level, which necessitates forest stand-scale measurements of sub-canopy longwave radiation. Seven forest stands were identified to feature both measurements of sub-canopy longwave radiation and sufficient data for driving model simulations. These forest stands as well as measurements of sub-canopy longwave radiation are described in the following and subsequently used to give an overview of longwave enhancement.

3.1 Forest stands

3.1.1 Alptal, Switzerland

The Alptal valley in central, subalpine Switzerland, at an altitude of approximately 1220m, has been a focus of snow observations by the Swiss Federal Institute for Forest, Snow and Landscape Research WSL for more than 40 years (*Keller and Strobel*, 1977). An instrument setup had been deployed in 2004 in order to retrieve spatial measurements of sub-canopy shortwave and longwave radiation, both upward and downward, which is described by *Stähli et al.* (2009) and shown in Figure 3.1. Moving radiometers had been installed on a rail of 10m length covering one length of the rail every 10 minutes. The rail setup had been removed in 2007 so that measurements were available for snowmelt seasons 2004 to 2007. Sub-canopy longwave radiation measurements have subsequently been used by *Gouttevin et al.* (2015), who tested and calibrated SNOWPACK with data from this site, and *Webster et al.* (2016a).

Figure 3.1: Rail setup for measurements of downward and upward shortwave and longwave radiation that had been deployed at the forest stand in the Alptal valley, Switzerland. Photo taken from *Essery et al.* (2009).

Norwegian spruce (*Picea abies*, 85%) and silver fir (*Abies alba*, 15%) dominate vegetation at the forest stand, indicating canopies are evergreen and constant canopy density can be assumed throughout the snowmelt season. Trees reach heights of 25m (*Rutter et al.*,

2009; *Stähli et al.*, 2009) and an average tree diameter of $1\mathrm{m}$ was used by *Gouttevin et al.* (2015). Stand basal area was given as 41 $\mathrm{m^2 ha^{-1}}$ by *Stähli et al.* (2009) and *Gouttevin et al.* (2015). Both stand basal area and leaf area index (LAI) vary throughout the forest with ranges of 27 $\mathrm{m^2 ha^{-1}}$ to 75 $\mathrm{m^2 ha^{-1}}$ and 3.1 $\mathrm{m^2\ m^{-2}}$ to 6.4 $\mathrm{m^2 m^{-2}}$, respectively, given by *Stähli and Gustafsson* (2006). Consequently, studies give different LAI values for Alptal, for example, mean stand LAI of 3.9 $\mathrm{m^2 m^{-2}}$ (*Gouttevin et al.*, 2015) and total LAI of 4.2 $\mathrm{m^2 m^{-2}}$ (*Rutter et al.*, 2009), while *Stähli et al.* (2009) give a range of 3.8 $\mathrm{m^2 m^{-2}}$ to 4.5 $\mathrm{m^2 m^{-2}}$ for LAI along the rail based on hemispheric photography. Total LAI includes woody parts and thus represents plant area index (PAI), the sum of LAI and stem area index (SAI). This suggests that LAI values given by *Stähli et al.* (2009) and *Gouttevin et al.* (2015) also represent PAI, especially when based on hemispheric photography. Therefore, an average of 4.1 $\mathrm{m^2 m^{-2}}$ along the rail was assumed as PAI.

3.1.2 Seehornwald, Switzerland

In 2007, the rail setup had been moved from Alptal to another WSL research site, a forest stand at Seehornwald near Davos, Switzerland, at an altitude of approximately $1640\mathrm{m}$. The rail setup is shown in Figure 3.2 and had been deployed until 2012, so that measurements were available for snowmelt seasons 2008 to 2012, which have previously been used by *Webster et al.* (2016a,b). Similar to Alptal, Norwegian spruce is the dominating tree species at Seehornwald and forest stand height is $25\mathrm{m}$ with maximum heights of $27\mathrm{m}$ (*Webster et al.*, 2016b; *Zweifel et al.*, 2016). However, average tree diameter and tree density are different compared to the forest stand at Alptal, which can be seen in Figures 3.1 and 3.2. Stand basal area was calculated from figures for number of trees (498 with diameter at breast height larger than $12\mathrm{cm}$), tree diameter ($47\mathrm{cm}$, "quadratic average diameter of the 100 thickest trees per ha"),

Figure 3.2: Rail setup for measurements of downward and upward shortwave and longwave radiation that had been deployed at the forest stand near Seehornwald, Switzerland. Photo taken from *Webster et al.* (2016b).

and plot size (0.6ha) given online by the Swiss Long-Term Forest Ecosystem Research (LWF) programme (www.wsl.ch/en/forest/forest-development-and-monitoring/long-term-forest-ecosystem-research-lwf/sites.html), yielding 144 $\mathrm{m^2 ha^{-1}}$. LAI is given by *Webster et al.* (2016b) as 3.9 $\mathrm{m^2 m^{-2}}$, which is not assumed as PAI in contrast to Alptal because Seehornwald features a substantially higher stand basal area than Alptal indicating a higher vegetation density.

3.1.3 Sodankylä, Finland

During March and April 2012, two arrays of radiometers had been deployed near Sodankyä in northern Finland in order to measure downward sub-canopy shortwave and longwave radiation (*Reid et al.*, 2014a). These arrays had consisted of 14 radiometers, 10 for shortwave radiation and 4 for longwave radiation, across a $20\mathrm{m}$-by-$20\mathrm{m}$ plot, so that measurements could be used to represent spatial averages. Radiometers had been checked and quality controlled in the field on a daily basis. One of these arrays had been moved across 4 locations of different vegetation types remaining in one location for no more than 8 days, which was considered too short for this study and consequently, measurements by the "roving" radiometer were not used. The other array had been deployed continuously in one location, listed as site C by *Reid et al.* (2014a), measurements of which had covered 23 days and were used for this thesis.

Figure 3.3: Pine forest near Sodankylä, Finland for which measurements of downward shortwave and longwave radiation were provided. Photo provided by Nick Rutter.

The forest at site C, shown in Figure 3.3, consists solely of Scots pine trees (*Pinus sylvestris*) with an average tree height of $18\mathrm{m}$ (*Hancock et al.*, 2014). Based on a tree survey, average tree diameter and stand basal area were calculated for the $20\mathrm{m}$-by-$20\mathrm{m}$ plot at site C, which yielded $11.6\mathrm{cm}$ and 20 $\mathrm{m^2 ha^{-1}}$, respectively. PAI estimates from hemispheric photos range from 1.09 $\mathrm{m^2 m^{-2}}$ to 1.22 $\mathrm{m^2 m^{-2}}$ across the four locations of radiometers for longwave radiation and average 1.14 $\mathrm{m^2 m^{-2}}$, which indicates spatial homogeneity in vegetation density. As the forest at site C consists of evergreen vegetation, PAI values were assumed as constant throughout the measurement period.

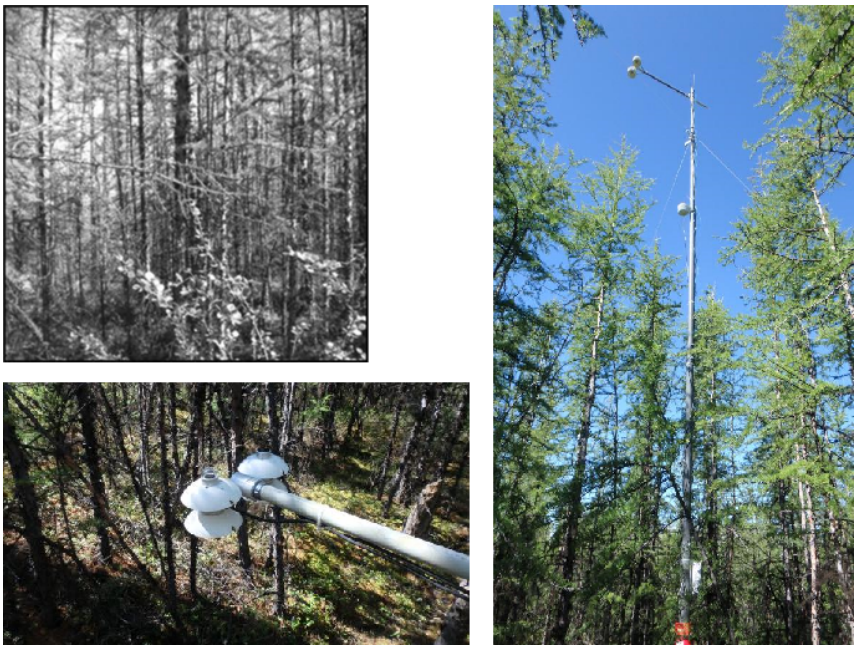

Figure 3.4: Photo taken from *Alexander et al.* (2012) depicting a typical high-density larch forest stand near Cherskiy, Russia (top left). Instrumentation tower (right) and sub-canopy radiometers (bottom left) at the forest stand near Cherskiy, Russia; photos taken from https://www.polartrec.com/expeditions/vegetation-impacts-on-permafrost/journals/2016-06-30.

3.1.4 Cherskiy, Russia

An instrument tower had been installed in 2016 within a forest stand near Cherskiy, Russia in northeastern Siberia (Figure 3.4). Among the instruments had been 8 radiometers for measurement of downward and upward shortwave and longwave radiation, both above and beneath the canopy, which subsequently covered the snowmelt season 2016/17. Measurements were made available online by *Kropp* (2018), and radiation measurements were quality controlled for snow cover on radiometers.

Description of the forest stand is given by *Alexander et al.* (2012), where it is listed as stand 13. The forest stand consists of Cajander larch (*Larix cajanderi*), which had regrown after a fire about 70 years earlier, and differs in vegetation structure compared to the previously described forest stands as trees are smaller and thinner (Table 3.1). Canopy tops reach heights of $5\mathrm{m}$, in contrast to mean stand height of $3.4\mathrm{m}$ given by *Alexander et al.* (2012), and tree density is 3.7 trees m^{-2}. Based on tree basal area and tree density, both given by *Alexander et al.* (2012), stand basal area was calculated as 48 $\mathrm{m}^2\mathrm{ha}^{-1}$, which is similar to Alptal and about twice as high as for Sodankylä. Larch trees had been leafless throughout the evaluation period and consequently, LAI was assumed as 0. In lieu of measurements, SAI was estimated as the lateral surface area of conical trees based on tree height and tree diameter, which yielded 0.67 $\mathrm{m}^2\mathrm{m}^{-2}$. Although stand basal area

is larger compared to Sodankylä, substantially smaller tree heights lead to lower PAI for the forest stand near Cherskiy.

3.1.5 Abisko, Sweden

The radiometer arrays described for Sodankylä had been deployed in a forest stand near Abisko in northern Sweden during March 2011. Similar to the forest stand near Sodankylä, the "roving" radiometer array had remained for only 3 to 4 days in individual locations within the forest stand, which was deemed too short for the purpose of this thesis. Descriptions of the forest stand location for the "continuity" radiometer array are given by *Reid et al.* (2014a,b), where it is listed as site C out of multiple sites at Abisko, and sub-canopy longwave radiation had been quality controlled by *Reid et al.* (2014a). The forest stand consists of patchy, polycormic mountain birch (*Betula pubescens*) with heights ranging from $2\mathrm{m}$ to $4\mathrm{m}$ and a mean canopy height of $3.5\mathrm{m}$ (Figure 3.5). Average tree diameter of $3.8\mathrm{cm}$ and stand basal area of 6.1 $\mathrm{m^2 ha^{-1}}$ were calculated for the $20\mathrm{m}$-by-$20\mathrm{m}$ plot at site C based on a tree survey, and the value for stand basal area differs slightly from 7.8 $\mathrm{m^2 ha^{-1}}$ given by (*Reid et al.*, 2014b). PAI estimates based on hemispheric photos range from 0.14 $\mathrm{m^2 m^{-2}}$ to 0.70 $\mathrm{m^2 m^{-2}}$ across four radiometer locations, indicating considerable spatial heterogeneity in vegetation density, and yield a spatial average of 0.44 $\mathrm{m^2 m^{-2}}$. Birch trees had been leafless throughout the evaluation period and consequently, LAI was assumed as 0 while SAI was assumed to be PAI.

Figure 3.5: Typical birch forest near Abisko, Sweden for which measurements of downward shortwave and longwave radiation were provided. Photo provided by Nick Rutter.

3.1.6 Yakutsk, Russia

Figure 3.6: Larch forest near Yakutsk, Russia for which measurements of sub-canopy net and shortwave radiation were provided. Photo taken from *Suzuki et al.* (2001).

Radiometers had been deployed for consecutive winters from 1997/98 to 1999/00 in a forest stand north of Yakutsk, Russia, however, measurements of sub-canopy longwave radiation were unavailable. For the snowmelt season in 1998, measurements of sub-canopy net all-wave radiation, downward and upward sub-canopy shortwave radiation, and surface temperature were available and subsequently, sub-canopy longwave radiation was estimated as a residual. However, incoming shortwave radiation beneath the canopy displayed large fluctuations compared to outgoing shortwave radiation resulting in occasional negative net shortwave radiation, which had potentially been caused by the usage of a single radiometer. Consequently, only nighttime sub-canopy longwave radiation was used for this study.

The forest stand, shown in Figure 3.6, consists of Dahurica larch (*Larix gmelinii*) with a mean stand height of $18\mathrm{m}$. A description of the forest stand is given by *Ohta et al.* (2001), which includes diameters and heights of four trees that had been used for sap flow measurements. Stand-average tree diameter was estimated as $25\mathrm{cm}$ by applying the ratio of diameter to height from those four trees to mean stand height. Subsequently, stand basal area was calculated from mean tree diameter and stand density of 840 trees ha^{-1} given by *Ohta et al.* (2001), which yielded 43 $\mathrm{m}^2\mathrm{ha}^{-1}$. PAI values, obtained from analysis of hemispheric photographs, range from 1.71 $\mathrm{m}^2\mathrm{m}^{-2}$ in the leafless season to 3.71 $\mathrm{m}^2\mathrm{m}^{-2}$ in the foliated season (*Ohta et al.*, 2001). As trees had remained leafless throughout the snowmelt season, LAI was assumed as 0 and SAI was assumed as 1.71.

3.1.7 Borden, Canada

At the end of 2012, radiometers had been placed in a forest stand near Borden, Canada in southern Ontario, which provided sub-canopy shortwave and longwave radiation measurements for the snowmelt season in 2013. While downward shortwave radiation had been measured by a separate array of 12 radiometers, measurements of upward and downward shortwave and longwave radiation were only available for a single location within the forest stand. Radiometers had been checked for orientation in the field and sub-canopy

longwave radiation measurements were quality controlled for snow cover on radiometers. The forest stand consists of both deciduous broadleaf and evergreen needleleaf trees (Figure 3.7), with percentages of 81% and 19%, respectively, based on the most recent tree survey described by *Teklemariam et al.* (2009). Dominant species are red maple (*Acer rubrum*, 52%), eastern white pine (*Pinus strobus*, 14%), large-tooth aspen (*Populus grandidentata*, 8%), white ash (*Fraxinus americana*, 7%), and American beech (*Fagus grandifolia*, 6%). Stand-average tree diameter and stand basal area were estimated based on the tree survey described by *Teklemariam et al.* (2009) and diameters for individual tree species given by *Neumann et al.* (1989), which yielded 7.8cm and 15.7 $\mathrm{m^2 ha^{-1}}$, respectively. Post-leaf out LAI for the forest stand is given as 4.6 $\mathrm{m^2 m^{-2}}$ by *Croft et al.* (2015). Pre-leaf out stand PAI was measured as 1.36 $\mathrm{m^2 m^{-2}}$ and deciduous trees were leafless throughout the snowmelt season (*private communication with Paul Bartlett, Environment and Climate Change Canada*).

Figure 3.7: Aerial view from instrumentation tower at the mixed forest near Borden, Canada for which measurements of sub-canopy shortwave and longwave radiation were provided. Photo taken from *Croft et al.* (2015).

3.2 Observations of longwave enhancement and net snow surface radiation

Atmospheric longwave radiation and (near-)surface air temperatures had been measured in addition to sub-canopy longwave radiation for all forest stands. This allowed for the calculation of longwave enhancement and effective emissivity of the sky ε_{sky} (Equation (2.4)), the latter of which can be used to quantify meteorological conditions as described in Chapter 2.1. In the following, longwave enhancement is compared between forest stands as a function of ε_{sky}. Measurements are shown as hourly averages, so that measurements for the forest stands at Alptal and Seehornwald represent spatial averages along the rail. For forest stands at Abisko and Sodankylä, measurements of individual radiometers were used to calculate spatial averages. Only nighttime estimates of sub-canopy longwave radiation were used for the forest stand near Yakutsk due to inconsistencies in sub-canopy shortwave radiation.

Table 3.1: Forest stands used for comparison of longwave enhancement. *Analysis periods at Alptal start on 1 January except for 2004 (24 January). Dates for end of analysis period at Alptal are: 12 March 2004, 14 March 2005, 19 March 2006, and 4 April 2007. Analysis durations for Alptal are 41 days in 2004, 57 days in 2005, 73 days in 2006, and 85 days in 2007. **Dates for end of analysis period at Seehornwald are: 27 April 2008, 1 April 2009, 20 April 2010, 29 March 2011, 26 April 2012. Analysis durations for Seehornwald are 116 days in 2008, 90 days in 2009, 106 days in 2010, 83 days in 2011, and 116 days in 2012.

	Abisko	**Alptal**	**Borden**	**Cherskiy**	**Seehornwald**	**Sodankylä**	**Yakutsk**
Latitude	68.4°N	47.1°N	44.3°N	68.7°N	46.8°N	67.4°N	62.3°N
Longitude	18.8°E	8.8°E	79.9°W	161.4°E	9.9°E	26.6°E	129.6°E
Altitude	388m	1220m	222m	39m	1640m	179m	220m
Snowmelt season	2011	2004-07	2013	2017	2008-12	2012	1998
Analysis start	11 Mar	*	2 Jan	30 Mar	1 Jan	10 Mar	14 Feb
Analysis end	3 Apr	*	4 Apr	21 May	**	16 Apr	14 May
Analysis days	9	*	77	51	**	37	87
Vegetation	birch	spruce	mixed	larch	spruce	pine	larch
Tree Height	3.5m	25m	22m	5m	25m	18m	18m
Tree Diameter	3.8cm	100cm	7.8cm	1.7cm	40cm	11.6cm	25.6cm
Stand Basal Area [$m^2 ha^{-1}$]	6	41	16	48	144	20	43
PAI [$m^2 m^{-2}$]	0.44	4.1	1.36	0.67	>3.9	1.14	1.71

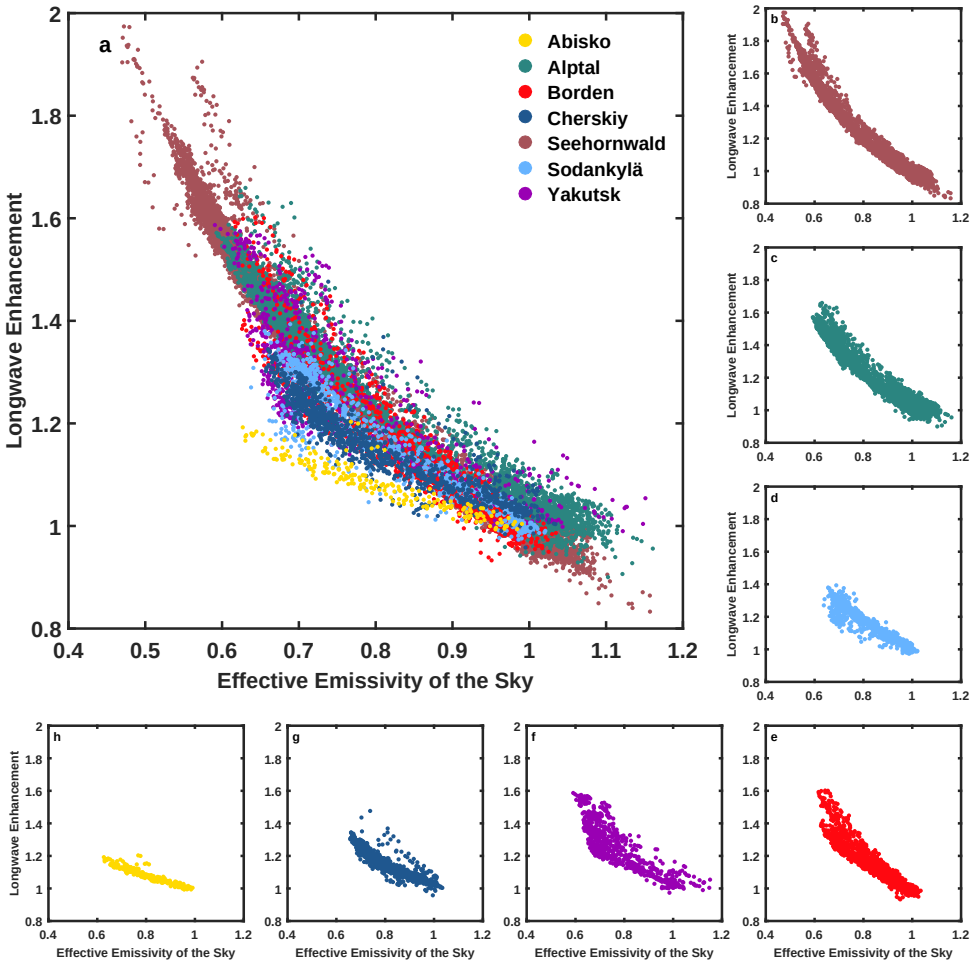

Figure 3.8: Comparison of longwave enhancement as a function of effective emissivity of the sky for hourly measurements at all forest stands (**a**) and individual forest stands at Seehornwald (maroon, **b**), Alptal (green, **c**), Sodankylä (light blue, **d**), Borden (red, **e**), Yakutsk (violet, **f**), Cherskiy (dark blue, **g**), and Abisko (yellow, **h**). Note that only nighttime measurements are displayed for Yakutsk.

Measurements reveal longwave enhancement increasing continuously with clearer skies for each forest stand (Figure 3.8). Longwave enhancement values are close to 1 for overcast conditions at each forest stand, indicating little to no impact of vegetation. Longwave enhancement values can be below 1 for ε_{sky} values larger than 1, which is common for the densest forest stand at Seehornwald. Highest longwave enhancement occurs for clear skies but varies with vegetation density across forest stands. Highest clear-sky longwave enhancement had been measured for dense forest stands at Alptal and Seehornwald, reaching values of up to 1.6 for the same range of ε_{sky}. However, lower ε_{sky} at Seehornwald, which is likely caused by higher elevation, leads to higher maximum longwave enhancement compared to Alptal, reaching values of up to 2. Clear-sky longwave enhancement values decrease with vegetation density from between 1.3 and 1.4 at So-

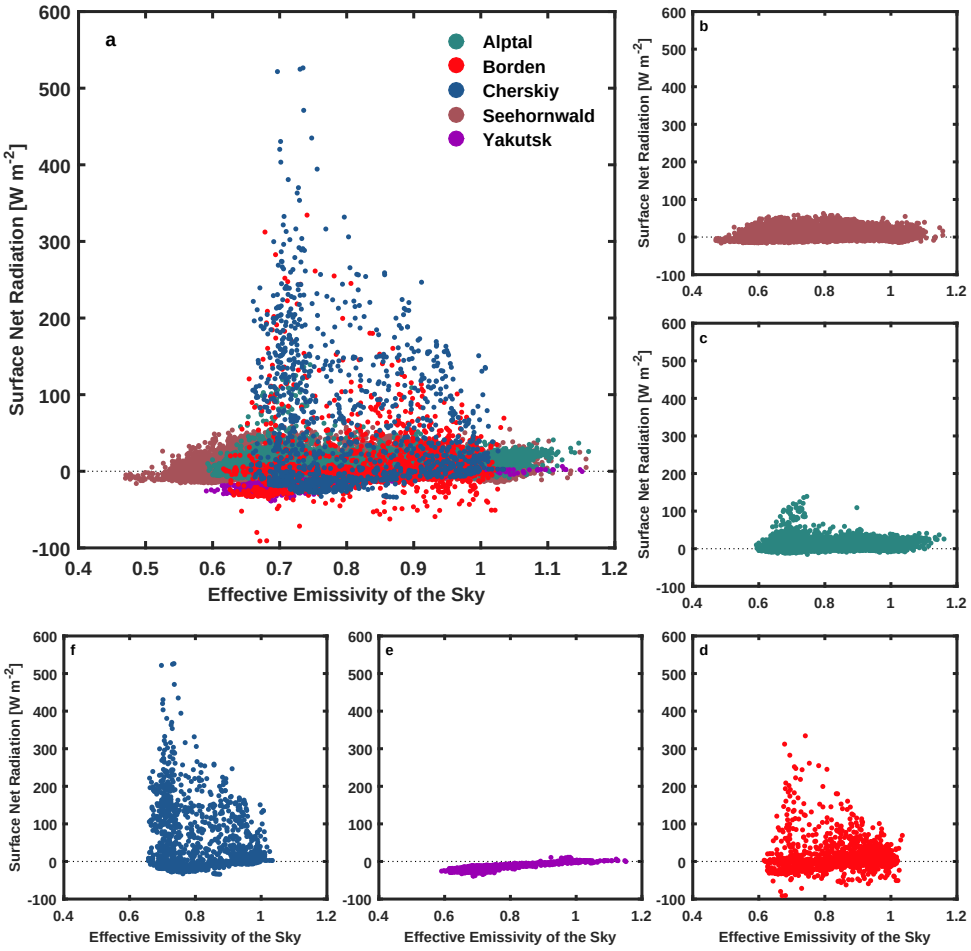

Figure 3.9: Comparison of snow surface net radiation as a function of effective emissivity of the sky for hourly measurements at all forest stands for which data were available (**a**) and individual forest stands at Seehornwald (maroon, **b**), Alptal (green, **c**), Borden (red, **d**), Yakutsk (violet, **e**), and Cherskiy (dark blue, **f**). Note that only nighttime measurements are displayed for Yakutsk.

dankylä to about 1.3 at Cherskiy and 1.2 at Abisko. Longwave enhancement is similar at Cherskiy and Sodankylä, although vegetation at Cherskiy is more similar to Abisko in terms of PAI and vegetation type. Spread in longwave enhancement for constant ε_{sky} is generally small except for Borden and Yakutsk, where clear-sky longwave enhancement is mostly similar to Cherskiy and Sodankylä but also reaches up to values of dense forest stands at Alptal and Seehornwald.

For 4 of the 7 forest stands (Alptal, Borden, Cherskiy, and Seehornwald) measurements of downward and upward shortwave and longwave radiation beneath the canopy were available, which allowed for the calculation of net radiation at the snow surface. For the forest stand near Yakutsk, measurements of sub-canopy net radiation were available. Measurements from these five forest stands can be used to illustrate the influence of vegetation density on snowmelt and are shown against measurements of ε_{sky} in Figure 3.9.

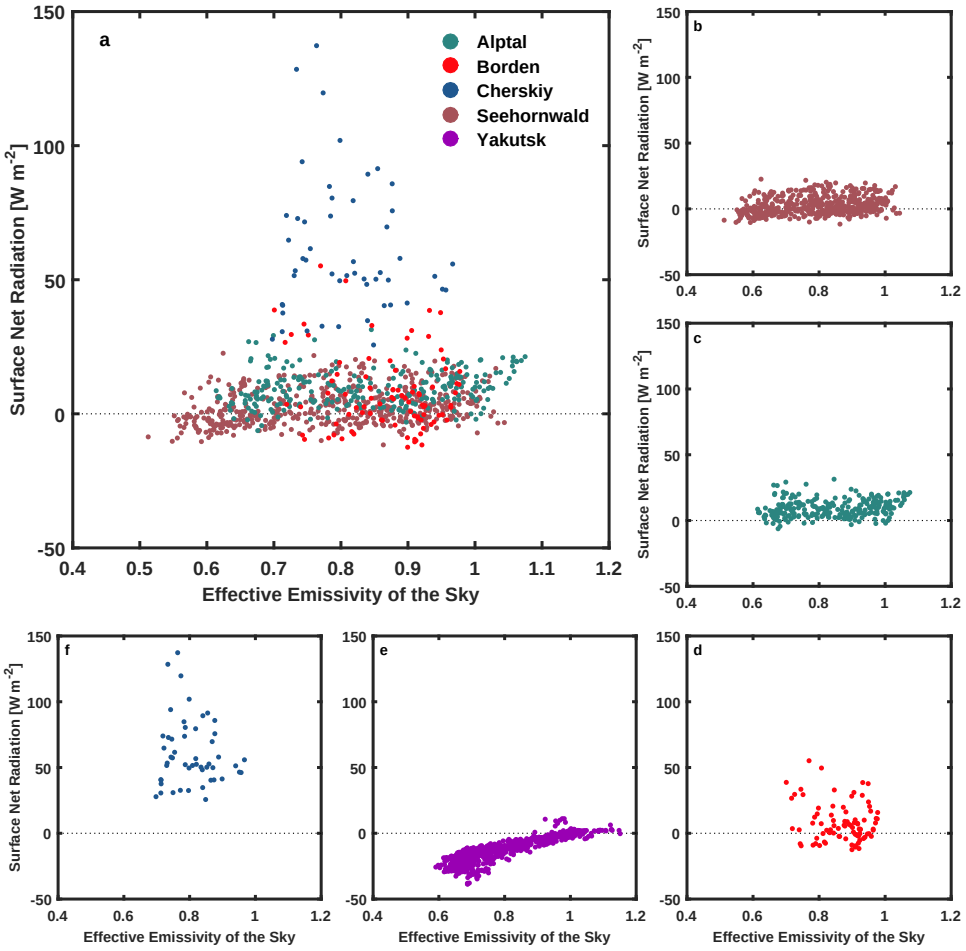

Figure 3.10: Comparison of snow surface net radiation as a function of effective emissivity of the sky for daily averages of measurements at all forest stands for which data were available (**a**) and individual forest stands at Seehornwald (maroon, **b**), Alptal (green, **c**), Borden (red, **d**), Yakutsk (violet, **e**), and Cherskiy (dark blue, **f**)). Note that Yakutsk is excluded from panel **a** and only nighttime measurements are displayed in panel **e**.

Throughout the five snow seasons of observations at Seehornwald, hourly values of sub-canopy net radiation range between -20 Wm^{-2} and 100 Wm^{-2}. Similarly for Alptal, sub-canopy net radiation only rarely exceeds that range and daytime values never exceed 200 Wm^{-2}. These small ranges for Alptal and Seehornwald are due to the dense canopies, which dampen diurnal variations. In contrast, sub-canopy net radiation ranges from -40 Wm^{-2} to 600 Wm^{-2} at the forest stand near Cherskiy and from -90 Wm^{-2} to 400 Wm^{-2} at the forest stand near Borden. While the magnitude of minimum sub-canopy net radiation does not display a dependence on ε_{sky} for dense forests at Alptal and Seehornwald, minimum sub-canopy net radiation values decrease with clearer skies for deciduous forest stands, which is illustrated by nighttime values for Yakutsk (Figure 3.9e).

In order to illustrate the implications for snowmelt, daily averages of sub-canopy net

radiation were calculated (Figure 3.10). Daily averages of sub-canopy net radiation do not exceed the range from -10 Wm^{-2} to 30 Wm^{-2} for the forests at Alptal and Seehornwald, and values for Alptal are almost exclusively positive. Daily averages for Borden are similar to Alptal and Seehornwald, but they can reach up to and exceed 50 Wm^{-2}. For the forest stand near Cherskiy, daily averages of sub-canopy net radiation are consistently positive and range from 20 Wm^{-2} to 150 Wm^{-2}.

3.3 Discussion

Higher vegetation density leads to a higher contribution from vegetation to sub-canopy longwave radiation. Consequently, denser forest stands feature higher longwave enhancement for clear-sky conditions. Under overcast skies, higher contribution from vegetation does not impact longwave enhancement due to the small contrast between vegetation temperatures and radiative temperature of the sky. However, the increase of clear-sky longwave enhancement with vegetation density is not linear as indicated by the dense forest stands at Alptal and Seehornwald. Despite featuring different vegetation densities, forest stands at Alptal and Seehornwald display virtually the same longwave enhancement values for the same range of ε_{sky}. Saturation of canopy coverage for very high vegetation density is usually expressed using an exponential function, as can be seen for vegetation emissivity ε_v in CLM (Equation (2.5)) and absorption factor σ_f in SNOWPACK (Equation (2.10)). At both Alptal and Seehornwald, where little atmospheric longwave radiation is transmitted due to dense canopies, there is a roughly inverse relationship between longwave enhancement and ε_{sky}. This is due to atmospheric longwave radiation being used to calculate both longwave enhancement and ε_{sky} and indicates temperatures of dense canopies can generally be approximated by above-canopy air temperatures.

Measurements show that hourly longwave enhancement values can reach up to 2, i.e. a doubling of atmospheric forcing, for dense forest canopies and clear skies. As atmospheric longwave radiation decreases with clearer skies, longwave enhancement reduces variations in longwave radiation beneath forest canopies compared to open areas. Even for (predominately) deciduous forest stands near Borden and Yakutsk, longwave enhancement values can reach hourly averages of 1.6. Longwave enhancement at those two forest stands exhibits higher spread for constant ε_{sky}, which might be due to spatial heterogeneity of vegetation. Absorption and transmissivity of evergreen and deciduous trees differ substantially and consequently, distribution of tree species around the single radiometer at the mixed forest stand near Borden likely has an impact on measured longwave enhancement based on time of day, via solar azimuth, and time of year, via solar elevation. In contrast, there is little spread in measurements for dense canopies at the forest stands

near Alptal and Seehornwald and for rather uniform deciduous vegetation at the forest stand near Cherskiy. However, deciduous vegetation might be too sparse and analysis period might be too short for spread in measurements at the forest stand near Abisko. Also, longwave enhancement values of less than 1 can occur when extensive cloud cover increases atmospheric longwave radiation and limits insolation reaching the vegetation. This happens frequently for dense forest stands, which reaffirms that forests can act as cold air sinks due to suppressed turbulent fluxes (*Link and Marks*, 1999b; *Webster et al.*, 2016a).

The overview given in this chapter is a novel illustration of the workings of longwave enhancement. So far, longwave enhancement had only been reported for individual forest stands and for periods of several days, apart from the measurements at Alptal and Seehornwald that were used in this thesis (*Webster et al.*, 2016a). Therefore, the continuous increase of longwave enhancement with clearer skies and its dependence on vegetation density had not been highlighted yet. Nevertheless, snapshots provided by previous studies can be used to fill gaps in the spectrum of vegetation density, especially for evergreen forest stands that are only represented by three sites in this thesis. Measurements in a medium-density pine forest stand near Fraser, USA display longwave enhancement values of up to 1.35 on clear-sky days and up to 1.2 on more overcast days (*Rowlands et al.*, 2002; *Sicart et al.*, 2004). Measurements in an open forest stand at the same location display longwave enhancement values of up to 1.25 on clear-sky days and up to 1.1 on more overcast days (*Rowlands et al.*, 2002; *Sicart et al.*, 2004). These measurements confirm the increase of longwave enhancement with denser vegetation and clearer skies. Moreover, these longwave enhancement values are similar to measurements from the forest stand near Sodankylä, which also features pine trees with medium vegetation density. Pine trees at the forest stand near Fraser are smaller compared to the forest stand near Sodankylä, with heights of $12\mathrm{m}$ at the medium-density forest stand and $8\mathrm{m}$ at the more open forest stand, but PAI of the denser forest stand, $1.8\ \mathrm{m^2 m^{-2}}$, is higher compared to Sodankylä (*Hardy et al.*, 1997; *Sicart et al.*, 2004). Both forest stands near Fraser display longwave enhancement values less than 1 during overcast mornings, which suggests cold air pools beneath the canopies that delay increase in sub-canopy longwave radiation compared to atmospheric longwave radiation emitted from the cloudy sky. This supports findings for the dense forest stands at Alptal and Seehornwald despite substantially lower vegetation density at the pine forest stands near Fraser, which is at least partially due to smaller trees. Therefore, a parameter that can represent tree density, such as stand basal area, might be more indicative of cold air pooling in forest stands than PAI or LAI.

Longwave enhancement values of 1.5 on clear-sky days have been measured for a dense

spruce forest in the subarctic Wolf Creek Research Basin, Canada, where trees range from $12\mathrm{m}$ to $18\mathrm{m}$ with PAI of 3.3 $\mathrm{m}^2\mathrm{m}^{-2}$ (*Pomeroy et al.*, 2002; *Sicart et al.*, 2004). This longwave enhancement value is smaller than measurements at the spruce forest stands near Alptal and Seehornwald, which feature taller and slightly more dense vegetation, but larger than measurements at the less dense pine forest stands near Fraser and Sodankylä. Longwave enhancement of up to 1.5 is also displayed by 15-minute averaged measurements for a pine forest stand in the high-altitude Marmot Creek Research Basin, Canada, where LAI is estimated to be roughly 2.1 $\mathrm{m}^2\mathrm{m}^{-2}$ based on hemispheric photographs (*Essery et al.*, 2008). Higher vegetation density as well as higher elevation and consequently lower ε_{sky} likely cause higher longwave enhancement values compared to other pine forest stands. Overall, the measurements of longwave enhancement in North American spruce and pine forests are consistent with the magnitude of clear-sky longwave enhancement and its increase with denser vegetation as presented in this thesis.

Vegetation coverage also reduces variations in sub-canopy net radiation, and this reduction increases with vegetation density. Below dense evergreen canopies at Alptal and Seehornwald, minimum net radiation is only slightly negative and higher than for deciduous forests near Borden, Cherskiy, and Yakutsk. Negative net radiation occurs during night, when there is no insolation and net radiation equals net longwave radiation. Longwave enhancement in dense forests results in net longwave radiation close to 0, while net longwave radiation is lower in sparse forests due to higher contribution from the atmosphere to sub-canopy longwave radiation. Clearer skies, indicated by low values of ε_{sky}, lead to less atmospheric longwave radiation and thus higher negative net radiation in absolute terms, which was most evident for Yakutsk. However, measurements in dense forests at Alptal and Seehornwald do not show this decrease with clearer skies, which indicates the sheltering effect of dense canopies. During daytime, denser vegetation shades the snow surface more substantially, resulting in lower values of net radiation. Highest sub-canopy net radiation occurs beneath the low-density forest stand near Cherskiy, as small deciduous vegetation leads to little shading during daytime while vegetation is dense enough to substantially enhance longwave radiation reducing nighttime cooling. Therefore, comparison of sub-canopy net radiation across forest stands supports findings that snowmelt generally decreases with increasing canopy coverage, due to shading outweighing longwave enhancement (*Yamazaki and Kondo*, 1992; *Sicart et al.*, 2004).

4 Forest stand-scale evaluation

As described in the introduction (Chapter 1) and shown in the previous chapter (Chapter 3), longwave enhancement is a process that has been observed to influence the surface energy balance and impact snowmelt in forests. However, its simulation by global climate models has not been assessed so far, which led to the formulation of Research Question 1: **How well is longwave enhancement simulated in global climate models? Can increasing complexity of canopy representation improve simulation of longwave enhancement in global climate models?**

CLM4.5 is chosen as a representative of global land models, as it is publicly available and uses a singe-layer vegetation scheme, which is a common approach in global climate models. In this chapter, simulation of sub-canopy longwave radiation and longwave enhancement by CLM4.5 is evaluated and compared to simulation by SNOWPACK, a one-dimensional snow model with a two-layer canopy module. Additionally, it is tested whether the implementation of a biomass heat storage in CLM4.5 can improve the simulation of sub-canopy longwave radiation and longwave enhancement by CLM4.5. This chapter has been published as *Simulation of Longwave Enhancement in Boreal and Montane Forests* in Journal of Geophysical Research: Atmospheres (*Todt et al.*, 2018).

4.1 Toy Model setup

Evaluation of sub-canopy longwave radiation and longwave enhancement simulated by CLM4.5 and comparison to simulations by SNOWPACK necessitate the usage of forest stand-scale forcing and evaluation data for both models. Therefore, full energy balance calculations of both models were extracted from their respective original model codes to calculate vegetation temperatures, which were subsequently used to calculate sub-canopy longwave radiation as outlined in Equations (2.6) and (2.13). Workflow and required inputs are shown in Figure 4.1. The Toy Model allows for a direct comparison as vegetation is conceptualized as layers in both CLM4.5 and SNOWPACK and mostly characterized by the same parameters. CLM4.5 subdivides grid cells based on land units and plant functional types (PFTs), however, usage of stand-scale forcing effectively results in the simulation of a single grid cell solely covered by the specific PFT(s) of a forest stand and consequently, the PFT coverage is 100%. This corresponds to the parameter throughfall fraction in SNOWPACK being set to 0, which is representative of complete canopy coverage and stand-scale averages.

The following assumptions and decisions were made to facilitate a direct comparison of CLM4.5 and SNOWPACK only focussing on differences in parameterizations of vegeta-

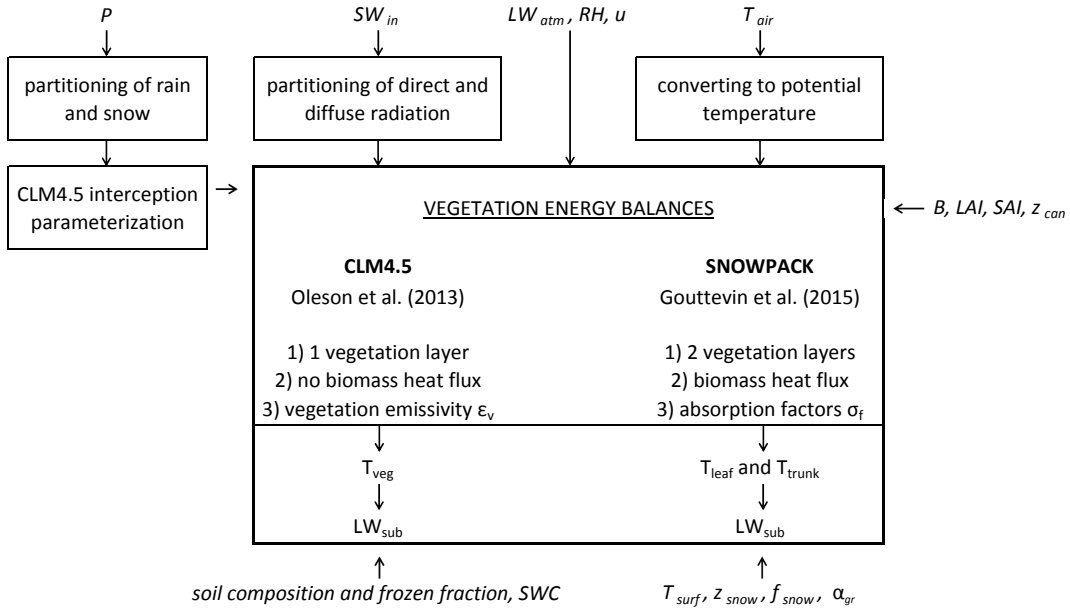

Figure 4.1: Schematic of Toy Model workflow. Symbols as in Equations (2.5), (2.6), (2.13), and (2.17). P denotes precipitation. SW_{in} denotes incoming shortwave radiation. RH denotes relative humidity. u denotes wind speed. T_{air} denotes air temperature. T_{surf} denotes surface temperature. z_{snow} denotes snow depth. f_{snow} denotes snow cover fraction. α_{gr} denotes ground albedo. SWC denotes soil water content.

tion energy balances. Hourly time steps were used for both models and all forest stand sites. Interception of precipitation calculated by CLM4.5 was also used for SNOWPACK. CLM4.5 distinguishes between 3 ground cover types, snow, soil, and surface water, in order to represent the distribution of wetlands. Since there are no observational data of ground coverage by water for forest stand sites, which also do not include wetlands, ground is only assumed to be snow-covered or not snow-covered (i.e. soil). This aligns with the representation of ground cover by CLM4. Albedo, emissivity, and roughness length for soil and snow were prescribed as the same for both models, using values and parameterizations from CLM4.5. CLM4.5 uses roughness length of soil only for a snow cover fraction of 0 and roughness length of snow otherwise. Ground albedo and emissivity were calculated as a combination of soil and snow values weighted by snow cover fraction. Emissivities of soil and snow in CLM4.5 are 0.96 and 0.97, respectively. Calculation of snow albedo by the SNICAR module in CLM4.5 (*Flanner and Zender*, 2005) was replaced with a simple ageing curve for forest-floor albedo used in SNOWPACK, which only required a set value for snow albedo and age of snow on the ground. Fresh snow albedo was set to 0.8 in the Toy Model except when noted, which is slightly lower than

the value of 0.84 used by *Pomeroy et al.* (1998). Insolation was assumed as visible since measurements of near-infrared shortwave radiation were not available and SNOWPACK does not distinguish between visible and near-infrared wavebands. A lapse-rate adjusted potential temperature, scaled from forcing height to surface, is used in CLM4.5 and this temperature was also used for SNOWPACK. Soil quantities were averaged vertically for CLM4.5 in lieu of consistent measurements of vertical profiles. Prescribed canopy top heights in CLM4.5 (Table 2.1) were replaced with values measured at the forest stand sites. Prescribed canopy bottom heights in CLM4.5 are only used to adjust vegetation for burying by snow, which was redundant since only tree PFTs were used for Toy Model simulations and burying by snow was therefore not possible.
The effect of a biomass heat storage parameterization on sub-canopy longwave radiation in CLM4.5 was tested, for which the parameterization used in SNOWPACK (Equations (2.15) - (2.17)) was implemented in CLM4.5 (henceforth, CLM4.5-BM). As in SNOWPACK, biomass heat flux was added to turbulent heat fluxes resulting in a vegetation energy balance of net radiation minus turbulent heat fluxes minus biomass heat flux. Biomasses of needles (Equation (2.16)) and trunks (Equation (2.17)) were combined for the single vegetation layer in CLM4.5-BM.

4.2 Forcing and evaluation data

The Toy Model was used to simulate sub-canopy longwave radiation for seven forest stands, which span a wide range of vegetation types and structures as well as meteorological conditions. Forest stands and measurements of sub-canopy longwave radiation that were used for evaluation are described in Chapter 3. Site characteristics are shown in Table 4.1, including type, height, and density of vegetation. Measurements of forcing variables and approximations, used if no measurements were available, are listed in Table 4.2 and described in the following, in addition to brief descriptions of stand characteristics. Sensitivity tests are given in Chapter 4.8.

Alptal, Switzerland Descriptions of the forest stand are given by *Rutter et al.* (2009), *Stähli et al.* (2009), and *Gouttevin et al.* (2015), the latter of which used data from this site to test and calibrate SNOWPACK. Sub-canopy longwave and shortwave radiation, both upward and downward, had been measured by a moving radiometer on a rail of $10\mathrm{m}$ length, which covered one length of the rail every 10 minutes representing a spatial average for each hourly time step. Sub-canopy longwave radiation measurements were checked for potential errors caused by snow cover on radiometers. Snow cover on radiometers was suspected when sub-canopy longwave radiation showed little changes

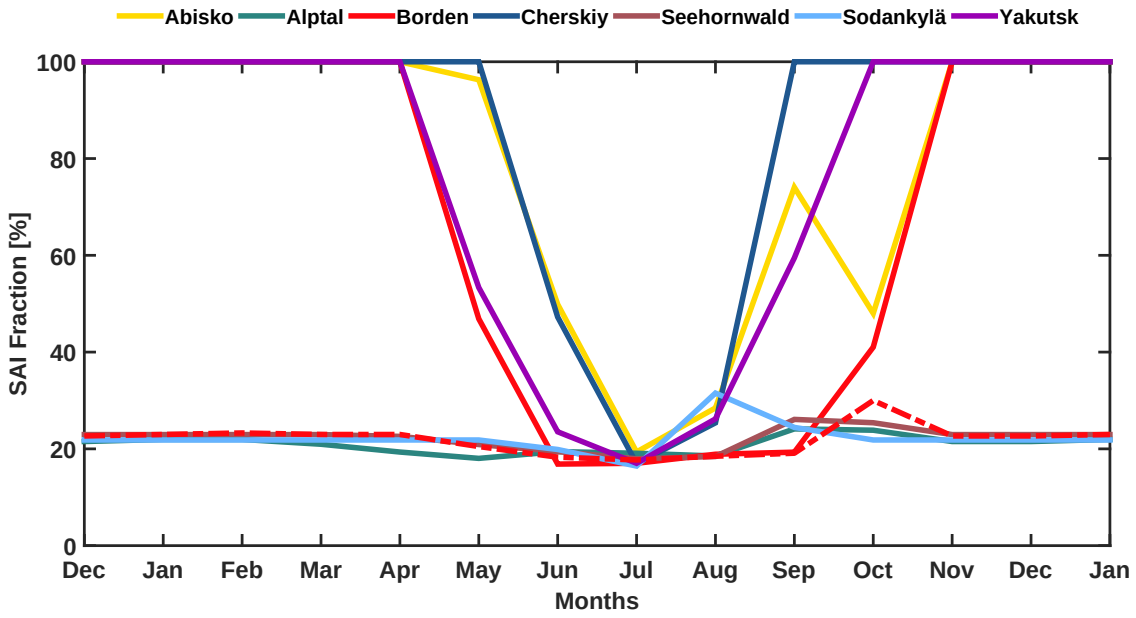

Figure 4.2: Seasonal cycle of stem area index (SAI) as a fraction of PAI taken from CLM4.5's high-resolution surface dataset ($0.3125° \times 0.2346°$) for corresponding grid cells and PFTs of forest stands at Abisko (yellow), Alptal (green), Borden (red), Cherskiy (dark blue), Seehornwald (maroon), Sodankylä (light blue), and Yakutsk (violet). Note that SAI fractions are shown for both PFTs of the mixed forest at Borden, deciduous broadleaf trees (solid) and evergreen needleleaf trees (dashed).

over multiple hours in contrast to air temperature and was close to longwave radiation emitted from a blackbody at $0°\mathrm{C}$, and these suspicious time steps were then checked for previous or simultaneous precipitation events. Subsequently, in cases of snow cover on radiometers full days including these time steps were removed from evaluation.

Studies give different values of leaf area index (LAI) for Alptal, mean stand LAI of 3.9 $\mathrm{m^2 m^{-2}}$ (*Gouttevin et al.*, 2015) and total LAI of 4.2 $\mathrm{m^2 m^{-2}}$ (*Rutter et al.*, 2009) while *Stähli et al.* (2009) give a range of 3.9 $\mathrm{m^2 m^{-2}}$ to 4.5 $\mathrm{m^2 m^{-2}}$ for LAI along the rail based on hemispherical photography. Total LAI includes woody parts and thus represents plant area index (PAI), indicating LAI values given by *Stähli et al.* (2009) and *Gouttevin et al.* (2015) also represent PAI. Consequently, an average of 4.1 $\mathrm{m^2 m^{-2}}$ along the rail was used as PAI based on the profile given by *Stähli et al.* (2009). Values for LAI and stem area index (SAI) are necessary for calculations by CLM4.5 and were estimated using their respective fractions of PAI (Figure 4.2), which were taken from Alptal's corresponding grid cell and PFT in the high-resolution surface dataset of CLM4.5 and averaged over the months of evaluation periods.

Meteorological forcing data had been measured either above the forest canopy, where instruments had been installed on a tower of $35\mathrm{m}$ height, or in an open meadow $200\mathrm{m}$

from the forest (Table 4.2). Fraction of diffuse shortwave radiation was approximated by projecting changes in ε_{sky} (see Equation (2.4)) onto a scale of 0 to 1, representing changes in cloudiness. The precipitation partitioning algorithm given by *Rutter et al.* (2009) for Alptal was used to estimate rainfall and snowfall. Manual snow depth measurements had been taken on a weekly basis throughout the snow season and were extrapolated to create a continuous time series. Ground albedo measurements were used to set snow cover fraction to either 1 or 0. Snow cover fraction was set to 0.5 for snow depths smaller than $15\mathrm{cm}$, which coincided with measurements of outgoing longwave radiation indicating surface temperatures larger than $0°\mathrm{C}$ but ground albedo indicating snow cover. Soil temperature had been measured at a depth of $20\mathrm{cm}$. Soil water content was approximated using observations of ground water level for Alptal. Ground water level was expressed as a fraction of its range over the 4-year period, averaged, and multiplied with soil water capacity. Soil albedo was taken from *Rutter et al.* (2009).

Seehornwald, Switzerland Descriptions of the forest stand near Davos, Switzerland are given by *Webster et al.* (2016b) and *Zweifel et al.* (2016). LAI was taken from *Webster et al.* (2016b) and SAI was calculated as for Alptal using the value from Seehornwald's corresponding grid cell and PFT (Figure 4.2). Stand basal area was calculated from tree diameter and tree density given online by the Swiss Long-Term Forest Ecosystem Research (LWF) programme. Sub-canopy longwave and shortwave radiation had been measured by the rail setup described for Alptal, which was moved to Seehornwald in 2007.

The Swiss National Air Pollution Monitoring Network (NABEL) operates a measurement tower at this site and data are available via FluxNet (labelled Davos). Fraction of diffuse shortwave radiation was estimated as a ratio of measured insolation to potential insolation taken from the FluxNet database. Rainfall and snowfall were estimated using the precipitation partitioning algorithm for Alptal. Continuous measurements of snow depth were only available from an open site less than 1km away from the forest. Manual snow depth measurements in the forest were used to calculate a ratio of forest to open

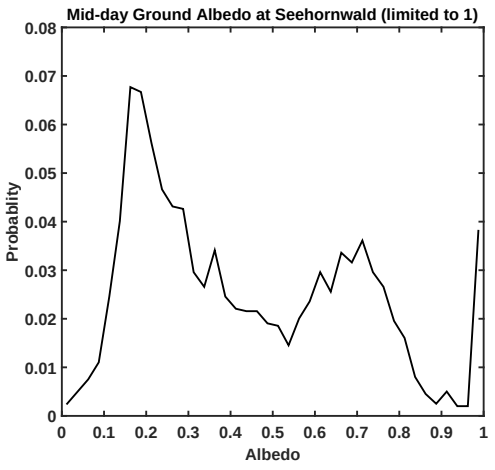

Figure 4.3: Probability density function (PDF) of mid-day ground albedo at Seehornwald measured from October 2007 to March 2013

snow depth and subsequently to scale continuous open site measurements. Based on ground albedo measurements, snow cover fraction was assumed to be 1 for snow depths higher than 25cm, 0 for snow depths of 0cm, and 0.5 for snow depths in between. Soil albedo was estimated from ground albedo measurements over the entire period the rail setup had been deployed, a probability density function (PDF) of which shows two distinct peaks, one for snow cover and one for soil albedo (Figure 4.3).

Sodankylä, Finland Descriptions of the forest stand are given by *Hancock et al.* (2014) and *Reid et al.* (2014a), where it is listed as site C out of multiple sites at Sodankylä. Sub-canopy longwave radiation had been measured by 4 radiometers providing a spatial average for this study. Radiometers had been checked and quality-controlled on a daily basis. PAI had been estimated from hemispheric photos for each radiometer location ranging from 1.09 $\mathrm{m^2 m^{-2}}$ to 1.22 $\mathrm{m^2 m^{-2}}$ and averaging 1.14 $\mathrm{m^2 m^{-2}}$. LAI and SAI were estimated as for Alptal using the value from Sodankylä's corresponding grid cell and PFT (Figure 4.2).
Meteorological forcing data had been measured near the forest stand, either in an open area or atop a tower of 48m height (Table 4.2). Vertical profiles of soil temperature and soil moisture had been measured in an intensive observation area near the forest stand. A threshold temperature of 2°C was used for partitioning of precipitation into snowfall and rainfall following *Essery et al.* (2016). Snow depth was adjusted to sub-canopy values by applying a scaling factor of 0.75, based on *Essery et al.* (2016, Figure 6). Sub-canopy air temperature measurements taken at 50cm height were used as a proxy for surface temperature and limited to a maximum of 0°C due to consistent snow cover. Fraction of tree height occupied by trunks, which is used to enable direct insolation to tree trunks in SNOWPACK, was changed from its Alptal value of 0.2 to 0.5 based on photos of the Sodankylä measurement location.
In addition to sub-canopy downward radiation, tree trunk temperatures had been measured via one infrared thermocouple and 64 contact thermocouples, which had been stuck underneath the tree bark. Contact thermocouples had been distributed among two pine trees, a "small" one and one of "medium" height, at different heights and cardinal directions. Measurements by unreliably working contact thermocouples and for unbalanced cardinal directions (e.g. South without North or East without West) were dismissed, which left the following sets of contact thermocouples: contact thermocouples at the medium-height tree directed toward North, East, South, and West at heights of 5cm, 10 cm, 25cm, and 50cm as well as directed toward North and South at heights of 100cm and 150cm; contact thermocouples at the small tree directed toward North and South at heights of 5cm, 10cm, and 25cm. Measurements by these contact thermocouples were averaged for comparison

with simulated vegetation temperatures.

Cherskiy, Russia Description of the forest stand near Cherskiy, Russia is given by *Alexander et al.* (2012), where it is listed as stand 13. The forest stand differs in vegetation structure compared to previous sites, as trees are smaller and thinner (Table 4.1) but tree density is high (3.7 trees m^{-2}). A canopy top height of $5\mathrm{m}$ was used instead of mean stand height of $3.4\mathrm{m}$ given by *Alexander et al.* (2012). LAI was set to 0 as vegetation was leafless throughout the evaluation period. SAI was estimated as the lateral surface area of conical trees based on tree height and tree diameter. Single radiometers had measured upward and downward shortwave and longwave radiation in a fixed position beneath the canopy. Radiation measurements were quality-controlled for snow cover on radiometers as described for Alptal.

Incoming shortwave and longwave radiation, air temperature, and relative humidity had been measured $2\mathrm{m}$ above the canopy. Wind speed and precipitation had been measured with a temporal resolution of 3 hours at the airport of Cherskiy, about 7km from the forest site. Precipitation was distributed evenly over each measurement interval and wind speed was assumed as constant for each measurement interval to create hourly values. Rainfall and snowfall were partitioned as for Sodankylä. Fraction of diffuse incoming shortwave radiation was approximated as for Alptal. In lieu of measurements, snow depth was set to a constant value ($0.2\mathrm{m}$) higher than roughness length thresholds for CLM4.5 and SNOWPACK. Soil water content was calculated from volumetric water content measurements at two depths ($20\mathrm{cm}$ and $50\mathrm{cm}$). Fraction of frozen soil was calculated from temperature measurements at two depths within the mineral soil ($20\mathrm{cm}$ and $50\mathrm{cm}$) as well as temperature measurements at the organic interface (at $10\mathrm{cm}$ depth). Soil albedo was estimated from ground albedo measurements over the entire available period, and fresh snow albedo for the snow ageing parameterization was set to 0.45 based on ground albedo measurements (Figure 4.4).

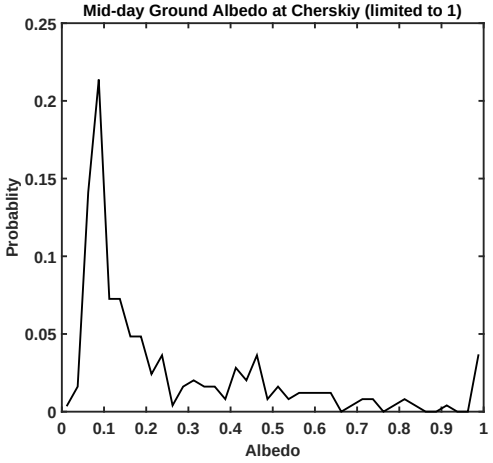

Figure 4.4: PDF of mid-day ground albedo at Cherskiy measured from July to October 2016 and from April to July 2017

Abisko, Sweden Descriptions of the forest stand are given by *Reid et al.* (2014a,b), where it is listed as site C out of multiple sites at Abisko. Sub-canopy longwave radiation had been measured by 4 radiometers, providing a spatial average for this study, and quality controlled by *Reid et al.* (2014a). PAI had been estimated from hemispheric photos for each radiometer location ranging from 0.14 $\mathrm{m^2 m^{-2}}$ to 0.70 $\mathrm{m^2 m^{-2}}$ and averaging 0.44 $\mathrm{m^2 m^{-2}}$. LAI was set to 0 and SAI set to PAI as the forest consists of birch trees that were leafless throughout the evaluation period.
Meteorological forcing data and soil temperature had been measured by a weather station on ground level in an open area near the forest stand. Precipitation had been measured daily and was distributed evenly over 24 hours. Rainfall and snowfall were partitioned as for Sodankylä. Snow depth had been measured manually on a daily basis in the open area, was assumed to be constant over a day, and was not scaled for the forest stand due to sparse, leafless vegetation. Surface temperature was approximated as for Sodankylä. Measurements of soil water content were not available and approximated from two separate ground water level measurements available online from the Geological Survey of Sweden. The proxy was calculated as a fraction of historical range of ground water level.

Yakutsk, Russia Description of the forest stand north of Yakutsk, Russia is given by *Ohta et al.* (2001) stating trees had still been leafless after snowmelt with an SAI of 1.71, so that LAI was set to 0. Mean tree diameter was estimated corresponding to mean stand height based on diameters and heights for four trees used for sap flow measurements (*Ohta et al.*, 2001).
Incoming and outgoing shortwave radiation, net all-wave radiation, and surface temperatures had been measured beneath the canopy, and sub-canopy longwave radiation was calculated as a residual. However, incoming shortwave radiation beneath the canopy displayed large fluctuations compared to outgoing shortwave radiation resulting in occasional negative net shortwave radiation, which had potentially been caused by the usage of a single radiometer. Consequently, only nighttime sub-canopy longwave radiation was used for this study.
Meteorological forcing data had been measured at a height of about $30\mathrm{m}$ on an instrumented tower. Vertical profiles of soil temperature and soil moisture had been measured at the tower location. Fraction of diffuse incoming shortwave radiation was approximated as for Alptal. Daily measurements of precipitation in the city of Yakutsk were taken from the Carbon Dioxide Information Analysis Center (CDIAC) database and distributed evenly over 24 hours. In lieu of measurements, snow depth was set to a constant value ($0.2\mathrm{m}$) higher than roughness length thresholds for CLM4.5 and SNOWPACK. Soil albedo was estimated based on sub-canopy shortwave radiation measurements. Gaps in

forcing data of 4 hours or less were interpolated linearly and a gap of 24 hours was excluded from evaluation.

Borden, Canada Description of the forest stand is given by *Teklemariam et al.* (2009) and *Froelich et al.* (2015). The forest stand consists of deciduous broadleaf and evergreen needleleaf trees, so that two PFTs were used for CLM4.5 simulations. Fractions of PFTs were based on the most recent tree survey described by *Teklemariam et al.* (2009), yielding 18.7% for evergreen needleeleaf trees and 81.3% for deciduous broadleaf trees, and used to weigh sub-canopy longwave radiation calculated separately for each PFT. Temperate instead of boreal PFTs were used as the Borden forest is located in the southern part of the North American deciduous-boreal forest ecotone. Tree diameter and stand basal area for each PFT were estimated based on tree diameters given by *Neumann et al.* (1989) and the tree survey described by *Teklemariam et al.* (2009). Post-leaf out LAI for the forest stand is given as 4.6 $\mathrm{m^2 m^{-2}}$ by *Croft et al.* (2015). Pre-leaf out and post-leaf out stand PAI had been measured as 1.36 $\mathrm{m^2 m^{-2}}$ and 5.6 $\mathrm{m^2 m^{-2}}$, respectively, by Paul Bartlett (private communication). LAI and PAI measurements, LAI-to-SAI fractions from CLM4.5's high-resolution surface dataset for corresponding PFTs and grid cell (Figure 4.2), and PFT fractions were used to calculate LAI and SAI values for both PFTs. Sub-canopy radiation measurements were quality-controlled for snow cover on radiometers.
Meteorological forcing data had been measured either at a height of $33\mathrm{m}$ ($44\mathrm{m}$ for wind speed) on an instrumented tower or in an open area near the forest stand (Table 4.2). Vertical profiles of soil temperature and soil moisture had been measured at the tower location. Description of the instrumentation is given by *Froelich et al.* (2015). Rainfall and snowfall were partitioned as for Sodankylä. In lieu of measurements, snow depth was set to a constant value ($0.2\mathrm{m}$) higher than roughness length thresholds for CLM4.5. Soil albedo was estimated based on sub-canopy shortwave radiation measurements. LAI for BDTTs was set to 0.05 $\mathrm{m^2 m^{-2}}$ instead of 0 to allow for latent heat fluxes. Gaps in forcing data of 4 hours or less, and two gaps of 6 and 8 hours for wind speed, were linearly interpolated and a gap of 10 hours in all forcing variables was excluded from evaluation.

Table 4.1: Characteristics of forest stand sites. Evaluation days differ from the length of evaluation periods due to quality control of measurements. Acronyms denote PFTs mentioned in Chapter 2.2.1. Soil albedo was not determined for Abisko and Sodankylä due to constant snow cover. Fractions of soil composition were taken from CLM4.5's $0.23^\circ \times 0.31^\circ$ surface dataset and averaged vertically. *Evaluation periods at Alptal start on 1 January except for 2004 (24 January) and end on 12 March 2004, 14 March 2005, 19 March 2006, and 4 April 2007. Evaluation durations for Alptal are 41 days in 2004, 57 days in 2005, 73 days in 2006, and 85 days in 2007. **Dates for end of evaluation period at Seehornwald are: 27 April 2008, 1 April 2009, 20 April 2010, 29 March 2011, 26 April 2012. Evaluation durations for Seehornwald are 116 days in 2008, 90 days in 2009, 106 days in 2010, 83 days in 2011, and 116 days in 2012.

	Abisko	**Alptal**	**Borden**	**Cherskiy**	**Seehornwald**	**Sodankylä**	**Yakutsk**
Latitude	68.4°N	47.1°N	44.3°N	68.7°N	46.8°N	67.4°N	62.3°N
Longitude	18.8°E	8.8°E	79.9°W	161.4°E	9.9°E	26.6°E	129.6°E
Altitude	388m	1220m	222m	39m	1640m	179m	220m
Snowmelt season	2011	2004-07	2013	2017	2008-12	2012	1998
Evaluation start	11 Mar	*	2 Jan	30 Mar	1 Jan	10 Mar	14 Feb
Evaluation end	3 Apr	*	4 Apr	21 May	**	16 Apr	14 May
Evaluation days	9	*	77	51	**	37	87
Vegetation	birch	spruce	mixed	larch	spruce	pine	larch
PFT	BDBT	NEBT	BDTT, NETT	NDBT	NEBT	NEBT	NDBT
Tree Height	3.5m	25m	22m	5m	25m	18m	18m
Tree Diameter	3.8cm	100cm	6.8cm, 12.3cm	1.7cm	40cm	11.6cm	25.6cm
Stand Basal Area [m^2m^{-2}]	0.0006	0.004	0.0011, 0.0036	0.0048	0.0166	0.002	0.004
SAI [m^2m^{-2}]	0.44	0.86	1.10, 0.48	0.67	1.2	0.25	1.71
LAI [m^2m^{-2}]	0	3.24	0.05, 1.93	0	3.9	0.89	0
PAI [m^2m^{-2}]	0.44	4.1	1.15, 2.41	0.67	5.1	1.14	1.71
Soil Albedo	-	0.11	0.20	0.09	0.19	-	0.19
Clay	19%	24%	3%	19%	31%	12%	26%
Sand	54%	48%	71%	46%	52%	61%	41%
Organic Matter	7%	7%	6%	12%	8%	25%	9%

Table 4.2: Measurement locations, measurement methods, and approximations of forcing variables. Symbols as used in Figure 4.1. ε_{sky} indicates effective emissivity of the sky (Equation (2.4)) was used to approximate fraction of diffuse shortwave radiation f_{diff}. GWL indicates ground water level was used to approximate soil water content. LWR indicates outgoing longwave radiation was used to estimate surface temperature. Soil temperature T_{soil} was used to estimate fraction of frozen soil. Calculation of rainfall fraction $f_{rainfall}$ out of precipitation was based on either a transition algorithm over the range of 0-1.5°C, given by *Rutter et al.* (2009) for Alptal, Switzerland, or a threshold algorithm at 2°C, given by *Essery et al.* (2016) for Sodankylä, Finland.

Forcing	**Abisko**	**Alptal**	**Borden**	**Cherskiy**	**Seehornwald**	**Sodankylä**	**Yakutsk**
LW_{atm}	open	tower	tower	tower	tower	open	tower
P	open	open	open	open	tower	open	open
RH	open	open	tower	tower	tower	tower	tower
SW_{in}	open	tower	tower	tower	tower	open	tower
T_{air}	open	tower	tower	tower	tower	tower	tower
u	open	tower	tower	open	tower	tower	tower
z_{snow}	open	forest, manual	assumption	assumption	open, scaled	open, scaled	assumption
LW_{sub}	4 radiometers	rail	single radiometer	single radiometer	rail	4 radiometers	residual
SWC	proxy (GWL)	proxy (GWL)	vertical profile	vertical profile	single depth	vertical profile	vertical profile
T_{soil}	vertical profile	single depth	vertical profile	vertical profile	single depth	vertical profile	vertical profile
f_{diff}	measured	ε_{sky}	ε_{sky}	ε_{sky}	potential SW_{in}	measured	ε_{sky}
f_{snow}	constant	α_{gr}	α_{gr}	α_{gr}	α_{gr}	constant	top T_{soil}
$f_{rainfall}$	threshold	transition	threshold	threshold	transition	threshold	threshold
T_{surf}	T_{air} (0.5m)	LWR	LWR	LWR	LWR	T_{air} (0.5m)	measured

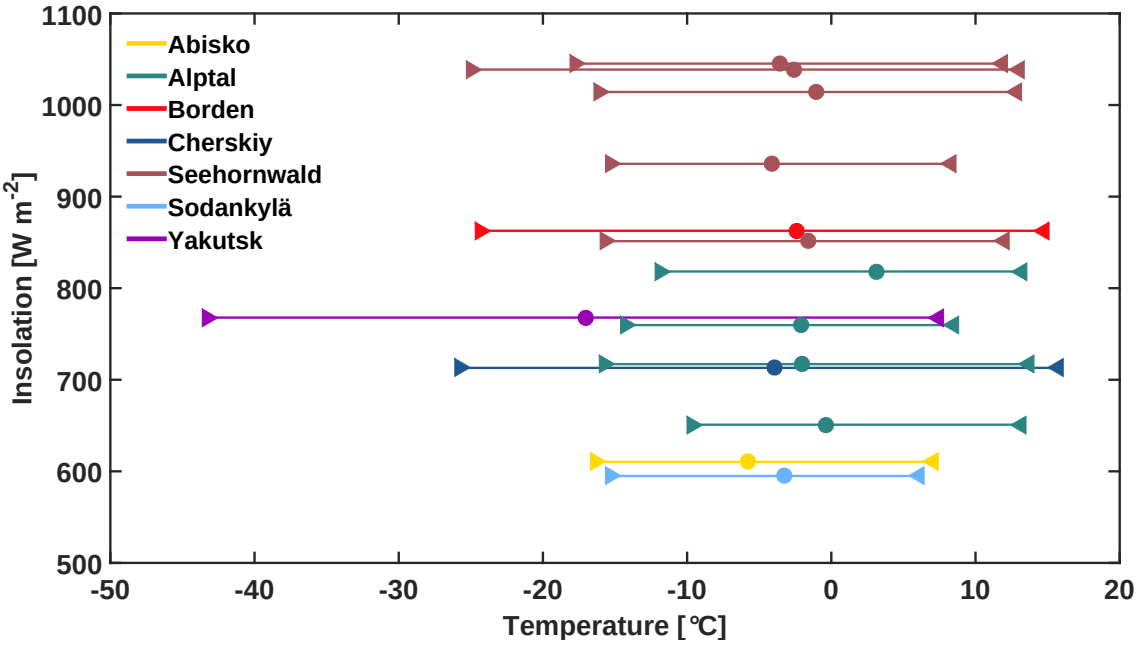

Figure 4.5: Comparison of air temperature (minimum, mean, maximum) and maximum insolation over respective evaluation periods (see Table 4.1) for forest stand sites Abisko (yellow), Alptal (green, individual years), Borden (red), Cherskiy (dark blue), Seehornwald (maroon, individual years), Sodankylä (light blue), and Yakutsk (violet). Maximum insolation at Yakutsk is shown only for context, as evaluation was limited to nighttime.

4.3 Site comparison

This study uses data from seven forest stands, of which three consist of evergreen needle-leaf trees, three consist of deciduous trees, and one is a mixed forest of both evergreen and deciduous trees. The forest stands used for evaluation represent all three boreal PFTs of CLM4.5 (Figure 2.1), although vegetation characteristics are not the same (compare Tables 2.1 and 4.1). The current version of SNOWPACK is only suited for evergreen sites as it was developed for alpine forests (*Gouttevin et al.*, 2015), so that its usage was limited to Alptal, Seehornwald, and Sodankylä. The start of evaluation periods was determined by data availability at each site except for Alptal (2005-2007) and Seehornwald, for which evaluation start was set to 1 January. The end of evaluation periods was determined by data availability for Abisko and Sodankylä. For Alptal, Borden, Cherskiy, Seehornwald, and Yakutsk, the end of evaluation periods was determined by meltout, which was estimated from ground albedo measurements.

Air temperatures are similar across most sites (Figure 4.5), the exception being Yakutsk for which evaluation started four to six weeks earlier than for the other high-latitude sites Abisko, Cherskiy, and Sodankylä. Maximum insolation varies across sites; Borden and

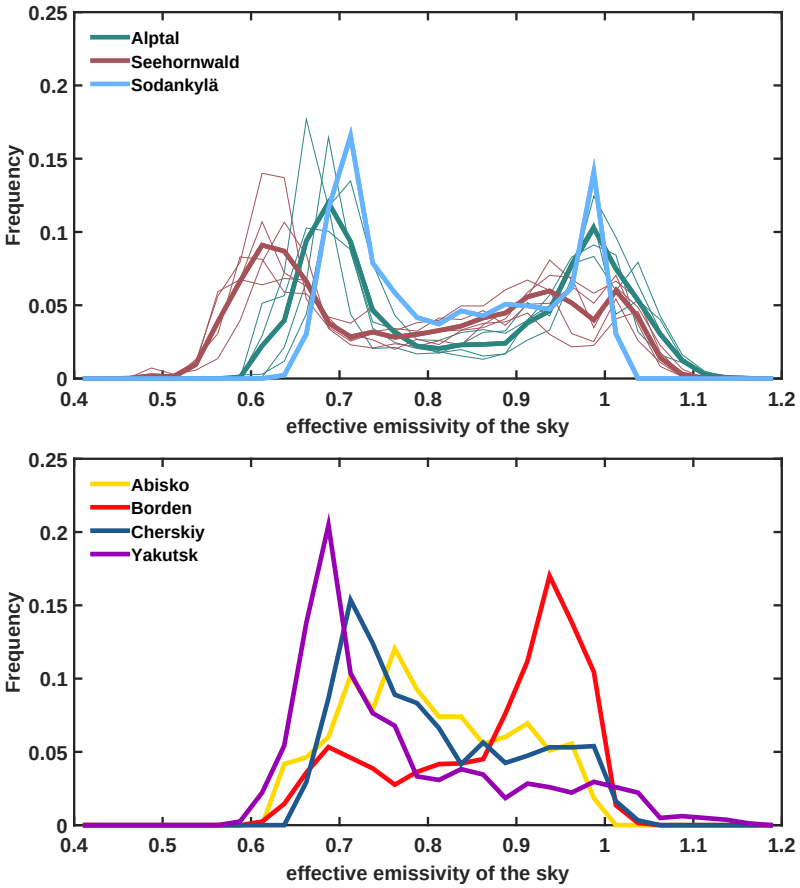

Figure 4.6: PDFs of effective emissivities of the sky over respective evaluation periods (see Table 4.1) for evergreen (top) and deciduous (bottom) Toy Model sites Abisko (yellow), Alptal (green), Borden (red), Cherskiy (dark blue), Seehornwald (maroon), Sodankylä (light blue), and Yakutsk (violet). Multiple lines for Alptal and Seehornwald display total (bold line) and individual years (thin lines).

Seehornwald display larger insolation maxima due to latitude and duration of evaluation period. Effective emissivity of the sky (ε_{sky}), which is described in Chapter 2.1, varies greatly based on cloudiness and hence was used to categorize meteorological conditions. For clear skies, radiative temperature of the atmosphere decreases reducing the amount of atmospheric longwave radiation reaching vegetation and ground. Conversely, radiative temperature for overcast conditions is similar to or higher than actual air temperature resulting in ε_{sky} close to or larger than 1. Effective emissivity of the sky is a dimensionless quantity and thus suitable to compare different locations, and PDFs of ε_{sky} are shown in Figure 4.6. Abisko, Cherskiy, and Yakutsk exhibit one clear peak at low emissivity values indicating mostly clear-sky conditions, while there is one peak at high emissivity values for Borden indicating mostly overcast conditions. Alptal, Sodankylä, and, to a lesser degree, Seehornwald exhibit two peaks, one at each end of the spectrum, indicating

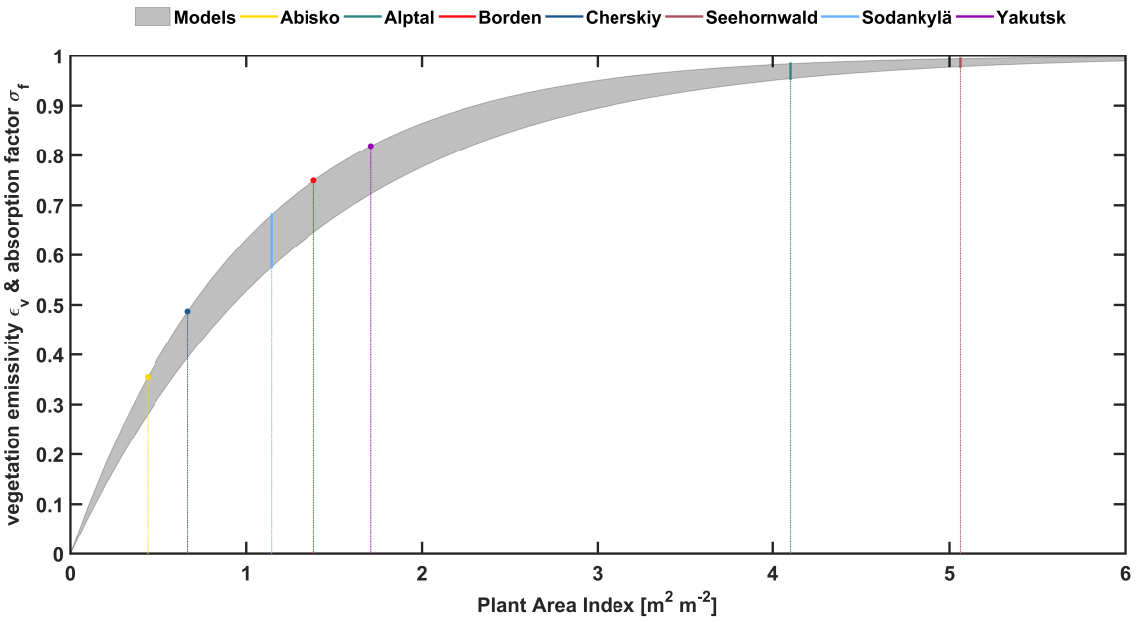

Figure 4.7: Vegetation emissivity ε_v (Equation (2.5)) and absorption factor σ_f (Equation (2.10)) as functions of vegetation density for model calculations (grey shading, upper boundary ε_v, lower boundary σ_f) and forest stands at Abisko (yellow), Alptal (green), Borden (red), Cherskiy (dark blue), Seehornwald (maroon), Sodankylä (light blue), and Yakutsk (violet). Note that SNOWPACK is limited to evergreen needleleaf trees, so that differences between ε_v and σ_f are only shown for Alptal, Seehornwald, and Sodankylä.

varying degrees of cloudiness.

Parameters for absorption and emission of longwave radiation calculated by CLM4.5 (Equation (2.5)) and SNOWPACK (Equations (2.10) to (2.12)) are shown for each forest stand in Figure 4.7, in order to illustrate representations of vegetation density. Both vegetation emissivity ε_v in CLM4.5 and absorption factor σ_f in SNOWPACK are calculated from PAI and based on Beer's law, thus using an exponentail profile $e^{-(k\ PAI)}$. Extinction coefficient k differs between CLM4.5 and SNOWPACK with CLM4.5 featuring a value of 1 and SNOWPACK featuring a value of 0.75, which was calibrated by *Gouttevin et al.* (2015) for the dense forest at Alptal, Switzerland, and consequently ε_v is higher than σ_f for the same PAI. Usage of SNOWPACK was limited to evergreen forest stands and differences between ε_v and σ_f are small for the dense forests at Alptal and Seehornwald, however, there is a substantial difference for the forest stand at Sodankylä. Based on vegetation density and ε_v, forest stands used in this study form three groups. Deciduous sites Abisko and Cherskiy feature sparsest vegetation, due to small tree heights, and consequently lowest ε_v, although slightly higher vegetation density for Cherskiy already results in a substantial difference in ε_v due to the exponential profile. While vegetation types

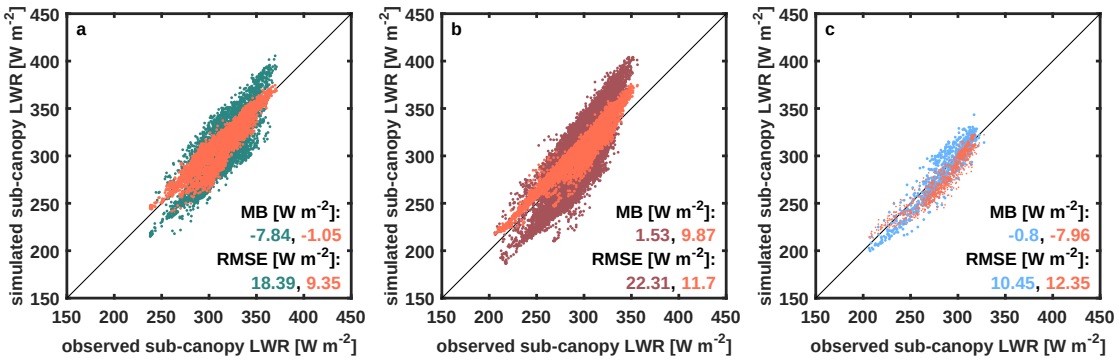

Figure 4.8: Comparison of observed and simulated sub-canopy longwave radiation for Alptal (**a**), Seehornwald (**b**), and Sodankylä (**c**). SNOWPACK simulations are shown in orange, whilst CLM4.5 simulations are shown in green (Alptal), maroon (Seehownwald), and light blue (Sodanklya). Mean bias (MB) and root-mean-square error (RMSE) values are given in Table 4.3 for comparison with deciduous forest stands.

differ between the forest stands at Borden, Sodankylä, and Yakutsk, vegetation densities are similar and lead to similar values of ε_v. Dense, evergreen forests at Alptal and Seehornwald display the highest values of ε_v with minimal difference between them despite substantial differences in vegetation density, which is due to the exponential profile.

4.4 Comparison of sub-canopy longwave radiation simulated by CLM4.5 and SNOWPACK with observations

Simulated and observed sub-canopy longwave radiation for evergreen sites are compared in Figure 4.8. Ranges of observations and simulations differ between sites as a consequence of differences in vegetation density (Table 4.1) and meteorological forcing (Figure 4.5). Simulations by CLM4.5 display a larger spread than simulations by SNOWPACK for both Alptal and Seehornwald, resulting in root-mean-square error (RMSE) values about twice as high as for SNOWPACK. For Sodankylä, spread in sub-canopy longwave radiation simulated by CLM4.5 is smaller than for Alptal and Seehornwald, with RMSE being smaller by about 50%, and similar to the spread simulated by SNOWPACK. Simulations by CLM4.5 exhibit a substantial negative mean bias (MB) for Alptal, in contrast to simulations by SNOWPACK, while MB values are close to zero for Seehornwald and Sodankylä. For SNOWPACK, MB is close to zero for Alptal but substantially larger in absolute terms for Seehornwald and Sodankylä. RMSE values are also higher for Seehornwald and Sodankylä compared to Alptal, for which SNOWPACK was calibrated; however, the spread in sub-canopy longwave radiation simulated by SNOWPACK is similar for all evergreen sites.

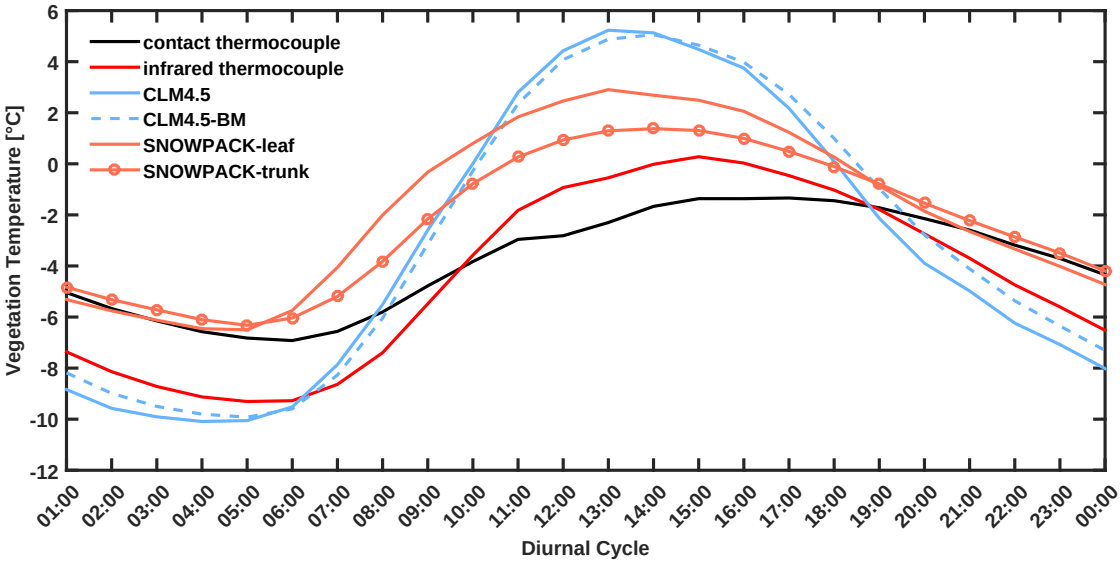

Figure 4.9: Diurnal cycle of vegetation temperature at Sodankylä for site-averaged contact thermocouple observations (black), infrared thermocouple observations (red), SNOWPACK leaf layer (orange), SNOWPACK trunk layer (orange with circles), and CLM4.5 (light blue) before (solid) and after (dashed) implementation of biomass heat storage.

Similarly large magnitudes of RMSE and MB indicate that SNOWPACK almost consistently overestimates or underestimates sub-canopy longwave radiation for forest stands at Seehornwald and Sodankylä, which coincides with differences in vegetation density compared to Alptal, for which SNOWPACK was calibrated. Comparison of vegetation temperatures reveals a smaller diurnal cycle for SNOWPACK compared to CLM4.5 (Figure 4.9), with lower vegetation temperatures during day and higher vegetation temperatures at night. This indicates consistent underestimation of sub-canopy longwave radiation at Sodankylä by SNOWPACK is due to an underestimation of absorption and emission parameter σ_f and consequently too little contribution to sub-canopy longwave radiation from vegetation, rather than too little longwave radiation emitted from vegetation. Temperature of the trunk layer in SNOWPACK displays a smaller diurnal cycle as well as later maximum and minimum than SNOWPACK's leaf layer, which highlights sheltering by the upper layer and more substantial thermal inertia due to more biomass. Implementation of SNOWPACK's parameterization for biomass heat storage in CLM4.5 does not reduce the diurnal range of vegetation temperature but slightly delays its diurnal cycle. Comparison with observations shows that vegetation temperatures simulated by SNOWAPCK agree with those measured underneath the tree bark at night but are higher during daytime. Vegetation temperature measured by the single infrared thermocouple displays a higher diurnal range, with higher daytime and lower nighttime values, a lower average, and an earlier diurnal maximum compared to contact thermocouple measure-

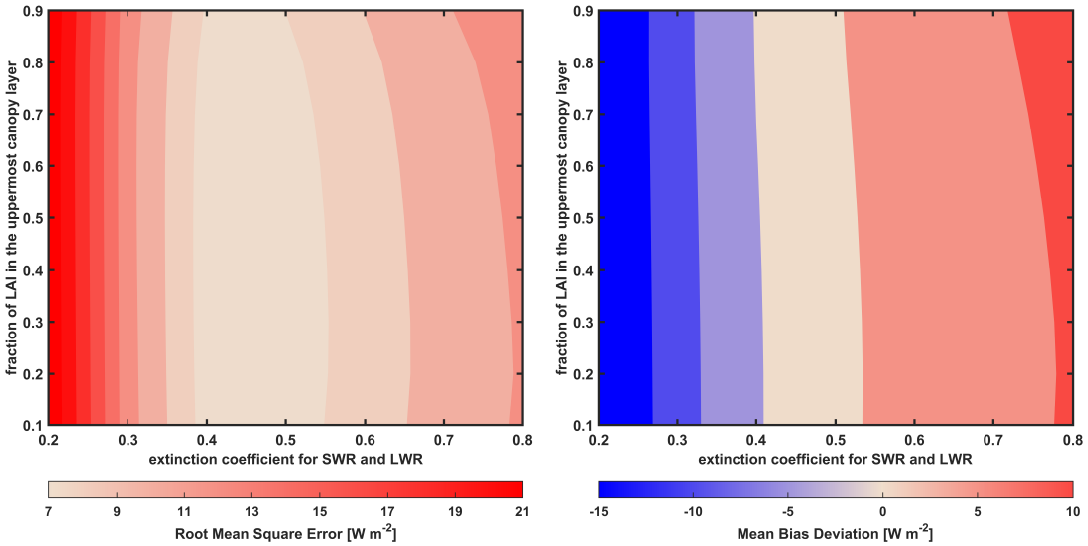

Figure 4.10: Changes in RMSE (left panel) and MB (right panel) for sub-canopy longwave radiation simulated by SNOWPACK due to variations in parameters f_{LAI} and k_{LAI} for study site Seehornwald, Switzerland.

ments, as it represents a surface temperature. Nighttime vegetation temperature simulated by CLM4.5 is only slightly lower than that measured by the infrared thermocouple, but CLM4.5 simulates a substantially higher daytime vegetation temperature. However, vegetation temperatures were only measured for tree stems, not for foliage, and at rather low heights. Since vegetation at Sodankylä is evergreen, measurements do not yield ideal temperatures for comparison with CLM4.5.

Sub-canopy longwave radiation simulated by SNOWPACK exhibits low RMSE and a MB close to 0 for Alptal. However, RMSE values are higher for both Seehornwald and Sodankylä. Mean bias is substantially positive for Seehornwald, which features a higher vegetation density compared to Alptal, and substantially negative for Sodankylä, which features a lower vegetation density compared to Alptal. As parameters f_{LAI}, representing the fraction of LAI in the uppermost canopy layer, and k_{LAI}, representing an extinction coefficient for SW and LW radiation, were calibrated by *Gouttevin et al.* (2015) for Alptal, sensitivity of RMSE and MB values to changes in f_{LAI} and k_{LAI} was tested for Seehornwald and Sodankylä (Figures 4.10 and 4.11). Generally, k_{LAI} displays a higher impact on metrics than f_{LAI}. Smallest RMSE and MB values for Seehornwald are found for f_{LAI} between 0.2 and 0.3 and k_{LAI} between 0.45 and 0.5, both of which are lower than values calibrated at Alptal (f_{LAI} of 0.5 and k_{LAI} of 0.75). Parameters can be calibrated for MB to reach 0. For Sodankylä, RMSE and in absolute terms MB values are smallest for highest possible values of f_{LAI} and k_{LAI} (both close to 1). In contrast to Seehornwald, a MB of 0 cannot be reached via calibration indicating SNOWPACK inherently underestimates sub-

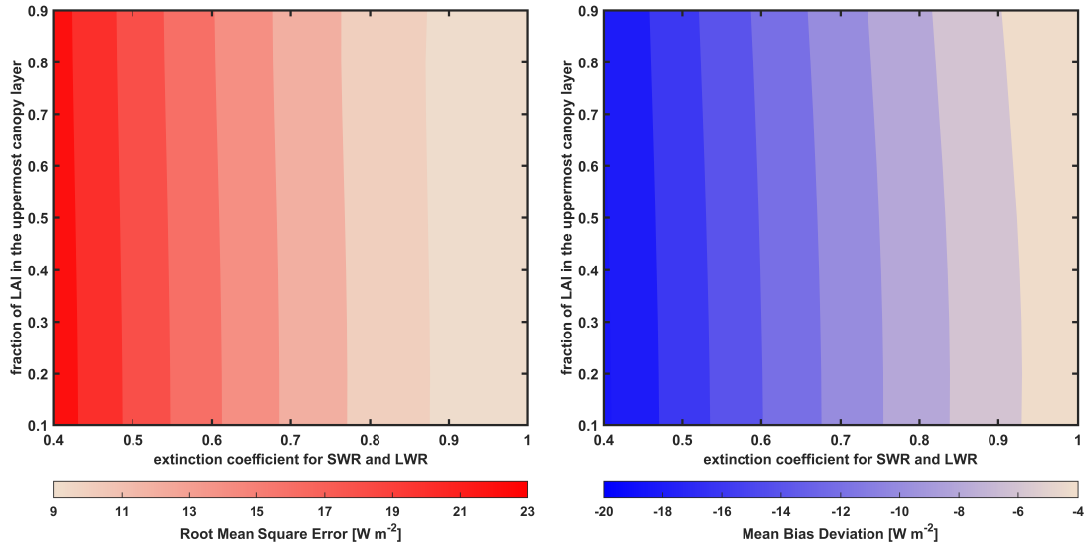

Figure 4.11: Changes in RMSE (left panel) and MB (right panel) for sub-canopy longwave radiation simulated by SNOWPACK due to variations in parameters f_{LAI} and k_{LAI} for study site Sodankylä, Finland.

canopy longwave radiation for Sodankylä. This might be due to low vegetation density and sparse canopies in particular that result in insolation reaching stems, which cannot be represented by SNOWPACK for this forest stand. Even though SNOWPACK allows for direct shortwave radiation reaching the trunk layer, this parameterization uses tree height without considering vegetation density or basal area.

Calibration of extinction coefficient for radiation reflects differences in vegetation density for Seehornwald and Sodankylä compared to Alptal. Higher vegetation density at Seehornwald necessitates a decreased extinction coefficient while lower vegetation density at Sodankylä necessitates a higher extinction coefficient. Note that *Gouttevin et al.* (2015) prescribed a range of 0.4 to 0.8 for k_{LAI} but calibration yielded a value of 1 for Sodankylä, which is also used in CLM4.5. Parameter f_{LAI} is only slightly different at Seehornwald compared to Alptal, potentially due to the same tree types and thus same structure at both sites, but considerably higher at Sodankylä compared to Alptal, which might reflect differences in vegetation type and structure (pine compared to fir and spruce). Generally, both RMSE and MB can be improved for SNOWPACK via calibration, mainly by increasing (decreasing) extinction coefficient k_{LAI} for lower (higher) vegetation density.

4.5 Simulation of longwave enhancement by CLM4.5

Relative errors of sub-canopy longwave radiation simulated by CLM4.5 are shown in Figure 4.12. Evergreen sites and Cherskiy display the same triangular pattern; errors increase in absolute terms for lower values of ε_{sky} with daytime overestimation and nighttime underestimation. The range of errors is higher for Alptal than for Sodankylä and Cherskiy when comparing the range of ε_{sky} and insolation present at Sodankylä and Cherskiy. Simulations for Seehornwald display a higher range of errors than for Alptal when comparing similar meteorological conditions and larger maximum overestimation due to later meltout leading to higher maximum insolation. For ε_{sky} reaching values larger than 1, which occurs regularly for Alptal and Seehornwald in contrast to Sodankylä and Cherskiy, nighttime underestimation increases in absolute terms for higher ε_{sky}. For Abisko, relative errors decrease slightly for clearer skies during nighttime, resembling the pattern seen for previous sites, but there is no clear pattern in daytime errors. Relative errors for nighttime at Yakutsk contrast those for previous sites, with spread around 0 increasing for clearer skies. For Borden, the range of errors is similar to Alptal although maximum insolation is higher. In addition, there are nighttime simulation errors close to 0 for the whole range of ε_{sky} and occasional daytime underestimations. RMSE values in Table 4.3 display a contrast between dense vegetation at Alptal and Seehornwald (18 Wm^{-2} and 22 Wm^{-2}, respectively), low-to-medium density vegetation with values between 10 Wm^{-2} and 12 Wm^{-2} (Borden, Cherskiy, Sodankylä), and sparse vegetation at Abisko (6 Wm^{-2}).
Patterns seen for sub-canopy longwave radiation translate to longwave enhancement displaying nighttime underestimation and daytime overestimation (Figure 4.13). Both longwave enhancement and ε_{sky} depend on atmospheric longwave radiation. For clear skies, atmospheric longwave radiation decreases resulting in decreasing ε_{sky} and increasing longwave enhancement during both day and night, while insolation is higher during clear-sky days increasing vegetation temperatures. Therefore, increasing absolute errors of sub-canopy longwave radiation for clearer skies result in increasing absolute errors for higher longwave enhancement. Alptal, Seehornwald, Sodankylä, Cherskiy, and Borden display this pattern, however, neither Abisko nor Yakutsk do. Ranges of longwave enhancement differ substantially between sites. At Seehornwald, longwave enhancement values of more than 1.9 and less than 0.9 have been observed. At Alptal, Borden, and Yakutsk, longwave enhancement values of up to 1.6 have been observed. Ranges of observed longwave enhancement values are smaller and similar for Cherskiy and Sodankylä and distinctly smaller for Abisko.

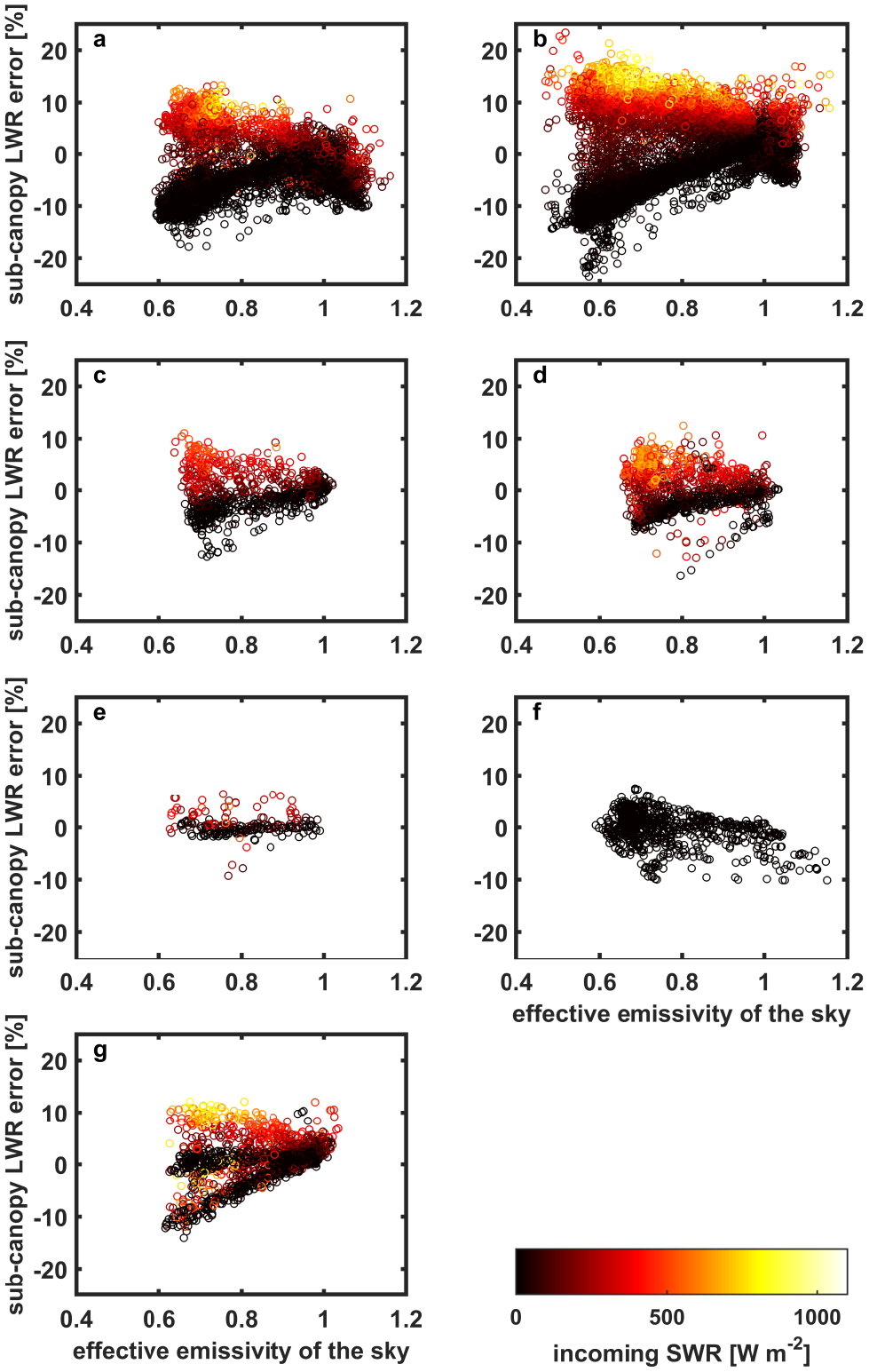

Figure 4.12: Sub-canopy longwave radiation errors simulated by CLM4.5 relative to observations as a function of effective emissivity of the sky (abscissa) and insolation (colour) for Alptal (**a**), Seehornwald (**b**), Sodankylä (**c**), Cherskiy (**d**), Abisko (**e**), Yakutsk (**f**), and Borden (**g**). Values for Yakutsk are shown only for nighttime. Errors are negative for underestimation by CLM4.5 and positive for overestimation by CLM4.5.

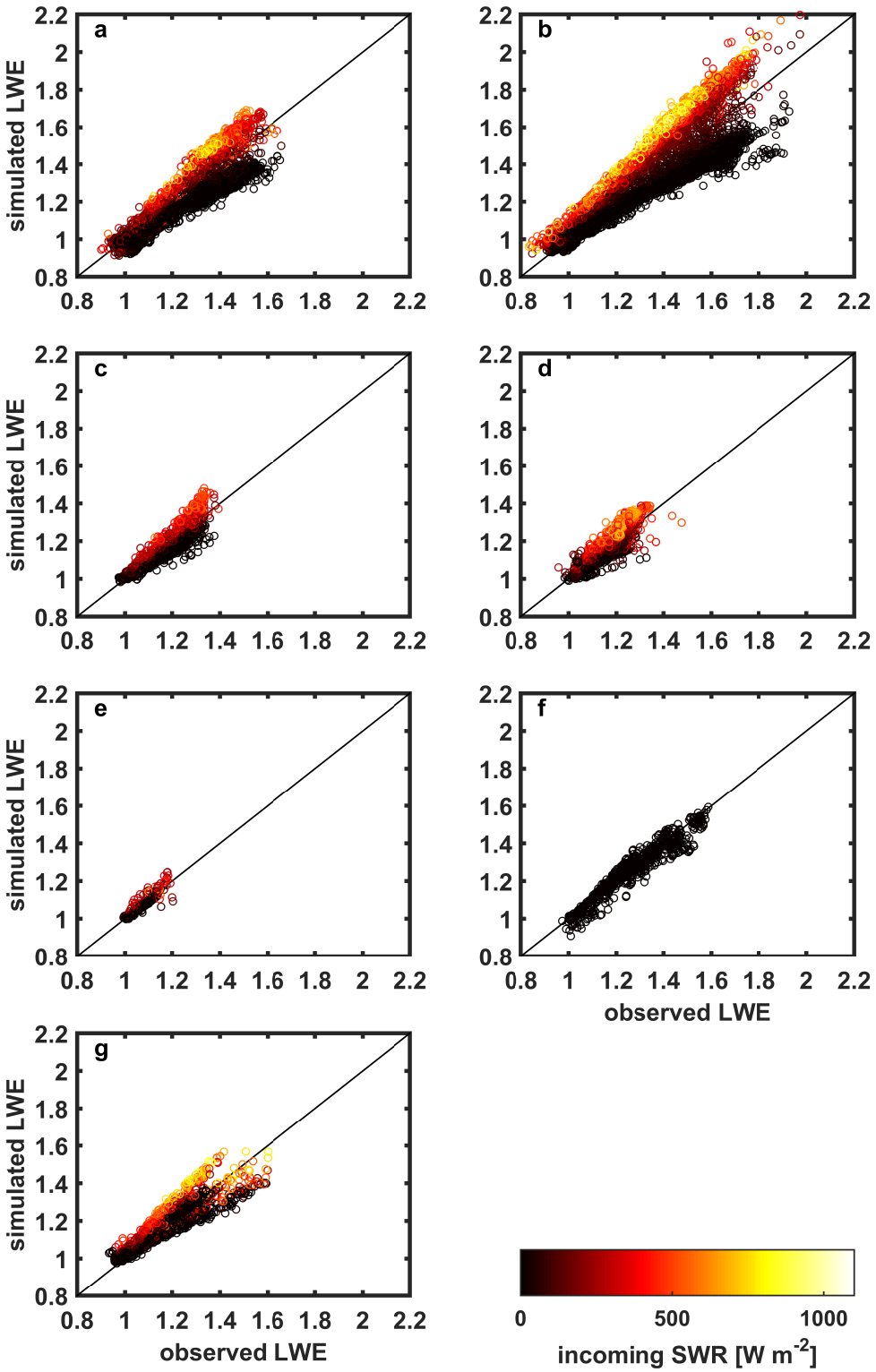

Figure 4.13: Comparison of observed longwave enhancement and longwave enhancement simulated by CLM4.5 as a function of insolation for Alptal (**a**), Seehornwald (**b**), Sodankylä (**c**), Cherskiy (**d**), Abisko (**e**), Yakutsk (**f**), and Borden (**g**). Values for Yakutsk are shown only for nighttime.

Table 4.3: Root-mean-square error (RMSE) and mean bias (MB) for sub-canopy longwave radiation simulated by CLM4.5 before and after (CLM4.5-BM) including a biomass heat storage parameterization and by SNOWPACK, which was only used for evergreen sites. Values for Alptal and Seehornwald were calculated for all years combined. *Values for Yakutsk were calculated only for nighttime.

Site	**RMSE** [$\mathrm{Wm^{-2}}$]			**MB** [$\mathrm{Wm^{-2}}$]		
	CLM4.5	**CLM4.5-BM**	**SNOWPACK**	**CLM4.5**	**CLM4.5-BM**	**SNOWPACK**
Abisko	5.65	5.47	-	0.70	0.64	-
Alptal	18.39	14.72	9.35	-7.84	-5.63	-1.05
Borden	11.27	10.79	-	3.37	4.55	-
Cherskiy	11.30	10.55	-	0.70	0.86	-
Seehornwald	22.31	15.75	11.70	1.53	10.44	9.87
Sodankylä	10.45	9.20	12.35	-0.80	-0.08	-7.96
Yakutsk	6.92*	8.45*	-	-0.37*	1.46*	-

The impact of vegetation density on longwave enhancement can be seen in Figure 4.14. PDFs of observed longwave enhancement reveal a bimodal distribution for every site except Abisko and Borden. The first peak occurs for longwave enhancement values around 1 indicating little to no effect of the vegetation, which coincides with high ε_{sky} (overcast conditions). This peak is generally well represented by CLM4.5 except for Cherskiy. The second peak of observed longwave enhancement occurs for varying longwave enhancement values across sites and changes in accordance with vegetation density and ε_{sky}. Higher vegetation density and lower ε_{sky} result in higher longwave enhancement. For the dense forests at Alptal and Seehornwald, the second peak is clearly distinguishable from the first. Peaks are closer for Sodankylä and overlap for Cherskiy and Yakutsk, while there is no distinction for Abisko. The frequency of longwave enhancement is in accordance with the frequency of ε_{sky} (Figure 4.6), so that the second peak of longwave enhancement is more dominant for Cherskiy and Yakutsk while there is no clear second peak for Borden. Over- and underestimations by CLM4.5 found in Figures 4.12 and 4.13 can be seen for PDFs and result in a separation of the second peak, which is more evident for the dense forests at Alptal and Seehornwald. For Sodankylä, CLM4.5 simulates no clear second peak, while the first and split-up second peak overlap for Cherskiy due to low vegetation density. For Abisko and Borden, CLM4.5 simulates the PDF of longwave enhancement well. In contrast to CLM4.5, SNOWPACK simulates a clear bimodal distribution of longwave enhancement for each evergreen forest stand. SNOWPACK simulates the second peak well for Alptal, for which it was calibrated, but overestimates (underestimates) the longwave enhancement value of the second peak for Seehornwald (Sodankylä) due to higher (lower) vegetation density compared to Alptal.

4.6 Impact of biomass heat storage on simulation of longwave enhancement by CLM4.5

As a test for potential improvement of CLM4.5, SNOWPACK's biomass heat storage parameterization has been included and resulting PDFs of longwave enhancement are shown as dashed lines in Figure 4.14. Inclusion of biomass heat storage displays little to no impact for Abisko, Borden, Cherskiy, Sodankylä, and Yakutsk due to small volumes of biomass. A clear impact on underestimation of the second peak can be seen for Alptal and Seehornwald, and less so for Sodankylä, while there is little impact on overestimation. Consequently, inclusion of biomass heat storage has a net positive effect on simulated sub-canopy longwave radiation, which can be seen in increasing MB values except for the sparsest vegetation at Abisko (Table 4.3). However, RMSE values are reduced by including biomass heat storage for all sites except Yakutsk. Change in RMSE and MB

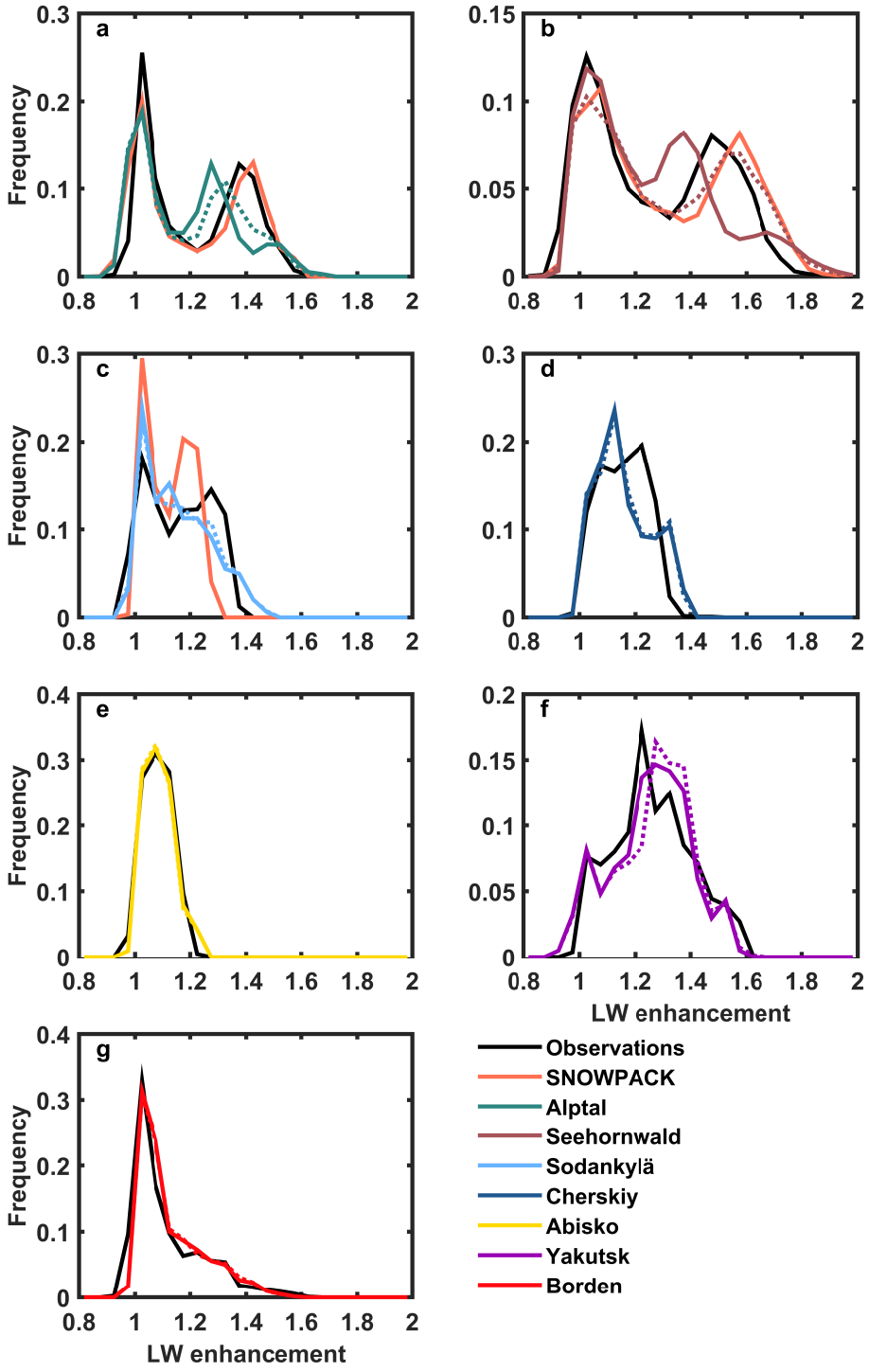

Figure 4.14: PDFs of longwave enhancement for observations (black), SNOWPACK (orange), CLM4.5 (coloured, solid), and CLM4.5 including biomass heat storage (coloured, dashed) for (**a**) Alptal (green), (**b**) Seehornwald (maroon), (**c**) Sodankylä (light blue), (**d**) Cherskiy (dark blue), (**e**) Abisko (yellow), (**f**) Yakutsk (violet), and (**g**) Borden (red). PDF for Yakutsk was calculated from nighttime values. Note that PDFs for SNOWPACK were calculated from simulations shown in Figure 4.8 without calibration for sites Seehornwald and Sodankylä.

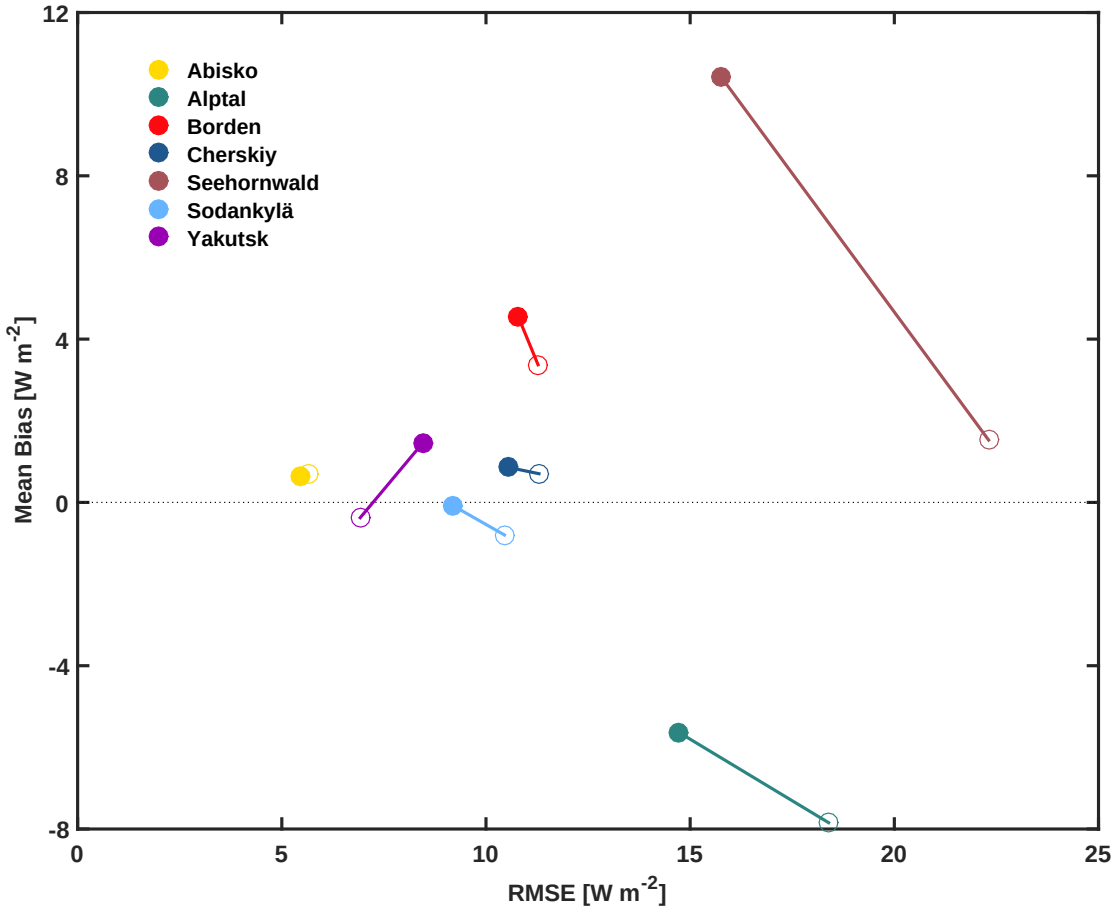

Figure 4.15: Change in RMSE and MB (as shown in Table 4.3) for sub-canopy longwave radiation simulated by CLM4.5 before (empty circles) and after (filled circles) including a biomass heat storage parameterization for Abisko (yellow), Alptal (green), Borden (red), Cherskiy (dark blue), Seehornwald (maroon), Sodankylä (light blue), and Yakutsk (violet). Values for Yakutsk were calculated only for nighttime

due to implementation of biomass heat storage is illustrated in Figure 4.15. The impact on metrics is consistent across evergreen forest stands, Borden, and Cherskiy with decreasing RMSE and increasing MB. Impact on RMSE differs for Yakutsk likely because evaluation was restricted to nighttime values. Note that the magnitude of change in metrics depends on tree height and basal area but does not necessarily correspond to vegetation density (see Tables 3.1 and 4.1).

Implementation of biomass heat storage reveals a substantial improvement of simulations by CLM4.5 for dense evergreen forests, as evident from reduced RMSE of sub-canopy longwave radiation (Table 4.3) and more coalesced second peaks in PDFs of longwave enhancement (Figure 4.14). This raises the question whether a parameterization of biomass heat storage alone can correct the simulation of sub-canopy longwave radiation by CLM4.5, which is explored by performing simulations with different values of biomass

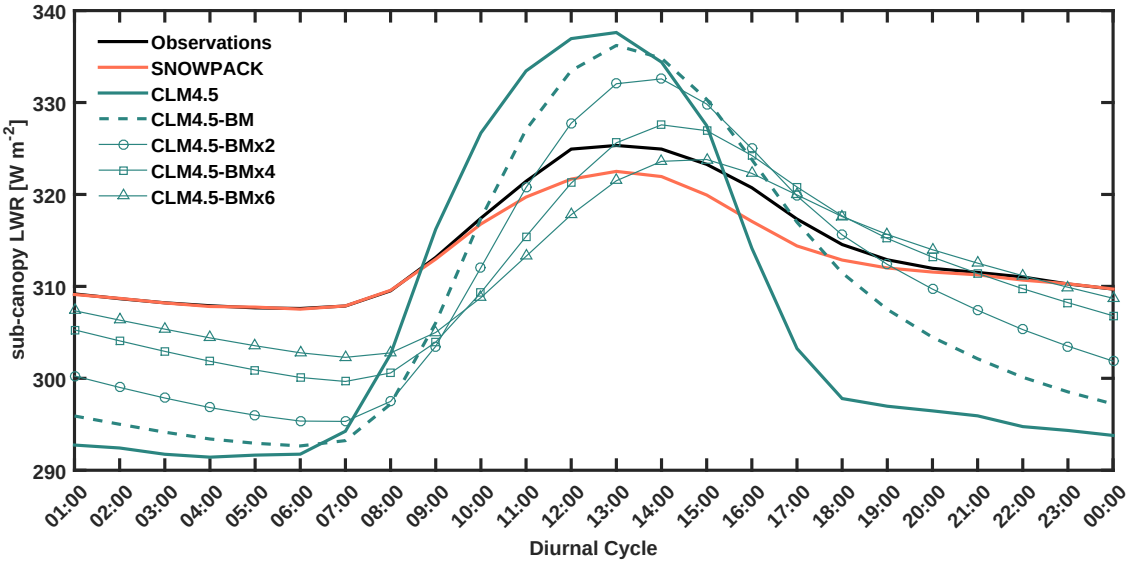

Figure 4.16: Diurnal cycle of sub-canopy longwave radiation at Alptal for observations (black), SNOWPACK (orange), and CLM4.5 (green) before (solid) and after (dashed) implementation of biomass heat storage as well as after implementing theoretical increased biomass values: biomass multiplied by 2 (line with superimposed circles), multiplied by 4 (line with superimposed squares), and multiplied by 6 (line with superimposed triangles).

volume. Alptal was chosen as test site for these simulations since SNOWPACK's parameterization of biomass heat storage had been developed for this site by *Gouttevin et al.* (2015) determining its biomass volume, which is multiplied by factors of 1, 2, 4, and 6 for test simulations. Increasing biomass volume results in a decrease of the diurnal cycle of sub-canopy longwave radiation, however, a substantial overestimation of biomass is necessary for the diurnal range of sub-canopy longwave radiation to become similar to observations (Figure 4.16). Moreover, thermal inertia due to increasing biomass volume delays the diurnal cycle of sub-canopy longwave radiation and leads to an unrealistic timing, which eventually results in an increase of RMSE values before the observed diurnal range can be reached (Table 4.4). Note that even an overestimation of biomass volume by several times does not yield the same skill as simulation by SNOWPACK, highlighting the impact of a sheltering upper canopy layer. Furthermore, CLM4.5 simulations including biomass heat storage display a consistent cooling and thus decrease of sub-canopy longwave radiation during night, as release of heat from biomass slows but can't entirely compensate for nighttime cooling, while neither observations nor SNOWPACK display a substantial decrease of sub-canopy longwave radiation throughout the night.

Table 4.4: Root-mean-square error (RMSE) and mean bias (MB) for sub-canopy longwave radiation simulated by CLM4.5 before and after (CLM4.5-BM) including a biomass heat storage parameterization and by SNOWPACK. CLM4.5-BMx2, CLM4.5-BMx4, and CLM4.5-BMx6 denote multiplication of biomass by factors 2, 4, and 6 in the respective model version. Values for CLM4.5, CLM4.5-BM, and SNOWPACK are the same as the ones given in Table 4.3.

Model	**RMSE** [$\mathrm{Wm^{-2}}$]	**MB** [$\mathrm{Wm^{-2}}$]
CLM4.5	18.39	-7.84
CLM4.5-BM	14.72	-5.63
CLM4.5-BMx2	12.84	-4.16
CLM4.5-BMx4	11.73	-2.68
CLM4.5-BMx6	11.88	-2.37
SNOWPACK	9.35	-1.05

4.7 Influence of vegetation density on simulation error

As seen in Figure 4.12 and Table 4.3, errors in sub-canopy longwave radiation simulated by CLM4.5 are smaller for sparsely vegetated sites compared to densely vegetated sites. Observations of atmospheric longwave radiation are used in Equation (2.6) leaving two potential sources of simulation errors, vegetation temperature T_{veg} and vegetation emissivity ε_v. Schematically, equal absolute errors in vegetation temperature result in smaller errors in sub-canopy longwave radiation for sparse compared to dense vegetation due to the weighing by vegetation emissivity. Vegetation temperatures simulated by CLM4.5 (without biomass heat storage) and inferred from observed sub-canopy longwave radiation are compared to examine differences in errors solely caused by simulated vegetation temperatures (Figure 4.17). Vegetation temperatures were inferred from observations by inverting Equation (2.6) and using vegetation emissivity calculated by CLM4.5 (Equation (2.5)).

Observations indicate similar average diurnal ranges of vegetation temperatures for the dense vegetation at Alptal and Seehornwald. Vegetation temperatures are lower on average at Seehornwald, likely caused by differences in evaluation periods and higher elevation of Seehornwald resulting in lower air temperatures (see Table 4.1 and Figure 4.5). Interannual variability is higher for Alptal than for Seehornwald, which is tied to differences in evaluation periods at Alptal (Table 4.1). Observations for Sodankylä and Cherskiy indicate higher average diurnal ranges of vegetation temperatures for sparser vegetation. Different ranges of vegetation temperatures between Sodankylä and Cher-

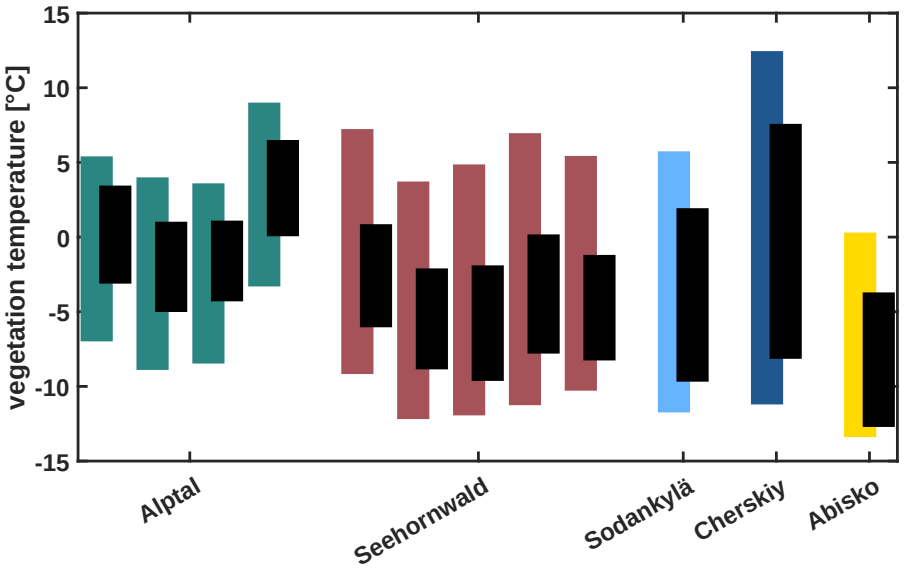

Figure 4.17: Comparison of average diurnal ranges of vegetation temperature calculated from observed sub-canopy longwave radiation (black) and sub-canopy longwave radiation simulated by CLM4.5 without biomass heat storage (coloured) for Alptal (green, individual years), Seehornwald (maroon, individual years), Sodankylä (light blue), Cherskiy (dark blue), and Abisko (yellow). Borden is excluded from this analysis as the forest stand consists of multiple PFTs and uncertainty in fractions of PFTs affects the calculation of vegetation emissivities. Yakutsk is excluded as only nighttime values are used for this site.

skiy are likely caused by differences in air temperatures, insolation, and ε_{sky} (Figures 4.5 and 4.6). Ranges of vegetation temperatures at Abisko are small compared to all other sites, however, evaluation period is substantially shorter at Abisko (Table 4.1). CLM4.5 overestimates average diurnal ranges of vegetation temperatures, extending both above and below observations. Average diurnal ranges of simulated vegetation temperatures are similar for Seehornwald and Sodankylä and slightly smaller for Alptal. As observations indicate a larger average diurnal range for Sodankylä than for the densely vegetated sites at Alptal and Seehornwald, simulated vegetation temperatures are closer to those inferred from observations for Sodankylä compared to Alptal and Seehornwald, which is also found for the deciduous, sparser vegetation at Abisko and Cherskiy.

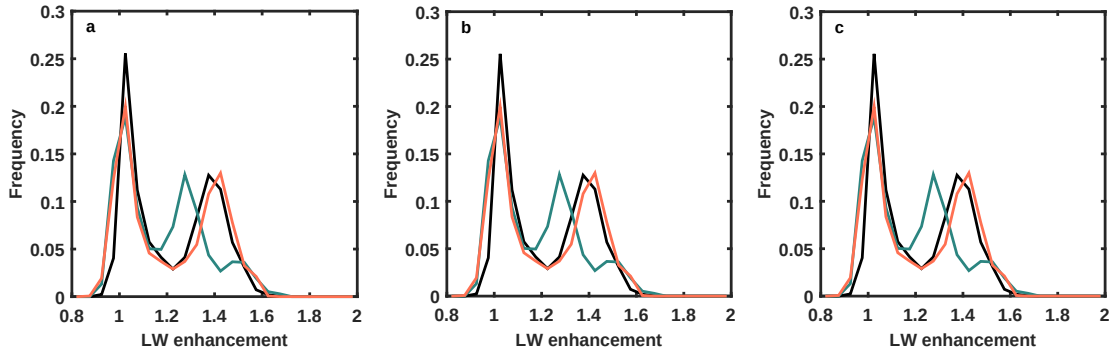

Figure 4.18: PDFs of longwave enhancement at Alptal for observations (black), CLM4.5 (green), and SNOWPACK (orange) with shaded intervals representing changes over a range of -20% to +20% for ground albedo (**a**), fraction of diffuse shortwave radiation (**b**), and soil water content (**c**). Shaded intervals are indiscernible indicating little sensitivity of simulated sub-canopy longwave radiation to approximations as represented by changes in RMSE and MB of less than ± 0.02 Wm^{-2}.

4.8 Sensitivity studies

4.8.1 Interception of precipitation for SNOWPACK

The Toy Model is designed to prescribe intercepted precipitation calculated by CLM4.5 for both models, so that CLM4.5 and SNOWPACK calculate sub-canopy longwave radiation from the same forcing data for every time step. This results in adjustment of interception by evaporation not being carried over to the next timestep in SNOWPACK (as the value from CLM4.5 is used). The consequent impact on simulated sub-canopy longwave radiation is tested by using the parameterization for interception of precipitation from CLM4.5 but running SNOWPACK independently. The effect is miniscule as indicated by root-mean-square error (RMSE) and mean bias (MB) values: RMSE of 9.41 Wm^{-2} (in comparison to 9.35 Wm^{-2} in Table 3) and MB of -0.96 Wm^{-2} (-1.05 Wm^{-2}) for Alptal, RMSE of 11.73 Wm^{-2} (11.70 Wm^{-2}) and MB of 9.88 Wm^{-2} (9.87 Wm^{-2}) for Seehornwald, and RMSE of 12.34 Wm^{-2} (12.35 Wm^{-2}) and MB of -7.92 Wm^{-2} (-7.96 Wm^{-2}) for Sodankylä.

4.8.2 Approximations of forcing data and parameters

Alptal, Switzerland RMSE and MB values given in Table 4.3 show little sensitivity to approximations of ground albedo, fraction of diffuse shortwave radiation, and soil water content as variations in approximations by $\pm 20\%$ result in changes in RMSE and MB of less than ± 0.02 Wm^{-2} (not shown here). For CLM4.5, RMSE values increase with

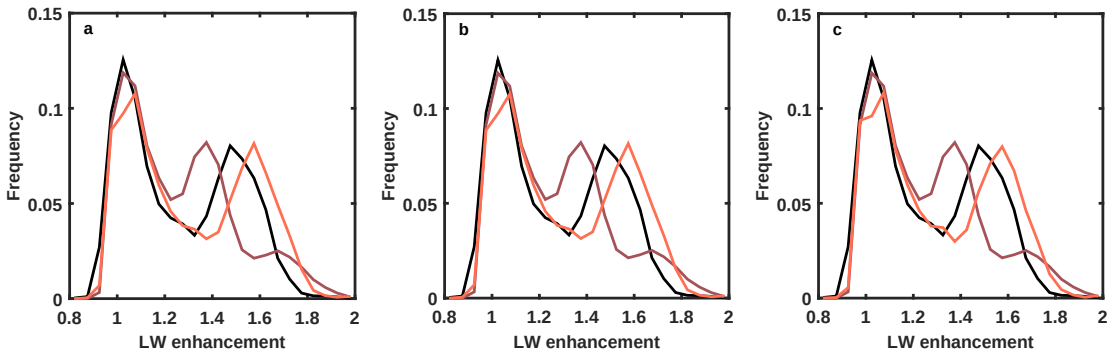

Figure 4.19: PDFs of longwave enhancement at Seehornwald for observations (black), CLM4.5 (maroon), and SNOWPACK (orange) with shaded intervals representing changes over a range of -20% to +20% for ground albedo (**a**), fraction of diffuse shortwave radiation (**b**), and snow depth (**c**). Shaded intervals are indiscernible indicating little sensitivity of simulated sub-canopy longwave radiation to approximations as represented by changes in RMSE and MB of less than ± 0.02 Wm^{-2}.

increasing ground albedo as well as decreasing fraction of diffuse shortwave radiation and soil water content, while MB increases with decreasing fraction of diffuse shortwave radiation as well as increasing ground albedo and soil water content. For SNOWPACK, RMSE increases with decreasing ground albedo, fraction of diffuse shortwave radiation, and soil water content, while MB increases with increasing ground albedo and fraction of diffuse shortwave radiation as well as decreasing soil water content. Sensitivity for PDFs of longwave enhancement is shown in Figure 4.18 and little sensitivity to approximations is indicated by small shaded intervals.

Seehornwald, Switzerland RMSE and MB values given in Table 4.3 show little sensitivity to approximations of ground albedo, fraction of diffuse shortwave radiation, and snow depth as variations in approximations by $\pm 20\%$ result in changes in RMSE and MB of less than ± 0.02 Wm^{-2} (not shown here). For CLM4.5, RMSE values increase with increasing ground albedo as well as decreasing fraction of diffuse shortwave radiation and snow depth, while MB increases with ground albedo, fraction of diffuse shortwave radiation, and snow depth. For SNOWPACK, both RMSE and MB increase with increasing ground albedo and fraction of diffuse shortwave radiation as well as decreasing snow depth. Sensitivity for PDFs of longwave enhancement is shown in Figure 4.19 and little sensitivity to approximations is indicated by small shaded intervals.

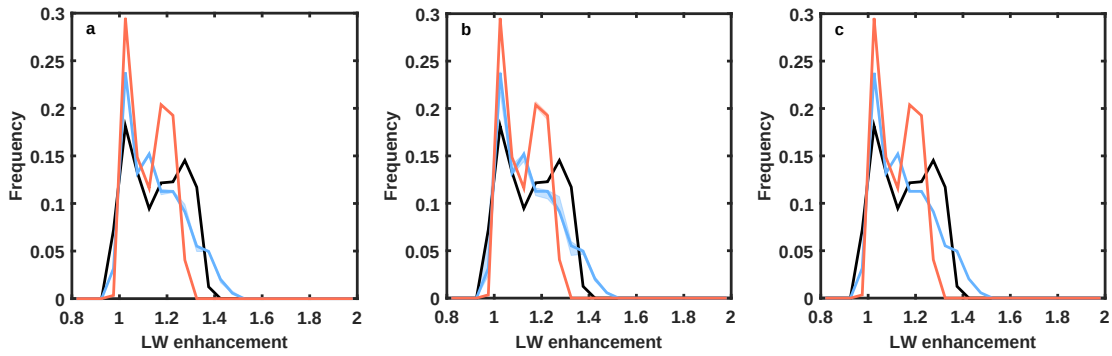

Figure 4.20: PDFs of longwave enhancement at Sodankylä for observations (black), CLM4.5 (light blue), and SNOWPACK (orange) with shaded intervals representing changes over a range of -20% to +20% for ground albedo (**a**), surface temperature (**b**), and soil water content (**c**).

Sodankylä, Finland Sensitivity of RMSE and MB values to approximations of ground albedo, surface temperature, and soil water content are shown in Table 4.5; sensitivity for PDFs of longwave enhancement is shown in Figure 4.20. RMSE and MB display little sensitivity to any of the approximations for SNOWPACK, and shaded intervals are indiscernible for PDFs of longwave enhancement simulated by SNOWPACK. For CLM4.5, RMSE and MB show sensitivity to ground albedo and higher sensitivity to surface temperature, but PDFs of longwave enhancement are not substantially affected. Both RMSE and MB increase for CLM4.5 with ground albedo, and MB increases with decreasing surface temperature. RMSE for CLM4.5 decreases for any change in surface temperature. While sensitivity does not substantially impact RMSE, variation in surface temperature can change sign of MB.

Table 4.5: Sensitivity of RMSE and MB to parameter choices for CLM4.5 and SNOWPACK for Sodankylä. Parameters are changed over a range of -20% to +20%, limited to 1 for ground albedo and soil water content. Resulting changes in RMSE values refer to 10.45 Wm^{-2} for CLM4.5 and 12.35 Wm^{-2} for SNOWPACK; resulting changes in MB values refer to -0.80 Wm^{-2} for CLM4.5 and -7.96 Wm^{-2} for SNOWPACK (given in Table 4.3). Surface temperature was varied by changing the difference between evaluation period average and 0°C over a range of -20% to +20% while still limiting to a maximum of 0°C.

Change	**RMSE** [Wm^{-2}]						**MB** [Wm^{-2}]					
	CLM4.5			**SNOWPACK**			**CLM4.5**			**SNOWPACK**		
	α_{gr}	SWC	T_{surf}	α_{gr}	SWC	T_{surf}	α_{gr}	SWC	T_{surf}	α_{gr}	SWC	T_{surf}
-20%	-0.32	0	-0.36	+0.02	+0.00	-0.04	-0.32	0	+1.53	-0.03	-0.00	+0.07
-16%	-0.24	0	-0.30	+0.01	+0.00	-0.03	-0.25	0	+1.24	-0.02	-0.00	+0.05
-12%	-0.18	0	-0.24	+0.01	+0.00	-0.03	-0.19	0	+0.94	-0.02	-0.00	+0.04
-8%	-0.12	0	-0.19	+0.01	+0.00	-0.02	-0.12	0	+0.63	-0.01	-0.00	+0.03
-4%	-0.06	0	-0.11	+0.00	+0.00	-0.01	-0.06	0	+0.31	-0.01	-0.00	+0.01
0%	0	0	0	0	0	0	0	0	0	0	0	0
+4%	+0.06	0	-0.11	-0.00	-0.00	+0.01	+0.06	0	-0.38	+0.01	+0.00	-0.02
+8%	+0.13	0	–0.24	0.01	-0.00	+0.02	+0.13	0	-0.75	+0.01	+0.00	-0.03
+12%	+0.20	0	-0.38	-0.01	-0.00	+0.03	+0.20	0	-1.14	+0.02	+0.00	-0.05
+16%	+0.27	0	-0.56	-0.01	-0.00	+0.04	+0.26	0	-1.52	+0.02	+0.00	-0.07
+20%	+0.34	0	-0.75	-0.02	-0.00	+0.05	+0.33	0	-1.87	+0.03	+0.00	-0.08

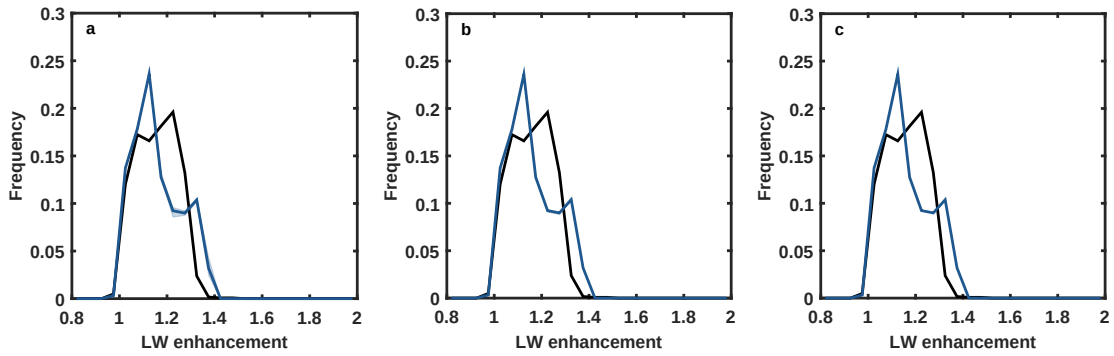

Figure 4.21: PDFs of longwave enhancement at Cherskiy for observations (black) and CLM4.5 (dark blue) with shaded intervals representing changes over a range of -20% to +20% for ground albedo (**a**), fraction of diffuse SWR (**b**), and snow depth (**c**).

Cherskiy, Russia Sensitivity of RMSE and MB for simulations by CLM4.5 to approximations of ground albedo, fraction of diffuse shortwave radiation, and snow depth is shown in Table 4.6, with little sensitivity to fraction of diffuse shortwave radiation and no sensitivity to prescribed snow depth. Both RMSE and MB increase with ground albedo.

Table 4.6: Sensitivity of RMSE and MB to parameter choices for CLM4.5 for Cherskiy. Parameters are changed over a range of -20% to +20%, limited to 1 for ground albedo and fraction of diffuse shortwave radiation. Resulting changes in RMSE and MB values refer to RMSE of 11.30 Wm^{-2} and MB of 0.70 Wm^{-2} (given in Table 4.3).

Change	**RMSE** [Wm^{-2}]			**MB** [Wm^{-2}]		
	α_{gr}	f_{diff}	z_{snow}	α_{gr}	f_{diff}	z_{snow}
-20%	-0.37	-0.01	0	-0.40	+0.06	0
-16%	-0.30	-0.01	0	-0.32	+0.05	0
-12%	-0.23	-0.01	0	-0.24	+0.04	0
-8%	-0.15	-0.00	0	-0.17	+0.02	0
-4%	-0.07	-0.00	0	-0.08	+0.01	0
0%	0	0	0	0	0	0
+4%	+0.08	+0.00	0	+0.08	-0.02	0
+8%	+0.16	+0.00	0	+0.18	-0.03	0
+12%	+0.24	+0.00	0	+0.26	-0.04	0
+16%	+0.33	+0.01	0	+0.35	-0.05	0
+20%	+0.42	+0.01	0	+0.43	-0.06	0

Sensitivity of PDFs of longwave enhancement is shown in Figure 4.21, and PDFs are not affected by changes in approximations. Sensitivity of RMSE and MB to variations in SAI is shown to in Tables 4.9 and 4.10, respectively, and discussed in Chapter 4.8.3.

Abisko, Sweden Sensitivity of RMSE and MB values for simulations by CLM4.5 to approximations of ground albedo, soil water content, and surface temperature are shown in Table 4.7. Similarly to Sodankylä, metrics display no sensitivity to soil water content and more sensitivity to surface temperature than ground albedo. MB increases with ground albedo and surface temperature, and it changes sign within the tested range of surface temperature. RMSE increases with ground albedo and almost consistently increases with both increasing and decreasing surface temperature. Sensitivity of PDFs of longwave enhancement is shown in Figure 4.22. Shaded intervals are only discernible for variations in surface temperature, reiterating sensitivity found for RMSE and MB values, but do not affect the shape of the PDF, especially since small, sparse vegetation at Abisko leads to overlapping peaks of longwave enhancement.

Table 4.7: Sensitivity of RMSE and MB to parameter choices for CLM4.5 for Abisko. Parameters are changed over a range of -20% to +20%, limited to 1 for ground albedo and soil water content. Resulting changes in RMSE and MB values refer to RMSE of 5.65 Wm^{-2} and MB of 0.70 Wm^{-2} (given in Table 4.3). Surface temperature was varied by changing the difference between evaluation-period average and 0°C over a range of -20% to +20% while still limiting to a maximum of 0°C.

Change	**RMSE** [Wm^{-2}]			**MB** [Wm^{-2}]		
	α_{gr}	SWC	T_{surf}	α_{gr}	SWC	T_{surf}
-20%	-0.48	0	+0.72	-0.43	0	-1.26
-16%	-0.39	0	+0.58	-0.34	0	-1.02
-12%	-0.32	0	+0.42	-0.27	0	-0.78
-8%	-0.22	0	+0.22	-0.18	0	-0.56
-4%	-0.09	0	+0.08	-0.08	0	-0.28
0%	0	0	0	0	0	0
+4%	+0.11	0	-0.03	+0.09	0	+0.21
+8%	+0.22	0	-0.05	+0.17	0	+0.43
+12%	+0.31	0	-0.02	+0.25	0	+0.66
+16%	+0.43	0	+0.02	+0.34	0	+0.90
+20%	+0.55	0	+0.08	+0.42	0	+1.15

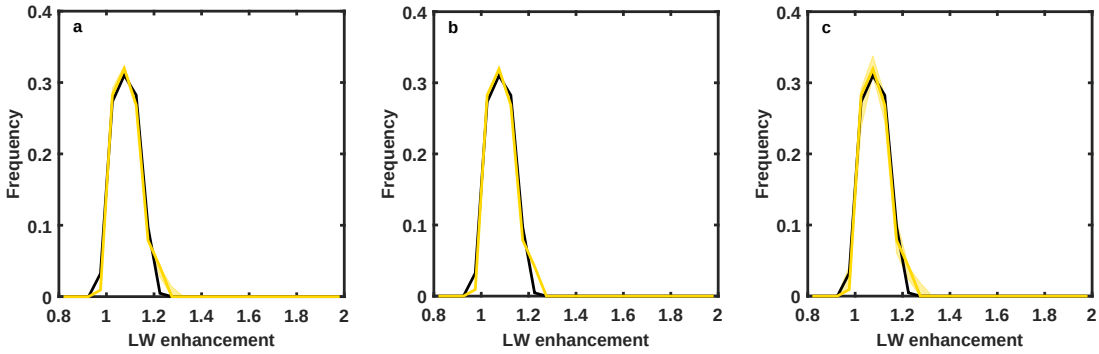

Figure 4.22: PDFs of longwave enhancement at Abisko for observations (black) and CLM4.5 (yellow) with shaded intervals representing changes over a range of -20% to +20% for ground albedo (**a**), soil water content (**b**), and surface temperature (**c**).

Yakutsk, Russia RMSE and MB values given in Table 4.3 show little sensitivity to approximations of ground albedo, fraction of diffuse shortwave radiation, and snow depth as variations in approximations by $\pm 20\%$ result in changes in RMSE and MB of less than ± 0.01 Wm^{-2} (not shown here). RMSE values increase for decreasing ground albedo and increasing fraction of diffuse shortwave radiation, while there is no effect due to small variations in snow depth. MB values increase for increasing ground albedo and decreasing fraction of diffuse shortwave radiation, while there is no effect due to small variations in snow depth. Sensitivity for PDFs of longwave enhancement is shown in Figure 4.23 and little sensitivity to approximations is indicated by small shaded intervals. Little sensitivty is expected as evaluation is limited to nighttime.

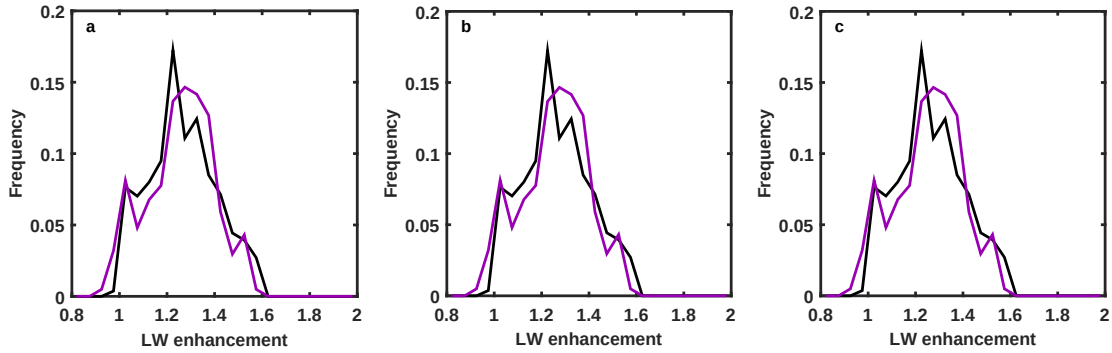

Figure 4.23: PDFs of nighttime longwave enhancement at Yakutsk for observations (black) and CLM4.5 (violet) with shaded intervals representing changes over a range of -20% to +20% for ground albedo (**a**), fraction of diffuse shortwave radiation (**b**), and snow depth (**c**).

Borden, Canada Sensitivity of RMSE and MB values to approximations of ground albedo, fraction of diffuse shortwave radiation, PFT fractions, and snow depth is shown in Table 4.8. Both RMSE and MB display no sensitivity to variations in prescribed snow depth and increase with ground albedo, fraction of diffuse shortwave radiation, and fraction of evergreen needleleaf trees. Variations in those 3 parameters have little impact on RMSE, and ground albedo and fraction of diffuse shortwave radiation have also little impact on MB. MB displays a higher degree of sensitivity to fraction of evergreen needleleaf trees, however, variation in none of the parameters exhibits impact on PDFs of longwave enhancement (Figure 4.24).

Table 4.8: Sensitivity of RMSE and MB to parameter choices for CLM4.5 for Borden. Parameters are changed over a range of -20% to +20%, limited to 1 for ground albedo, fraction of diffuse shortwave radiation, and PFT fractions. Resulting changes in RMSE and MB values refer to RMSE of 11.27 Wm^{-2} and MB of 3.37 Wm^{-2} (given in Table 4.3).

Change	**RMSE** [Wm^{-2}]				**MB** [Wm^{-2}]			
	α_{gr}	f_{diff}	f_{PFT}	z_{snow}	α_{gr}	f_{diff}	f_{PFT}	z_{snow}
-20%	-0.09	-0.02	-0.02	0	-0.09	-0.00	-0.36	0
-16%	-0.07	-0.02	-0.02	0	-0.08	-0.00	-0.28	0
-12%	-0.06	-0.01	-0.01	0	-0.06	-0.00	-0.21	0
-8%	-0.04	-0.01	-0.01	0	-0.04	-0.00	-0.14	0
-4%	-0.02	-0.00	-0.01	0	-0.02	-0.00	-0.07	0
0%	0	0	0	0	0	0	0	0
+4%	+0.02	+0.00	+0.01	0	+0.02	+0.00	+0.07	0
+8%	+0.04	+0.01	+0.01	0	+0.04	+0.00	+0.13	0
+12%	+0.06	+0.01	+0.02	0	+0.06	+0.00	+0.19	0
+16%	+0.08	+0.02	+0.02	0	+0.08	+0.00	+0.25	0
+20%	+0.10	+0.02	+0.04	0	+0.10	+0.00	+0.31	0

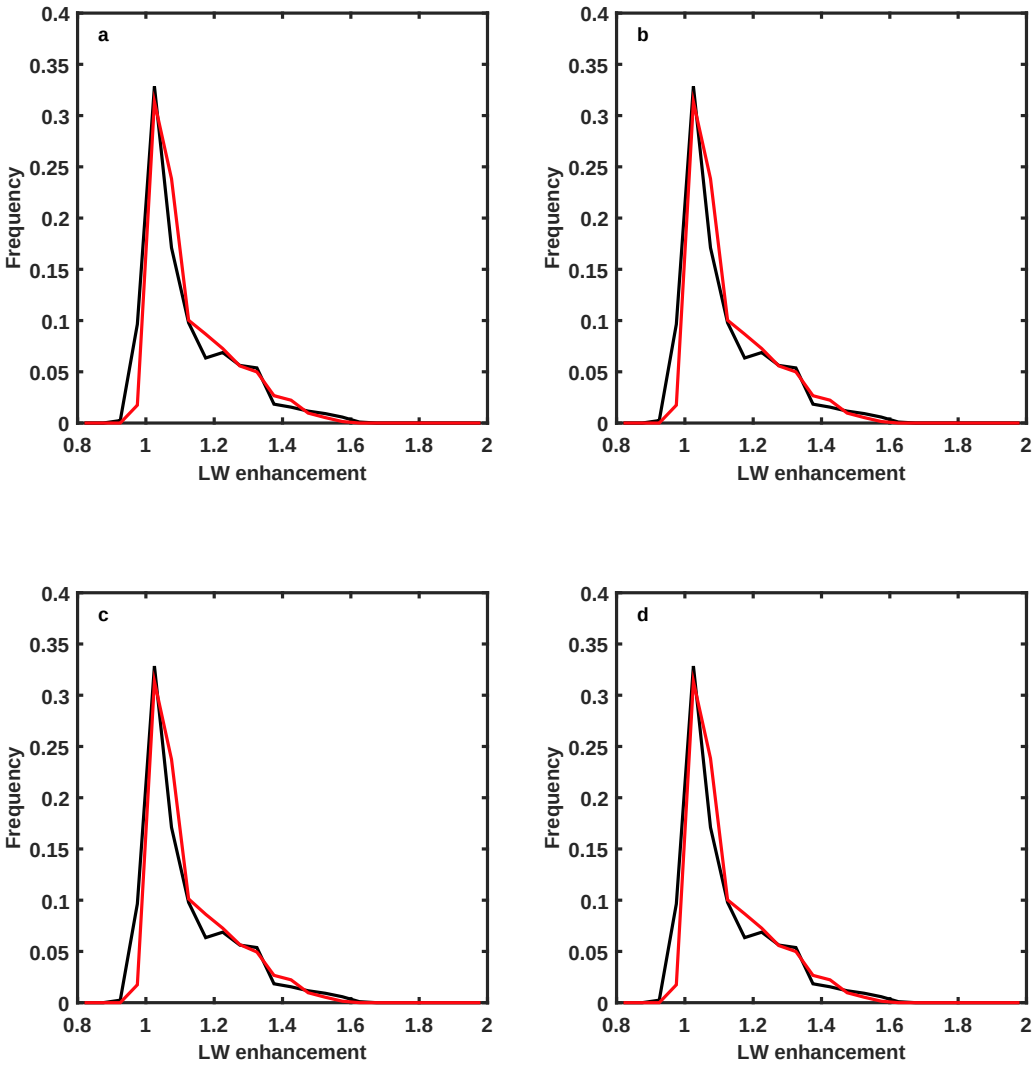

Figure 4.24: PDFs of longwave enhancement at Borden for observations (black) and CLM4.5 (red) with shaded intervals representing changes over a range of -20% to +20% for ground albedo (**a**), fraction of diffuse shortwave radiation (**b**), PFT fractions (**c**), and snow depth (**d**).

4.8.3 Sensitivity to plant area index (PAI)

Sensitivity of RMSE and MB values given in Table 4.3 to variations in plant area index (PAI) is shown in Tables 4.9 and 4.10, respectively. Generally, both models exhibit an increase in RMSE with vegetation density except for Sodankylä. For CLM4.5, minimum RMSE can be seen within the range of -16% to 0% for the low-vegetation density sites. No minimum RMSE can be found within the tested range for both high-vegetation density sites indicating the substantial RMSE values seen in Table 4.3. For SNOWPACK, changes in RMSE are generally smaller for Alptal compared to Seehornwald and Sodankylä representing the calibration of SNOWPACK to Alptal data. Sensitivity to changes in vegetation density are contrasting for Seehornwald and Sodankylä, which indicates the substantial differences in vegetation density between these sites and potential for calibration that was explored previously.

Mean biases are generally increasing with vegetation density due to enhancement of subcanopy longwave radiation by vegetation being scaled by vegetation density. Simulations by CLM4.5 for Alptal and Seehornwald display a contrasting sensitivity to vegetation density with decreasing mean bias for increasing vegetation density. This is likely due to asymmetric overestimations and underestimations seen for effective emissivity of the sky larger than 1 in Figure 4.12.

Sensitivity of PDFs of longwave enhancement is shown in Figure 4.25. Shaded areas show all values covered by variation in PAI around measured values and represent shifting locations of peaks in longwave enhancement. Although the location of peaks displays sensitivity to changes in vegetation density, the split-up second peak simulated by CLM4.5 is independent of these changes.

Table 4.9: Sensitivity of RMSE to plant area index (PAI) for CLM4.5 before implementation of biomass heat storage and for SNOWPACK. Values of PAI are changed over a range of -20% to +20% and resulting changes in RMSE are given in Wm^{-2} referring to values given in Table 4.3. Abbreviations for study sites are used: Abisko (Abi), Alptal (Alp), Borden (Bor), Cherskiy (Che), Seehornwald (SHW), Sodankylä (Sod), and Yakutsk (Yak).

Change	**CLM4.5**							**SNOWPACK**		
	Abi	Alp	Bor	Che	SHW	Sod	Yak	Alp	SHW	Sod
-20%	+0.16	-1.34	-0.10	-0.23	-0.72	+0.83	-0.28	-0.47	-2.67	+3.92
-16%	-0.04	-1.05	-0.19	-0.36	-0.48	+0.48	-0.40	-0.52	-2.05	+3.06
-12%	-0.14	-0.75	-0.20	-0.39	-0.31	+0.22	-0.41	-0.48	-1.47	+2.23
-8%	-0.17	-0.47	-0.16	-0.36	-0.18	+0.05	-0.33	-0.36	-0.93	+1.45
-4%	-0.13	-0.22	-0.09	-0.21	-0.07	-0.01	-0.18	-0.20	-0.44	+0.7
0%	0	0	0	0	0	0	0	0	0	0
+4%	+0.23	+0.19	+0.11	+0.29	+0.05	+0.07	+0.21	+0.22	+0.40	-0.66
+8%	+0.49	+0.37	+0.24	+0.61	+0.08	+0.21	+0.43	+0.44	+0.76	-1.27
+12%	+0.83	+0.52	+0.39	+0.97	+0.1	+0.38	+0.64	+0.66	+1.09	-1.84
+16%	+1.21	+0.65	+0.54	+1.35	+0.1	+0.61	+0.85	+0.88	+1.38	-2.35
+20%	+1.61	+0.76	+0.69	+1.77	+0.1	+0.85	+1.01	+1.09	+1.64	-2.82

Table 4.10: Sensitivity of MB to plant area index (PAI) for CLM4.5 before implementation of biomass heat storage and for SNOWPACK. Values of PAI are changed over a range of -20% to +20% and resulting changes in MB are given in Wm^{-2} referring to values given in Table 4.3. Abbreviations for study sites are used: Abisko (Abi), Alptal (Alp), Borden (Bor), Cherskiy (Che), Seehornwald (SHW), Sodankylä (Sod), and Yakutsk (Yak).

Change	**CLM4.5**							**SNOWPACK**		
	Abi	Alp	Bor	Che	SHW	Sod	Yak	Alp	SHW	Sod
-20%	-3.08	+0.66	-2.66	-4.63	+0.75	-3.97	-2.93	-2.98	-2.75	-3.99
-16%	-2.44	+0.54	-2.06	-3.62	+0.59	-3.11	-2.22	-2.26	-2.06	-3.15
-12%	-1.81	+0.42	-1.49	-2.66	+0.42	-2.27	-1.58	-1.61	-1.45	-2.33
-8%	-1.19	+0.28	-0.96	-1.75	+0.27	-1.49	-1.00	-1.02	-0.91	-1.53
-4%	-0.59	+0.15	-0.46	-0.86	+0.13	-0.72	-0.47	-0.49	-0.43	-0.75
0%	0	0	0	0	0	0	0	0	0	0
+4%	+0.60	-0.15	+0.45	+0.83	-0.12	+0.69	+0.42	+0.44	+0.38	+0.73
+8%	+1.18	-0.26	+0.87	+1.62	-0.22	+1.34	+0.81	+0.84	+0.72	+1.45
+12%	+1.75	-0.39	+1.26	+2.39	-0.32	+1.97	+1.15	+1.20	+1.02	+2.14
+16%	+2.32	-0.50	+1.62	+3.12	-0.41	+2.56	+1.44	+1.53	+1.28	+2.81
+20%	+2.87	-0.61	+1.96	+3.85	-0.49	+3.12	+1.70	+1.83	+1.52	+3.47

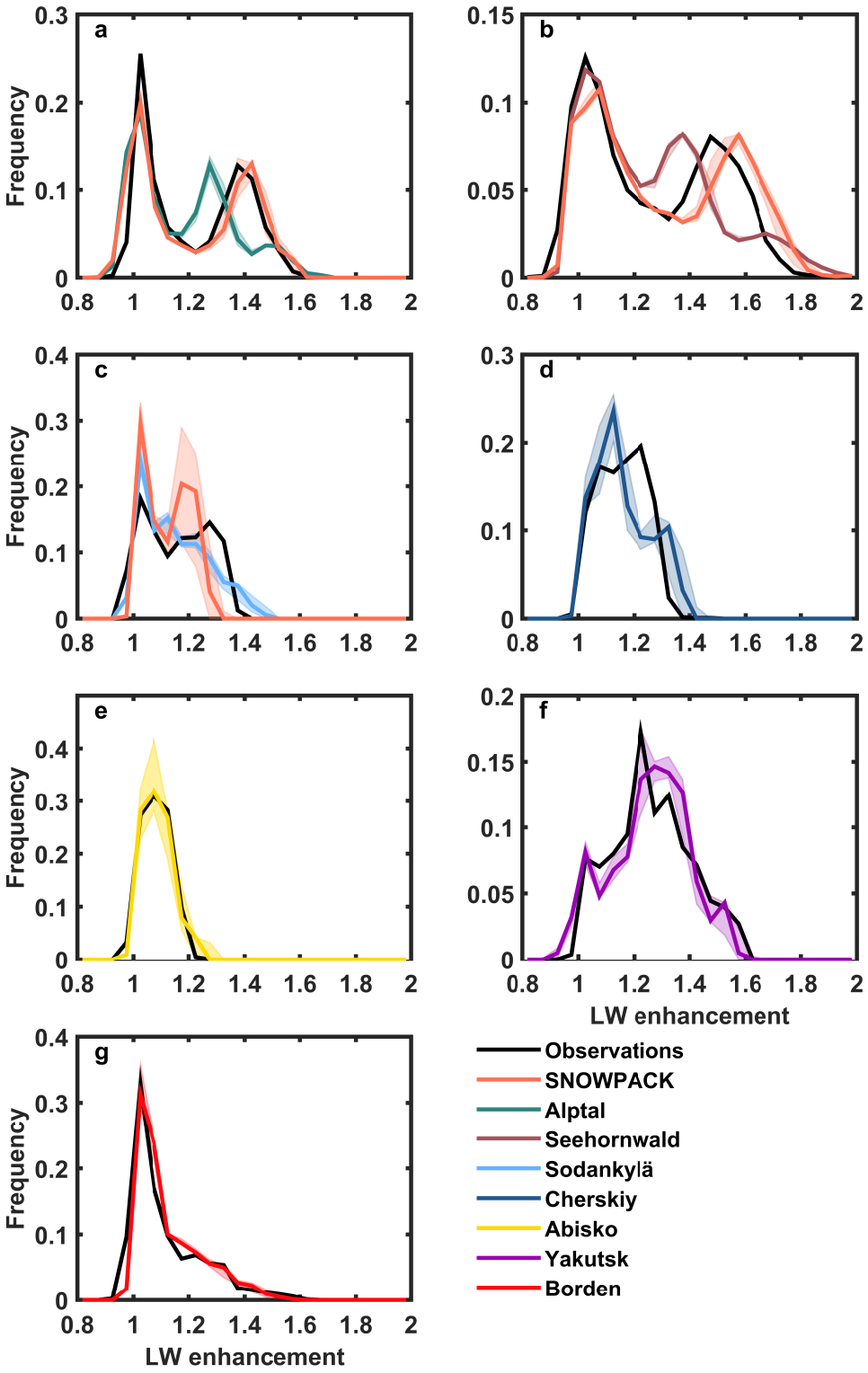

Figure 4.25: PDFs of longwave enhancement as given in Figure 4.14 (solid) and effect of varying plant area index (PAI, shaded intervals). PDFs for Yakutsk were calculated from nighttime values. PDFs are given for CLM4.5 before implementation of biomass heat storage.

4.9 Discussion

Magnitude and range of longwave enhancement vary across forest stands and depend on meteorological conditions as well as vegetation density and structure. Except for Abisko (small, sparse vegetation) and Borden (primarily overcast conditions), a substantial impact of vegetation on longwave radiation can be seen (Figure 4.14). This is especially true for evergreen forests, which are the predominant vegetation type of boreal forests. Coincidentally, all three evergreen sites feature a bimodal distribution of ε_{sky}, indicating no domination of clear-sky or overcast conditions. At Seehornwald, which featured both the highest vegetation density and lowest ε_{sky}, observed hourly longwave enhancement values reached up to 2, i.e. doubling of sub-canopy compared to atmospheric longwave radiation, and observed hourly longwave enhancement values reached up to 1.6 even at the dense but (predominantly) deciduous forests near Borden and Yakutsk. These magnitudes indicate that longwave enhancement represents a substantial contribution to the surface energy balance below the canopy.

CLM4.5 overestimates sub-canopy longwave radiation during the day and underestimates sub-canopy longwave radiation at night, with larger errors occurring under clear-sky conditions. As the magnitude of longwave enhancement increases for clearer skies, CLM4.5 displays larger errors for higher longwave enhancement values. The range of over- and underestimation varies between sites as the contribution from vegetation depends on vegetation density. Higher vegetation density results in a higher fraction of sub-canopy longwave radiation being attributed to vegetation and consequently, simulation errors are more emphasized for dense compared to sparse vegetation. This results in RMSE and mean bias values for sub-canopy longwave radiation being sensitive to changes in vegetation density, however, the systematic deficiency in simulated longwave enhancement (Figure 4.14) persists independent of potential uncertainty in vegetation density. Furthermore, vegetation temperatures indicate an impact of vegetation density on the response of vegetation to meteorological conditions, which CLM4.5 fails to capture contributing to simulation errors differing between sites (Figure 4.17). Including a term that accounts for heat stored in vegetation biomass results in a net increase of sub-canopy longwave radiation, except for Abisko where vegetation is sparse and small, as this parameterization mostly affects vegetation temperatures during afternoon and evening by allowing the vegetation to remain warmer for longer. Consequently, there is little impact on the diurnal range of sub-canopy longwave radiation, however, net overestimations are enhanced (see Table 4.3).

Although SNOWPACK exhibits less skill for Seehornwald and Sodankylä compared to Alptal, for which it was calibrated, simulated sub-canopy longwave radiation consistently displays a small spread, which is substantially smaller than the spread simulated

by CLM4.5 for the dense forests at Alptal and Seehornwald. This suggests a consistent impact of a two-layer vegetation, which affects vegetation temperatures and subsequently sub-canopy longwave radiation both during daytime, by shading the lower layer, and during nighttime, by sheltering the lower layer from radiative cooling. However, this general damping of temperature variations in the lower vegetation layer contrasts with findings of higher variability of trunk temperatures compared to needle temperatures due to insolation (*Pomeroy et al.*, 2009), further highlighting the role and importance of vegetation density. SNOWPACK was calibrated by *Gouttevin et al.* (2015) using Alptal data and not adjusted for this study. Consequently, mean biases are substantially larger in absolute terms for Seehornwald and Sodankylä, which feature varying vegetation density. Higher vegetation density at Seehornwald results in net overestimation, while lower vegetation density at Sodankylä results in net underestimation. Calibration leads to substantial improvement of simulated sub-canopy longwave radiation, which is mostly due to adjusting extinction of radiation (Equations (2.11) and (2.12)) in accordance with vegetation density. However, net underestimation is persistent for Sodankylä across the range of extinction coefficients, and calibration yields contrasting distributions of vegetation density into upper and lower layers between the fir-and-spruce forest at Seehornwald and the pine forest near Sodankylä. This suggests that absorption and emission of longwave radiation do not only depend on vegetation density but also on tree species. While detailed differentiation between species such as spruce and pine is not (yet) feasible in global climate models, individual global land models differentiate transmission of longwave radiation between PFTs, e.g. the interactions between the soil–biosphere–atmosphere (ISBA) land surface model within the EXternalized SURFace (SURFEX) model platform (*Boone et al.*, 2017). Improvements to SNOWPACK by *Gouttevin et al.* (2015) and this chapter focused mainly on the impact of radiation. However, *Bonan et al.* (2018) found turbulence parameterizations having a substantial impact on, among other variables, radiative temperature and reduced overestimation of diurnal ranges by implementing a roughness sublayer and subdividing the vegetation layer.

Systematic over- and underestimations of sub-canopy longwave radiation simulated by CLM4.5 across sites and vegetation types suggest that it may be possible to develop a correction to the parameterization of sub-canopy longwave radiation that depends on meteorological conditions. Improvements of SNOWPACK have shown that a two-layer canopy vegetation can reduce overestimated diurnal variations leading to asymmetric above-canopy and sub-canopy longwave radiation (*Gouttevin et al.*, 2015). However, mean biases are small compared to RMSE across all sites, apart from Seehornwald after including biomass heat storage. Simple scaling of diurnal cycles is likely to have little im-

pact on mean biases, as daytime overestimations and nighttime underestimations display similar magnitudes. Moreover, mean biases vary between sites and depend on evaluation periods, and sensitivity studies indicate forcing choices can turn net overestimations into net underestimations and vice versa. Consequently, the impact of simulation errors in sub-canopy longwave radiation on snowmelt in global simulations is uncertain and likely features substantial spatial variations. Implementation of biomass heat storage results in more realistic timing of diurnal cycles of sub-canopy longwave radiation, but the impact on mean biases is consistently positive increasing net overestimations. Moreover, the impact of biomass heat storage on diurnal ranges of sub-canopy longwave radiation is small, and biomass has to be substantially overestimated in order to correct these diurnal ranges. Generally, the single most important parameter for each vegetation type is vegetation density indicating its representation in climate models is crucial, as it determines the contribution from vegetation to sub-canopy longwave radiation, thereby scaling simulation errors, and exhibits an impact on the response of vegetation to meteorological forcing.

4.10 Conclusion

A model framework was created to facilitate the simulation of sub-canopy longwave radiation by CLM4.5 and SNOWPACK, a snow cover model with a more complex canopy representation, under equal conditions using forcing data from several boreal and montane forest stands with varying vegetation density and structure. Simulations by CLM4.5 display an overestimated diurnal range of sub-canopy longwave radiation and consequently an overestimated diurnal range in longwave enhancement by forest vegetation. Simulation errors for both of these quantities depend on vegetation density and meteorological conditions. Amplitudes of diurnal ranges for sub-canopy longwave radiation and longwave enhancement increase with decreasing effective emissivity of the sky, implying overestimated absorption of insolation and overestimated radiative cooling at night. In contrast, SNOWPACK featuring a two-layer vegetation canopy simulates smaller ranges of sub-canopy longwave radiation. Vegetation density determines the contribution from vegetation to sub-canopy longwave radiation thereby scaling simulation errors. Inclusion of a parameterization for biomass heat storage, guided by SNOWPACK, improves simulation of sub-canopy longwave radiation and longwave enhancement by CLM4.5 but does not substantially reduce diurnal ranges. This effect on sub-canopy longwave radiation is similar to the recent model development of SNOWPACK (*Gouttevin et al.*, 2015), in terms of both reduced RMSE and persistence of the overestimated diurnal range. The latter was corrected in SNOWPACK by partitioning vegetation into two layers, which may provide guidance for further improvements of CLM4.5.

5 Impact of deficient longwave enhancement on snow cover in global land-only simulations of CLM4.5

As described in Chapter 2.2.1, vegetation in the Community Land Model version 4.5 (CLM4.5) is parameterized as a single layer using a "big-leaf" approach. Evaluation of stand-scale simulations in Chapter 4 showed that CLM4.5 simulates overestimated diurnal cycles of sub-canopy longwave radiation and consequently of longwave enhancement, with simulation errors increasing with clearer skies. However, the consequent impact on large-scale snow cover and snowmelt has not been assessed yet, neither so far in this thesis nor in the literature, resulting in Research Question 2: **What impact do potential deficiencies in simulated longwave enhancement have on snow cover across the Northern Hemisphere?**

In this chapter, a correction is developed in order to reduce unphysical diurnal variations in sub-canopy longwave radiation, which is based on the systematic dependence of simulation errors on meteorological conditions found in Chapter 4. Subsequently, this correction is implemented in global offline simulations of CLM4.5 to assess the impact of deficient simulation of longwave enhancement on snow cover, and a brief outlook is given on the effect of this correction in global coupled simulations. A shortened version of this chapter, which only focuses on offline simulations, has been accepted for review as *Simulated single-layer forest canopies delay Northern Hemisphere snowmelt* in The Cryosphere Discussions (*Todt et al.*, 2019).

5.1 Methodology

5.1.1 Correction of sub-canopy longwave radiation in CLM4.5

A correction factor f_{corr} is implemented in CLM4.5 to reduce the overestimated diurnal cycle of sub-canopy longwave radiation. Modelling of sub-canopy longwave radiation in CLM4.5 is described in Chapter 2.2.1, and sub-canopy longwave radiation is calculated as the sum of atmospheric longwave radiation LW_{atm} and longwave radiation emitted by vegetation LW_{veg}, weighted by vegetation emissivity ε_v (Equation (2.6)). As atmospheric longwave radiation is an input variable to CLM4.5, from either forcing datasets or the atmospheric model component, correction factors are used to scale longwave radiation emitted from vegetation:

$$LW_{sub} \;=\; (1-\varepsilon_v)\; LW_{atm} \;+\; \varepsilon_v\; \sigma\; T_v^4\; f_{corr}. \tag{5.1}$$

Conceptually, correction factors represent a vegetation consisting of multiple individual layers, so that longwave radiation fluxes emitted upward and downward from the veg-

etation are no longer equal by design. In a multi-layer canopy scheme, the uppermost layer contributes most to longwave radiation emitted upward and is directly exposed to atmospheric forcing. Conversely, the lowest layer contributes most to longwave radiation emitted downward, but is shaded and sheltered by canopy layers above.
Using multi-layer canopy schemes as a guideline, longwave radiation is redistributed in CLM4.5 resulting in asymmetrical upward and downward longwave radiation fluxes and consequently, above-canopy longwave radiation is calculated as

$$\begin{aligned} LW_{above} &= (1-\varepsilon_v)\,(1-\varepsilon_g)\,(1-\varepsilon_v)\,LW_{atm} \\ &+ \varepsilon_v \left((2-f_{corr}) + (1-\varepsilon_v)\,(1-\varepsilon_g)\,f_{corr}\right)\sigma\,T_v^4 \\ &+ (1-\varepsilon_v)\,\varepsilon_g\,\sigma\,T_{surf}^4 \end{aligned} \tag{5.2}$$

with emissivity of the ground ε_g and ground surface temperature T_{surf}. In Equation (5.2), the first term represents atmospheric longwave radiation transmitted through the vegetation, reflected by the ground, and transmitted through the vegetation to the atmosphere; the second term represents longwave radiation emitted from the vegetation reaching the atmosphere; and the third term represents longwave radiation emitted by the ground and transmitted through the vegetation to the atmosphere. The second term combines longwave radiation emitted by the vegetation directly to the atmosphere (first term in parentheses) and longwave radiation emitted downward from the vegetation, reflected by the ground, and transmitted through the vegetation to the atmosphere (second term in parentheses). For $f_{corr} > 1$, LW_{above} decreases as reduction in the first term in parentheses $(2 - f_{corr})$ outweighs increase in the second term in parentheses $(1-\varepsilon_v)\,(1-\varepsilon_g)\,f_{corr}$, while LW_{sub} in Equation (5.1) increases. For $f_{corr} < 1$, LW_{sub} decreases and LW_{above} increases. Note that the sum of LW_{sub} and LW_{above} is not changed by the introduction of f_{corr}, which guarantees conservation of energy. The calculation of vegetation temperature in CLM4.5 is not altered by this approach and consequently, the temperature of the single vegetation layer represents an average of multiple (theoretical) layers that are suggested by asymmetrical upward and downward longwave radiation fluxes.

5.1.2 Global offline simulations with CLM4.5

Offline, i.e. land-only, simulations were chosen for assessment of the impact of corrected longwave enhancement on snow cover, as these allow for focusing on a particular process due to the one-way interaction between atmosphere and land model. Offline simulations of CLM4.5 were forced by prescribed atmospheric data using the CRUNCEP version 7 data set, which covers 1981 to 2016 and thus snow seasons 1981/82 to 2015/16 (*Viovy*, 2018). A simulation grid size of roughly 1° (latitudinal resolution of 0.9°, longitudi-

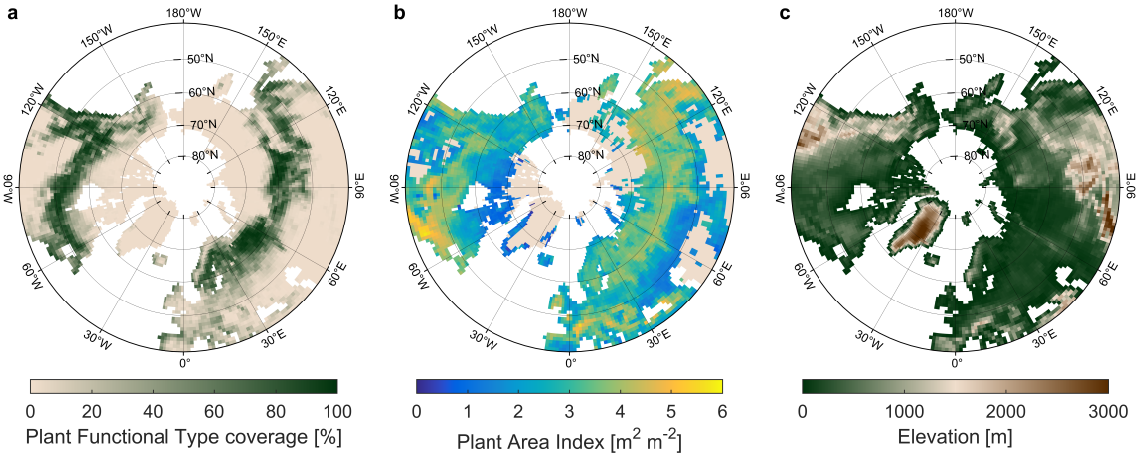

Figure 5.1: Coverage of vegetated landunit within grid cell by combination of Needleleaf Evergreen Boreal Trees (NEBTs) and Needleleaf Evergreen Temperate Trees (NETTs) (**a**), plant area index (PAI) for combination of NEBTS and NETTs weighted by their fractional coverage (**b**), and grid-cell average elevation (**c**) based on CLM4.5's $0.9° \times 1.25°$ surface dataset that was used for global simulations.

nal resolution of 1.25°) was chosen in order to balance spatial resolution and computational costs. The impact of correction factors on longwave enhancement, snow cover, and snowmelt is assessed by comparing two simulations, a control run (henceforth, CTRL) and a run in which correction factors were implemented (henceforth, CORR). Correction factors were applied to evergreen needleleaf trees in CLM4.5 as given in Equations (5.1) and (5.2). Two plant functional types (PFTs), Needleleaf Evergreen Boreal Trees (NEBTs) and Needleleaf Evergreen Temperate Trees (NETTs), represent evergreen forests across snow-covered areas in CLM4.5 and grid-cell coverage by these two PFTs is shown in Figure 5.1a. Plant area index (PAI), the sum of leaf area index (LAI) and stem area index (SAI), is shown in Figure 5.1b as a weighted average of NEBTs and NETTs.

5.2 Calculation of correction factors

A "toy model" was created in Chapter 4, which utilized forest stand-scale forcing data to evaluate sub-canopy longwave radiation in CLM4.5 and revealed systematic simulation errors that depend on meteorological conditions. These meteorological conditions were categorized via insolation and cloudiness represented by effective emissivity of the sky ε_{sky}, which is described in Chapter 2.1 and calculated as outlined in Equation (2.4). In this chapter, correction of sub-canopy longwave radiation is created based on those stand-scale simulations for forest stands near Abisko, Alptal, Cherskiy, Seehornwald, and Sodankylä, which are described in Chapter 3 and whose characteristics are listed in Tables 3.1 and 4.1. The forest stand near Yakutsk was not considered for this analysis, as only nighttime

measurements were reliable. Also, the forest stand near Borden was not considered for this analysis, as its mixed vegetation would introduce additional uncertainty to the derived correction. Correction factor f_{corr} as used in Equation (5.1) was calculated from ε_{sky} and insolation SW_{in} as

$$f_{corr}^{-1} = b_0 + b_1\,\varepsilon_{sky} + b_2\,SW_{in} + b_3\,SW_{in}\,\varepsilon_{sky}. \tag{5.3}$$

Coefficients $b_{0,\ldots,3}$ relate to intercept, ε_{sky}, insolation, and interaction of ε_{sky} and insolation, respectively, and were calculated via multiple linear regression from stand-scale simulation errors expressed as ratios (Figure 5.2) and observations of ε_{sky} and insolation at forest stands. Subsequently, correction factors were calculated as inverses of these ratios in order to scale longwave radiation in CLM4.5. For example, if stand-scale simulations revealed an overestimation of longwave radiation by 25% for particular values of ε_{sky} and SW_{in}, correction factors in global simulations would be $1.25^{-1} = 0.8$ for the same meteorological conditions. As CLM4.5 only simulates longwave radiation emitted from vegetation, simulation errors were calculated for LW_{veg} that was derived from sub-canopy longwave radiation via Equations (2.5) and (2.6) using measurements of atmospheric longwave radiation and PAI, which is given in Tables 3.1 and 4.1. Error ratios as a function of ε_{sky} and insolation as well as estimates based on regression coefficients are shown in Figure 5.2. Nighttime estimates are a linear function of ε_{sky} as insolation is zero, while daytime estimates involve interaction of effective emissivity of the sky and insolation. Both daytime and nighttime simulation errors generally increase in magnitude with clearer skies. However, insolation is necessary in addition to ε_{sky} in order to determine daytime regression slopes.

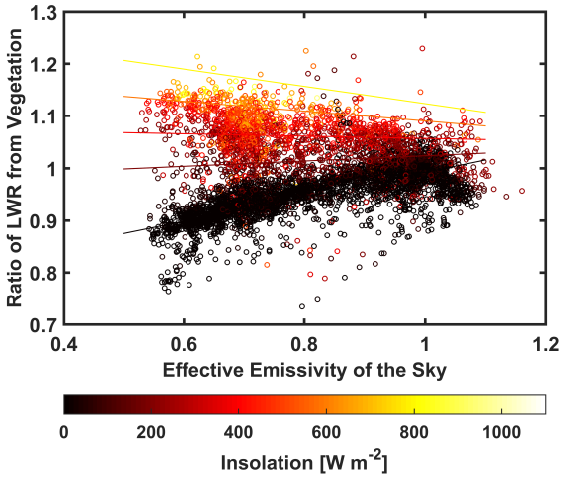

Figure 5.2: Ratio of longwave radiation emitted from vegetation simulated by CLM4.5 and estimated from forest stand observations as a function of effective emissivity of the sky ε_{sky} (abscissa) and insolation (colour) for Alptal (season 2005), Seehornwald (2009), Sodankylä, and Cherskiy. Lines represent solutions of Equation (5.3) for multiple values of insolation: 0, 200, 400, 600, and 800 Wm^{-2}.

Regression coefficients as outlined in Equation (5.3) are shown in Figure 5.3 for every site and season, differentiated for day and night. Intercept b_0 and regression coefficient

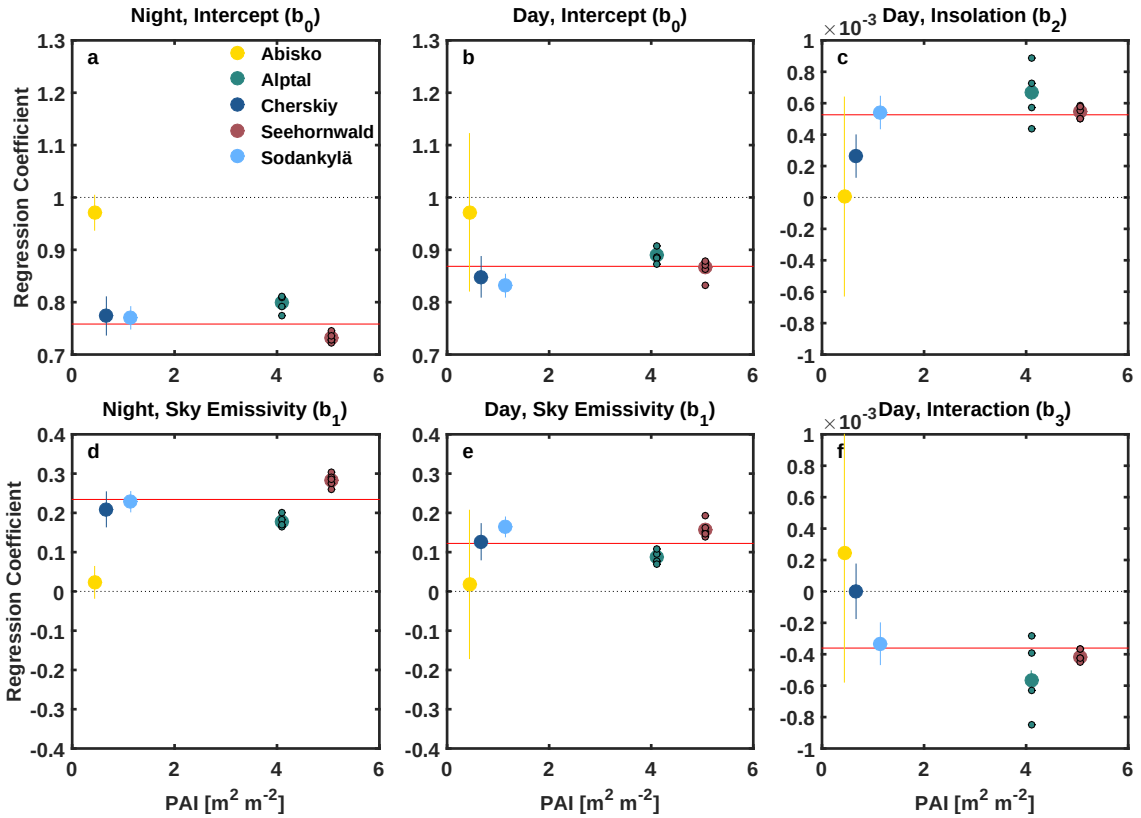

Figure 5.3: Regression coefficients (Equation (5.3)) for forest stands at Abisko (yellow), Alptal (green), Cherskiy (dark blue), Seehornwald (maroon), and Sodankylä (light blue) with small circles indicating individual seasons for Alptal and Seehornwald and solid lines indicating 95%-confidence intervals. Red lines display regression coefficients calculated from a combination of Alptal season 2005, Cherskiy, Seehornwald season 2009, and Sodankylä. Intercept b_0 and regression coefficient for ε_{sky} b_1 are differentiated for night (**a** and **d**, respectively) and day (**b** and **e**, respectively). Regression coefficient for insolation b_2 and regression coefficient for interaction of ε_{sky} and insolation b_3 are shown for day only (**c** and **f**, respectively). Regression coefficients involving insolation have the unit $\mathrm{W}^{-1}\mathrm{m}^2$.

for ε_{sky} b_1 agree in sign for all sites and agree in magnitude for all sites except Abisko (panels a, b, d, e). Both b_0 and b_1 display little interannual variability for the two sites with multiple years of data, Alptal and Seehornwald, which can be seen for day and night. In contrast to Abisko, b_0 and b_1 for the deciduous forest at Cherskiy are similar to those for evergreen sites Alptal, Seehornwald, and Sodankylä despite featuring different vegetation type, structure, and density. Regression coefficients involving insolation agree in sign but differ in magnitude among Alptal, Cherskiy, Seehornwald, and Sodankylä (panels c and f), with similar values for the latter two sites due to little interannual variability for Seehornwald. In contrast, interannual variability is large for Alptal with higher magnitudes for all four years combined compared to Seehornwald and Sodankylä, while

Table 5.1: Regression coefficients as implemented in simulation CORR in order to calculate correction factors and as shown as red lines in Figure 5.3. Regression coefficients involving insolation have the unit $\mathrm{W}^{-1}\mathrm{m}^2$.

Regression Coefficient	**Day**	**Night**
b_0 – intercept	0.8685	0.7582
b_1 – ε_{sky}	0.1223	0.2342
b_2 – insolation	$5.2627\ 10^{-4}$	–
b_3 – interaction	$-3.6065\ 10^{-4}$	–

magnitudes are smallest for Cherskiy. For Abisko, five out of six regression coefficients display smallest magnitudes, which is due to deciduous vegetation and consequently low vegetation density as well as smaller simulation errors compared to other sites (see Chapter 4). Overall, uncertainties are largest for Abisko due to a short evaluation period, with no regression coefficient being significantly different from one, as in the case of intercept b_0, or zero.

For implementation in global simulation CORR, regression coefficients were calculated based on one season each of Alptal, Cherskiy, Seehornwald, and Sodankylä in order to balance dense and sparser sites. Despite featuring a deciduous PFT, Cherskiy was included as regression coefficients are similar to evergreen sites. Individual seasons for Alptal, 2005, and Seehornwald, 2009, were chosen based on similarity of regression coefficients to those for all years combined of the respective site. Regression coefficients for these four sites combined are shown as red lines in Figure 5.3 and listed in Table 5.1. Estimates of simulation errors based on these regression coefficients are shown in Figure 5.2 and explain 60% of variance in nighttime errors and 59% of variance in daytime errors.

5.3 Effect of correction in offline simulations of CLM4.5

5.3.1 Sub-canopy longwave radiation – case study Alptal, Switzerland

In contrast to other forest stands used to estimate regression coefficients, grid cell and forest stand feature similarly high vegetation densities (PAIs of 3.7 $\mathrm{m}^2\mathrm{m}^{-2}$ and 4.1 $\mathrm{m}^2\mathrm{m}^{-2}$, respectively) and thus similar vegetation emissivities ε_v (0.975 and 0.983, respectively) for the location of Alptal. This allows for a comparison of diurnal cycles of sub-canopy longwave radiation as well as longwave enhancement between offline simulations and stand-scale measurements. Implementation of correction factors in CLM4.5 results in decreased sub-canopy longwave radiation during day and increased sub-canopy longwave

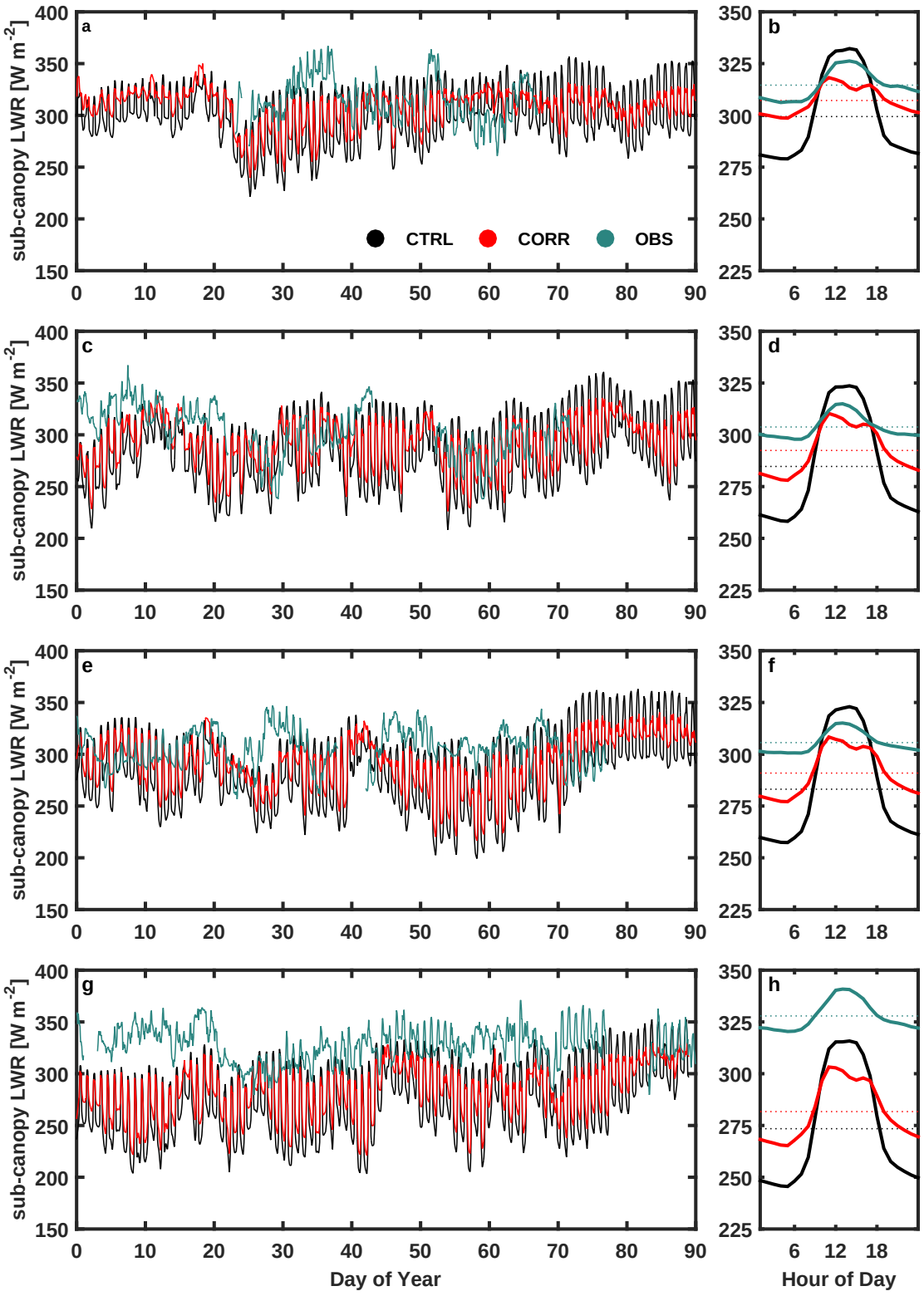

Figure 5.4: Hourly time series (**a**, **c**, **e**, **g**), diurnal cycles (solid in **b**, **d**, **f**, **h**), and JFM averages (dotted in **b**, **d**, **f**, **h**) of sub-canopy longwave radiation for the snowmelt seasons in 2004 (**a**, **b**), 2005 (**c**, **d**), 2006 (**e**, **f**), and 2007 (**g**, **h**) at the forest stand of Alptal, Switzerland. Measurements at the forest stand (green) are shown for comparison with offline simulations CTRL (black) and CORR (red) for boreal evergreen needleleaf trees in the corresponding grid cell of Alptal. Gaps in measurements are due to quality checks and excluded from calculation of diurnal cycle and JFM average.

radiation during night, thereby reducing diurnal cycles. For the grid cell representing Alptal, simulated diurnal ranges decrease from about 70 Wm^{-2} to about 30 Wm^{-2}, while observations at the forest stand show an average diurnal range of about 20 Wm^{-2} (Figure 5.4). Correction factors reducing diurnal ranges of sub-canopy longwave radiation as well as smaller observed diurnal cycles are consistent across all four years, for which measurements are available at the forest stand. However, diurnal cycles and seasonal averages of sub-canopy longwave radiation simulated by CLM4.5 display less interannual variation than measurements at the forest stand. Asymmetric diurnal cycles of corrected simulated sub-canopy longwave radiation are due to asymmetric diurnal cycles of insolation that consistently exhibit higher insolation values in the afternoon, which lead to more substantial correction. Moreover, diurnal cycles of corrected simulated sub-canopy longwave radiation show a slight dip around the time of maximum insolation due to the impact of insolation on correction factors. However, this dip is small compared to the reduction of diurnal ranges. Simulations and observations display a similar range of intraseasonal variability but do not agree in evolution and daily average of sub-canopy longwave radiation. Implementation of correction factors increases average sub-canopy longwave radiation, seen in Figure 5.4, for two reasons. Firstly, daytime correction depends on insolation, which changes throughout the snow cover season so that daytime correction varies to a higher degree than nighttime correction. Secondly, nights are longer than days prior to the boreal spring equinox, which leads to nighttime increases outweighing daytime decreases. Consequently, correction results in increased average sub-canopy longwave radiation even for equal magnitudes of daytime overestimation and nighttime underestimation.

Comparison of simulated and measured longwave enhancement is shown in Figure 5.5 for Alptal. As for sub-canopy longwave radiation, the diurnal cycle of simulated longwave enhancement is reduced by implementation of correction factors with increased enhancement at night and decreased enhancement at daytime. Reduction of daytime longwave enhancement increases throughout the snowmelt season, which is due to increasing insolation and consequently increasing reduction of sub-canopy longwave radiation during the day. Longwave enhancement values vary between 1.1 and 1.4 in CTRL, predominately due to the overestimated diurnal cycle. The diurnal cycle of longwave enhancement is reduced by more than 50% in CORR, resulting in a diurnal range similar to observations and in increased daily average longwave enhancement. Simulated longwave enhancement displays little intraseasonal variability with variations being largely driven by repetitions of diurnal cycles. This indicates intraseasonal variability in sub-canopy longwave radiation is largely due to variations in atmospheric longwave radiation, while longwave

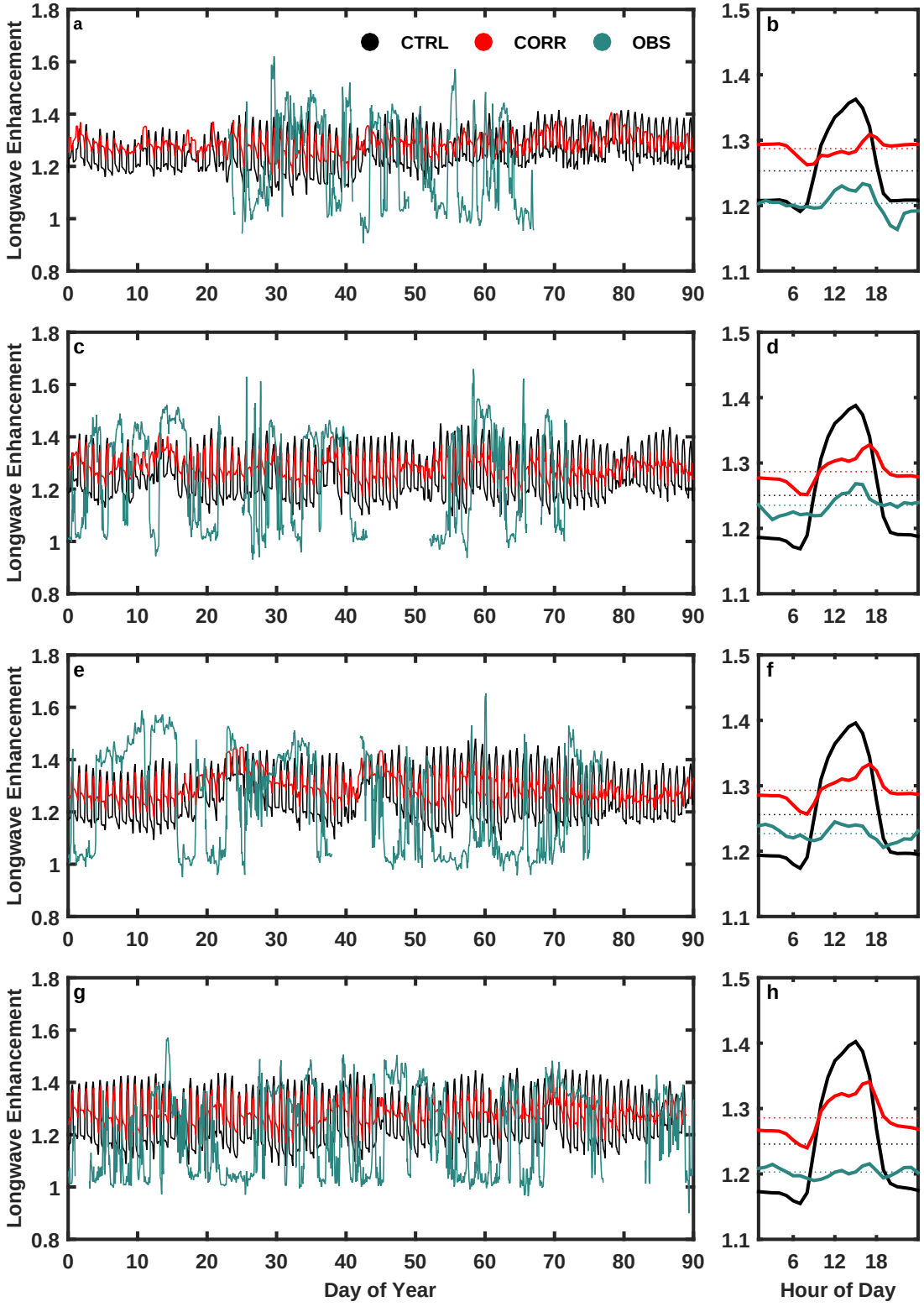

Figure 5.5: Hourly time series (**a**, **c**, **e**, **g**), diurnal cycles (solid in **b**, **d**, **f**, **h**), and JFM averages (dotted in **b**, **d**, **f**, **h**) of longwave enhancement for the snowmelt seasons in 2004 (**a**, **b**), 2005 (**c**, **d**), 2006 (**e**, **f**), and 2007 (**g**, **h**) at the forest stand of Alptal, Switzerland. Measurements at the forest stand (green) are shown for comparison with offline simulations CTRL (black) and CORR (red) for boreal evergreen needleleaf trees in the corresponding grid cell of Alptal. Gaps in measurements are due to quality checks and excluded from calculation of diurnal cycle and JFM average.

enhancement by vegetation only adds diurnal variability. In contrast, measured longwave enhancement values range from less than 1 to more than 1.6 and display little diurnal variability but high variability on synoptic timescales throughout the snowmelt season. Moreover, simulated longwave enhancement displays little interannual variability in contrast to observations, further highlighting the lack of variability in meteorological conditions as these determine the magnitude of longwave enhancement (see Chapter 2.1). This lack of meteorological variability results in a difference of daily average longwave enhancement between simulations and observations. Lower average longwave enhancement for observations indicates more overcast conditions, which lead to smaller diurnal cycles in sub-canopy longwave radiation compared to simulations. Therefore, correction factors improve the realism of diurnal cycles of sub-canopy longwave radiation and longwave enhancement, encouraging usage for evaluation of impact on snow cover.

The contrast in variability between simulated and observed longwave enhancement can be seen in Figure 5.6. Observations show a large range of longwave enhancement values that are closely tied to effective emissivity of the sky, which represents clear-sky (low ε_{sky}) and overcast (high ε_{sky}) conditions. Observed longwave enhancement increases for decreasing ε_{sky} as the contrast between vegetation temperatures, increasing due to higher insolation, and radiative temperature of the sky increases. Spread in observed longwave enhancement is small throughout the range of ε_{sky}, indicating little diurnal variability and the process of longwave enhancement depending on meteorological conditions. Offline simulations display a narrow range of ε_{sky}, which causes the lack of intraseasonal and interannual variability seen in Figure 5.5. The spread in simulated longwave enhancement values is substantially larger compared to observations for the respective range in ε_{sky} representing overestimated diurnal cycles. Implementation of correction factors reduces the spread in long-

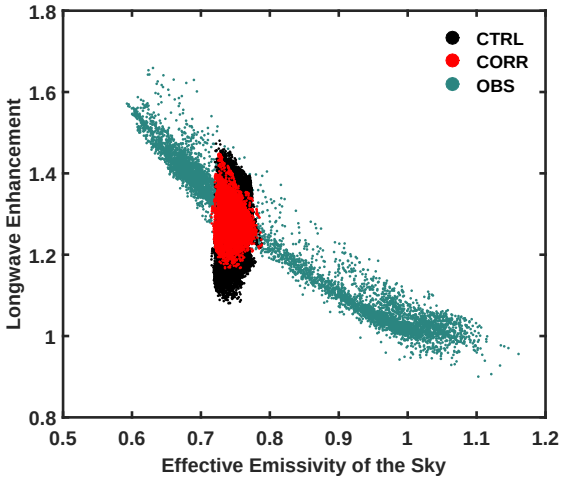

Figure 5.6: Longwave enhancement measured (green) at the forest stand of Alptal, Switzerland and simulated in CTRL (black) and CORR (red) for boreal evergreen needleleaf trees in the corresponding gridcell of Alptal, Switzerland as a function of effective emissivity of the sky. Each data point represents an hourly average seen in Figure 5.5.

wave enhancement values and increases average longwave enhancement (see Figure 5.5), however, spread in longwave enhancement is still overestimated and average longwave enhancement is underestimated in CORR compared to observations for the respective range in ε_{sky}.

5.3.2 Longwave enhancement and limited spatial variability in ε_{sky}

Offline simulations feature a lack of variability in ε_{sky}, as seen for the grid cell of Alptal, across the Northern Hemisphere, which results in correction factors being similar spatially and largely dependent on insolation. However, variability in both insolation and diurnal ranges in atmospheric longwave radiation indicate small variations in meteorological forcing that are not represented by ε_{sky}. Therefore, ε_{sky} in offline simulations may indicate clear-sky conditions even when insolation and atmospheric longwave radiation suggest more overcast conditions, resulting in overestimated correction factors and overcorrection of sub-canopy longwave radiation. This overcorrection results in larger nighttime than daytime values of sub-canopy longwave radiation in contrast to atmospheric longwave radiation and occurs mostly along continental coasts (Figure 5.7). One-way coupling between atmosphere and land in offline simulations limits the impact of overcorrection carrying over to other grid cells and consequently, a contour line is shown in maps depicting the effect of correction factors in order to denote an overcorrection for 10% of days.

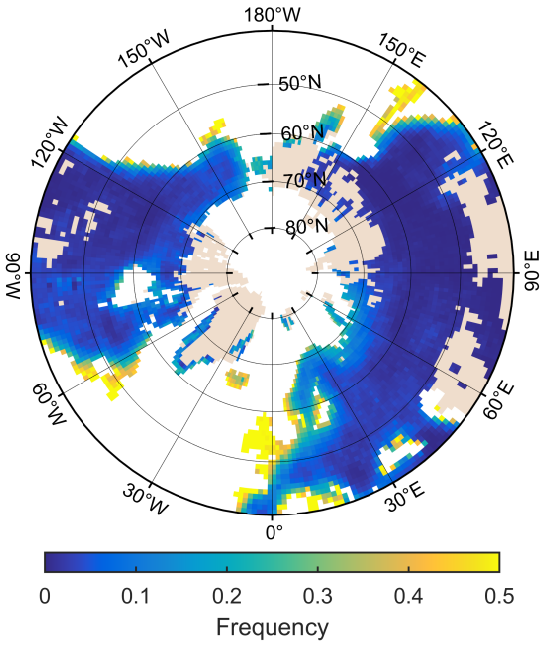

Figure 5.7: Frequency of days for 2004 - 2007 during which implementation of correction factors results in higher nighttime than daytime sub-canopy longwave radiation despite higher daytime than nighttime atmospheric longwave radiation.

Maps of longwave enhancement beneath evergreen needleleaf forests in CLM4.5 are shown in Figures 5.8a and 5.8b. For CTRL, averages over boreal winter and spring show an enhancement of longwave radiation beneath canopies by about 20% to 30% and display little differences across boreal forests, which is due to small spatial variability in both ε_{sky} and vegetation density (Figure 5.1). As shown for the grid cell of Alptal, intraseasonal

and interannual variability in ε_{sky} is small and consequently, overestimated diurnal cycles determine variability in longwave enhancement across boreal forests. CORR displays increased average longwave enhancement north of $40°\mathrm{N}$ with an additional enhancement of longwave radiation of up to 5% beneath dense boreal forests, which indicates a general underestimation by CLM4.5. Changes in longwave enhancement generally increase with latitude as daytime correction factors vary with insolation while nighttime correction factors are independent of latitude. A higher increase in longwave enhancement can be seen for higher vegetation density within regions covered by boreal forests (Figure 5.1b), which is due to weighing of contributions to subcanopy longwave radiation (Equation (5.1)).

5.3.3 Snow cover and snowmelt

Changes in sub-canopy longwave radiation affect the surface energy balance, which can be seen for grid cell-averaged snow surface temperature (Figures 5.8c and 5.8d). Simulated average snow surface temperatures are determined by latitude, topography, and continentality, reaching values of less than -40$°\mathrm{C}$ in the mountainous regions of northeastern Siberia (Figure 5.1c), and range between -20$°\mathrm{C}$ and -15$°\mathrm{C}$ for boreal forests, the outlines of which can be seen in central Siberia and central North America. The impact of correction factors is limited to grid cells for which vegetation is dominated by evergreen needleleaf trees, and implementation results in an increase in average snow surface temperature of up to $2°\mathrm{C}$. The lack of spatial variability in change due to correction factors is caused by little spatial variability in meteorological conditions as well as high vegetation density and similarly high PFT coverage across boreal forests (Figures 5.1a and 5.1b).
Cold content, the energy required to raise snow temperatures to $0°\mathrm{C}$, is used to quantify the impact of correction factors on the entire snow column. Average cold content simulated by CLM4.5 mostly reaches values of up to 4 MJm^{-2} and exceeds 5 MJm^{-2} only in glaciated grid cells (Figure 5.8e). In CTRL, simulated average cold content ranges between 1.5 MJm^{-2} and 3 MJm^{-2} across boreal forests, with lowest values in northeastern Europe and highest values in eastern Siberia, western Canada, and Quebec. Relative changes in cold content from CTRL to CORR display spatial differences with cold content generally decreasing across boreal forests (Figure 5.8f). Reductions in average cold content reach up to 30% in northeastern Europe and western North America and up to 20% in central North America. Across Siberian boreal forests, relative reductions decrease from west to east from more than 20% to about 10%. Spatial differences in relative reductions correspond to spatial differences in average cold content, with higher relative reductions for smaller averages, representing a more even spatial pattern of absolute reductions in cold content as indicated by changes in snow surface temperature (Figure 5.8d).

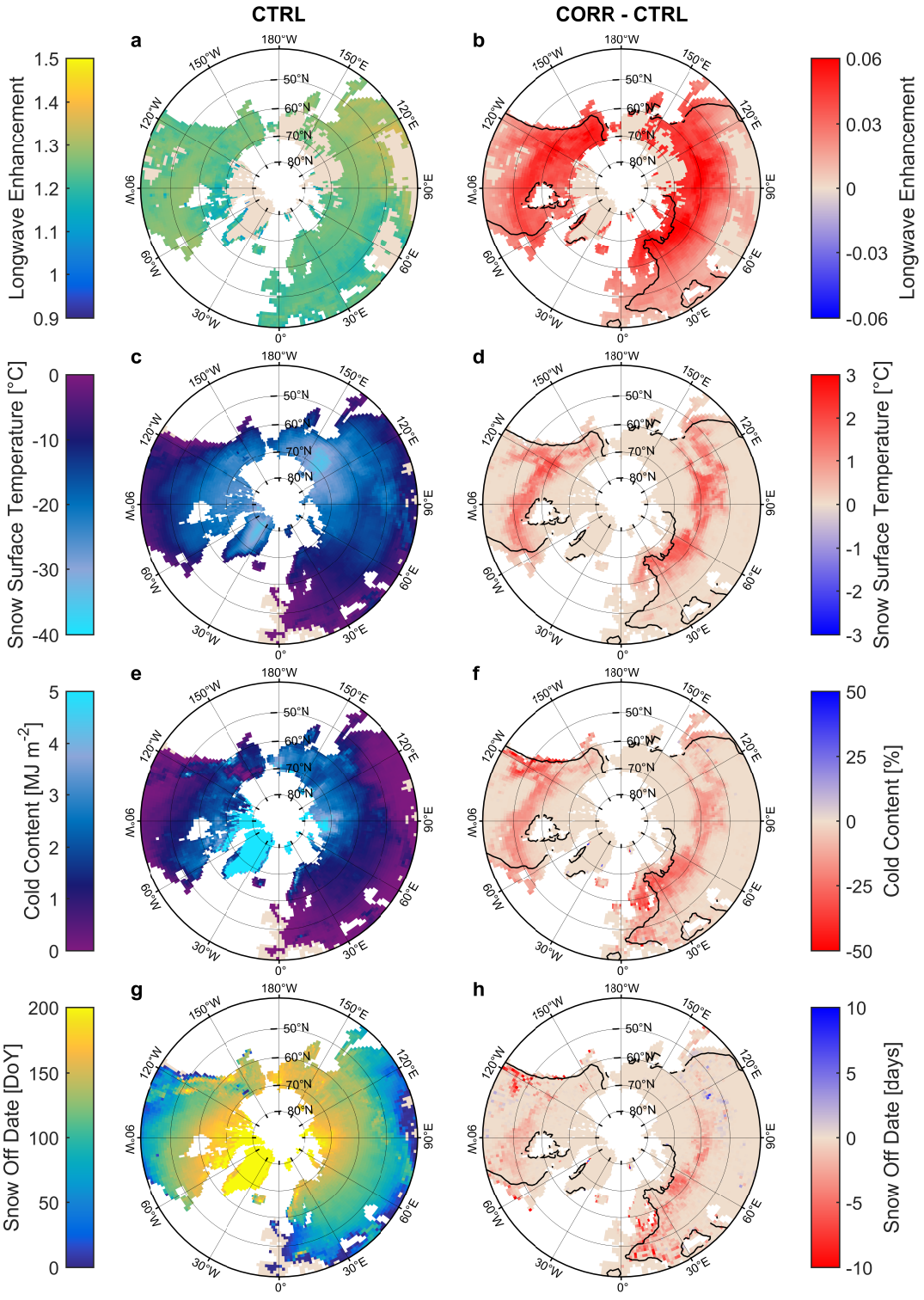

Figure 5.8: Averages in CTRL (**a**, **c**, **e**, **g**) and differences between CORR and CTRL (**b**, **d**, **f**, **h**) for longwave enhancement beneath evergreen needleleaf trees (**a**, **b**), snow surface temperature (**c**, **d**), cold content (**e**, **f**), and snow off date (**g**, **h**). Longwave enhancement is averaged over December to May while snow surface temperature and cold content are averaged over entire snow cover seasons. Differences CORR - CTRL are calculated as averages of differences between each individual snow cover season. For panels **c**-**h**, a mask is applied to filter out grid cells that are not perennially snow-covered. Black lines demarcate continental areas with less than 10% of overcorrected days.

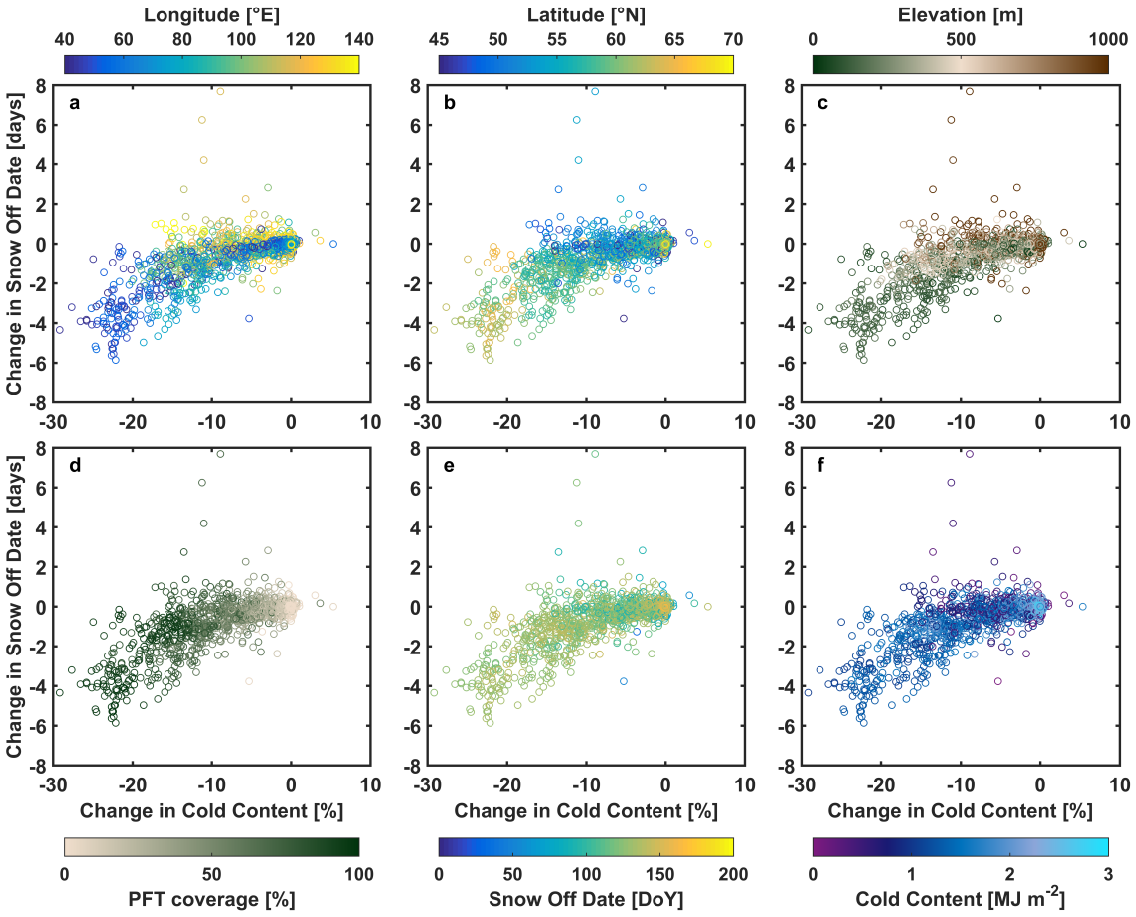

Figure 5.9: Change in cold content and snow off date from CTRL to CORR as a function of longitude (**a**), latitude (**b**), elevation (**c**), coverage by evergreen needleleaf trees (**d**), snow off date in CTRL (**e**), and cold content in CTRL (**f**) for grid cells within the area 40°E to 140°E and 42°N to 70°N.

Spatial patterns in snow off date are similar to those in cold content as higher cold content corresponds to later meltout (Figures 5.8g and 5.8h). Snow off dates across evergreen needleleaf forests generally occur earlier in CORR compared to CTRL, but changes due to correction display stark spatial contrasts. Meltout happens up to 10 days earlier in central Europe and on the western coast of North America. Meltout is advanced by about 5 days for boreal forests in northeastern Europe and western Siberia and slightly less for boreal forests in central North America. In contrast, meltout is delayed in mountains of southeastern Siberia (see elevation in Figure 5.1c), where meltout occurs late among boreal forests.

Reasons for spatial differences in changes of meltout across Siberian boreal forests are explored in Figure 5.9, which shows a clear contrast in the effect of correction on cold content and snow off date between northwestern Siberia and southeastern Siberia (panels a and b). Snow off dates in CTRL and coverage by evergreen needleleaf trees are

similar for northwestern and southeastern Siberia, so that snow cover in each grid cell is exposed to changes in sub-canopy longwave radiation to the same extent and for roughly the same duration (panels d and e). Spatially similar snow off dates in CTRL, despite differences in cold content, are likely caused by higher elevations in southeastern Siberia compensating for less cold content, and meltout generally occurs past the boreal spring equinox in northwestern and southeastern Siberia (panels c, e, and f). However, higher insolation for southeastern Siberia results in higher reductions of daytime sub-canopy longwave radiation by correction factors and consequently smaller increases in daily average sub-canopy longwave radiation prior to the boreal spring equinox compared to northwestern Siberia. Although changes in sub-canopy longwave radiation are still positive in southeastern Siberia when accumulated over the entire snow season, causing a decrease in cold content, reduction in daily average sub-canopy longwave radiation by correction factors past the boreal spring equinox counteracts the previous increase and consequently, snowmelt is slightly delayed. In contrast to southeastern Siberia, meltout is slightly accelerated in central North America although both latitude and meltout date are similar, as relative reductions in cold content are generally higher. However, differences in changes in meltout date between central North America and southeastern Siberia are minor. Across Europe, latitude and meltout date are more important than reductions in cold content for acceleration of meltout. Highest relative reductions in cold content can be seen for northeastern Europe but result in little to no change in meltout date (Figures 5.8f and 5.8h), which occurs on average in late April and early May. Relative reductions in cold content are smaller in central Europe but lead to acceleration of already early meltout dates by 5 to 10 days, despite coverage by PFTs being less than in northeastern Europe (Figure 5.1a).

5.4 Discussion

Correction factors were estimated by multiple linear regression based on two meteorological parameters, insolation and effective emissivity of the sky, which represents a measure of cloudiness. These two variables explain 60% of the variance in simulation errors and, although there is variability that is not captured, evident in variations of nighttime simulation errors (Figure 5.2), no other major impacting parameter or variable could be found to include in regression. Correction factors and consequently the precise impact of correction on snow cover and snowmelt depend on the choice of data used to calculate correction factors. Especially for daytime, choosing to omit or include a particular forest stand changes correction factors and thereby reduction of daytime sub-canopy longwave radiation. Stand-scale simulations for the four forest stands near Alptal, Cherskiy, Seehornwald, and Sodankylä were chosen for calculation of correction factors in order

to balance high-density and low-density vegetation. As seen in Chapter 4, sub-canopy longwave radiation simulated by CLM4.5 displays similar errors for the forest stand near Cherskiy compared to evergreen forest stands despite differences in vegetation characteristics, which is reflected in regression coefficients b_0 and b_1. However, regression coefficients involving insolation differ between evergreen forest stands, Cherskiy, and Abisko. This might suggest that the particular vegetation structure at the forest stand near Cherskiy shelters lower vegetation parts similarly to evergreen forests, due to its high tree density, but does not shade itself to the same degree, as larch trees are deciduous. Nevertheless, slight changes in correction factors do not change systematic daytime decrease and nighttime increase, and weighing by durations of day and night is independent of correction factors. Insolation and cloudiness being the primary governing variables indicates the shading and sheltering effect of a multi-layer canopy and its consequent damping of variations in sub-canopy longwave radiation, which was emphasized by *Gouttevin et al.* (2015). Therefore, the correction that is used in this chapter presents a simple approximation of the effect of a multi-layer canopy.

Comparison of stand-scale observations and offline simulations for the example of Alptal shows that CLM4.5 simulates a diurnal range of sub-canopy longwave radiation about 2.5 to 3.5 times larger than observations (across four years of observations at Alptal). Implementation of correction factors roughly divides the range of the diurnal cycle in half, and the resulting diurnal range is similar to observations when considering differences in meteorological conditions. On a seasonal and global scale, the impact of simulation errors on average daily sub-canopy longwave radiation is more important than the overestimated diurnal range. For Alptal, implementation of correction factors results in an increase of daily average sub-canopy longwave radiation by about 5 Wm^{-2} over the period January to March, which is the equivalent of 1.3 mm of snow water equivalent melting over a day or 20cm of snow water equivalent being warmed by 1 K over a day. This net increase is due to longer nights than days prior to the equinox at the end of March so that sub-canopy longwave radiation is increased by correction factors more during night than decreased during day. In Chapter 4, daytime overestimations and nighttime underestimations of sub-canopy longwave radiation in CLM4.5 were found to have roughly similar magnitudes. However, analysis in this chapter shows that different durations of day and night over the snow cover season result in a net underestimation of daily averages of sub-canopy longwave radiation by CLM4.5.

Observations and offline simulations of CLM4.5 show a similar range in sub-canopy longwave radiation at Alptal, however, origins of this similar range are contrary. Observations show that a large range in longwave enhancement compensates for large variability in

atmospheric longwave radiation, so that variability in sub-canopy longwave radiation is damped. Offline simulations exhibit little variability in meteorological forcing, both spatially and temporally, which results in little variabilty in longwave enhancement and consequently little variability in sub-canopy longwave radiation; the single-layer vegetation in CLM4.5 passes on the atmospheric signal while additionally enhancing diurnal variability. In fact, offline simulations display temporal variability in sub-canopy longwave radiation predominately on diurnal time scales rather than synoptic time scales, which contrasts observations.

The lack of variability in meteorological conditions seen at the grid-cell level is present over the Northern Hemisphere, which results in spatially uniform increases in longwave enhancement and snow surface temperatures due to correction. However, consistent impact on snow temperatures does not translate to consistent changes in meltout. Correction factors change throughout the snowmelt season due to increasing insolation and length of day. Consequently, net impact on daily averages of sub-canopy longwave radiation varies, which results in spatial differences in impact on cold content over the snow cover season and meltout date. Net increase in sub-canopy longwave radiation during the snow cover season is highest for regions of early snowmelt, where snow is already comparatively warm, which results in accelerated snowmelt. *Lundquist et al.* (2013) showed that forests enhance snowmelt compared to open area in regions where winters are warm and mid-winter melt events happen, during which longwave enhancement outweighs shading. Spatial differences in change of meltout date broadly agree with this pattern as the highest acceleration of melt occurs for regions of warmer winters as indicated by snow surface temperatures (Figure 5.8c), suggesting that mid-winter melt events could be underestimated by CLM4.5. Conversely, correction of sub-canopy longwave radiation results in slightly delayed snowmelt in southeastern Siberia albeit average cold content over the entire snow cover season being reduced. This delay is due to meltout happening substantially later than the boreal spring equinox and high insolation during the snowmelt period, which result in reduction in daytime sub-canopy longwave radiation outweighing increased sub-canopy longwave radiation during night. Consequently, overestimated diurnal cycles of sub-canopy longwave radiation in CLM4.5 lead to a compressed snowmelt duration across boreal forests in offline simulations.

Comparison of offline simulations of CLM4 with observations have shown CLM4 failing to accurately simulate the timing of both snow ablation and snow accumulation across boreal forests (*Thackeray et al.*, 2014, 2015). Observations show one major peak in reduction of Snow Cover Fraction (SCF) across boreal forests, from April to May, and smaller reductions in SCF in early and late spring. In contrast, CLM4 simulates major

reductions in SCF from March to April and April to May but underestimates reductions from February to March and May to June, indicating snowmelt duration is compressed into the period March to May. Correction of overestimated diurnal cycles of sub-canopy longwave radiation might thus help to expand snowmelt duration across boreal forests by accelerating early snowmelt and delaying late snowmelt. *Thackeray et al.* (2014, 2015) also showed SCF increasing earlier than observed across boreal forests in CLM4 and, although the snow accumulation period is not a focus in this chapter, processes governing the influence of correction factors are the same as for the snow ablation period. As most snowfall occurs past the boreal autumn equinox, when daily average sub-canopy longwave radiation is increased due to correction factors, correction could delay the accumulation of snow across boreal forests. Therefore, overestimated diurnal cycles in sub-canopy longwave radiation also potentially contribute to this deficiency in the simulation of snow cover timing. A change in calculation of SCF from CLM4 to CLM4.5 introduces uncertainty in projections from CLM4 to CLM4.5, however, impact of this change on snow cover in boreal forests appears to be minor (*Swenson and Lawrence*, 2012).

Changing seasonality in a warming climate may have implications for snowmelt and longwave enhancement. Future warming will lead to earlier snowmelt, when less energy from insolation is available for melt, which will likely result in lower melt rates (*Musselman et al.*, 2017). A shortened snow season indicates more asymmetrical lengths of day and night during snowmelt and consequently, overestimated diurnal cycles of sub-canopy longwave radiation in CLM4.5 could result in even higher underestimations in daily averages. Moreover, underestimated sub-canopy longwave radiation suggests that CLM4.5 underestimates melt rates in general. In turn, future projections are complex, as corrected and thus increased sub-canopy longwave radiation might cancel out reduced energy from insolation due to earlier snowmelt. Nonetheless, the contribution of longwave enhancement to snowmelt is likely to increase in the future, further necessitating accurate simulation of sub-canopy longwave radiation.

Implementation of correction factors resulted in realistic average diurnal ranges of sub-canopy longwave radiation and longwave enhancement, but more substantial underestimation than overestimation of longwave enhancement seen in Figure 5.6 suggests that the impact of shortcomings in CLM4.5 on snow cover and snowmelt might still be underestimated by this study. *Gouttevin et al.* (2015) and findings in Chapter 4 have shown the implementation of biomass heat storage to result in a net positive impact on sub-canopy longwave radiation as well as a slight reduction of diurnal cycles. This suggests that heat storage by biomass could further reduce nighttime underestimation in CLM4.5 and improve the simulation of sub-canopy longwave radiation and longwave enhancement.

5.5 Conclusions

In this chapter, the impact of deficiencies in simulated longwave enhancement by forest canopies on snow cover in CLM4.5 has been assessed. Sub-canopy longwave radiation simulated by CLM4.5's single-layer vegetation was corrected based on the damping effect of multiple canopy layers. Correction factors were derived from forest stand-scale simulations and subsequently implemented for evergreen needleleaf trees in offline (land-only) simulations of CLM4.5. Correction reduces overestimated diurnal cycles of sub-canopy longwave radiation by decreasing daytime overestimations and nighttime underestimations. This results in a net increase of sub-canopy longwave radiation over the entire snow cover season, due to longer nights than days. Consequently, correction results in increasing average snow temperatures, which indicates that CLM4.5 underestimates snow temperatures due to overestimated diurnal cycles of sub-canopy longwave radiation. Simulations exhibit a spatially uniform underestimation of snow temperatures by CLM4.5 across evergreen boreal forests. However, impact on meltout timing displays spatial differences that depend on insolation and duration of snow on the ground. The effect of overestimated diurnal cycles on daily average sub-canopy longwave radiation changes throughout the snowmelt season as insolation and length of day increase. Consequently, CLM4.5 delays snowmelt more in regions of warmer snow cover and earlier meltout, which results in a shortened snowmelt season across boreal forests. However, spatial variability in impact on snow cover is limited in offline simulations of CLM4.5 due to a lack of variability in meteorological conditions.

6 Impact of deficient longwave enhancement on snow cover in global coupled land-atmosphere simulations of CLM4.5

Correction of sub-canopy longwave radiation in offline simulations has resulted in increased snow temperatures throughout the snow cover season as well as a general acceleration of meltout across (evergreen) boreal forests. Warmer snow temperatures and changes in ground cover by snow have the potential to influence the atmosphere via energy fluxes from the surface. However, offline simulations feature no coupling to and thus no interaction with the atmosphere. Furthermore, the impact of corrected sub-canopy longwave radiation on snow cover and snowmelt displayed spatial differences despite a lack of temporal and spatial variability in meteorological forcing, which introduces uncertainty about patterns found for offline simulations. Therefore, correction factors were implemented for NEBTs and NETTs in coupled land-atmosphere simulations of the Community Earth System Model version 1.2.2 (CESM1.2.2) in the same manner as described for offline simulations in Chapter 5.1.2. While land component CLM4.5 and atmospheric component Community Atmosphere Model version 5 (CAM5) were freely evolving, time-varying ocean and sea ice conditions were prescribed in accordance with the Atmosphere Model Intercomparison Project (AMIP; *Gates et al.*, 1999; *Taylor et al.*, 2000) using the Hadley Centre Sea Ice and Sea Surface Temperature data set (HadISST; *Rayner et al.*, 2003; *Hurrell et al.*, 2008), which covers the historical period 1850 to 2012. Simulations were limited to the period 1979 to 2005 by AMIP settings (starting 1979) and prescribed data for atmospheric chemistry (ending 2005) and consequently covered snow seasons 1979/80 to 2004/05. Similarly to offline simulations, two model runs, CTRL and CORR, with spatial resolutions of roughly 1° were performed and compared in order to assess the impact of correction on longwave enhancement, snow cover, and snowmelt.

Coupled simulations display higher spatial variability in longwave enhancement compared to offline simulations (Figure 6.1a). Longwave enhancement by evergreen forests over boreal winter and spring is lowest over Europe and the western coast of North America, with longwave enhancement values of about 1.1 in CTRL. Average longwave enhancement values in CTRL range from 1.2 to 1.35 over evergreen boreal forests in central and eastern North America as well as central Siberia and exceed 1.4 in southeastern Siberia. Compared to offline simulations, longwave enhancement values are lower over Europe, western and central Siberia, and the western coast of North America up to Alaska, but longwave enhancement is similar across North American boreal forests and higher in coupled simulations over boreal forests in eastern Siberia. These differences in spatial variability of longwave enhancement are due to higher and more realistic spatial vari-

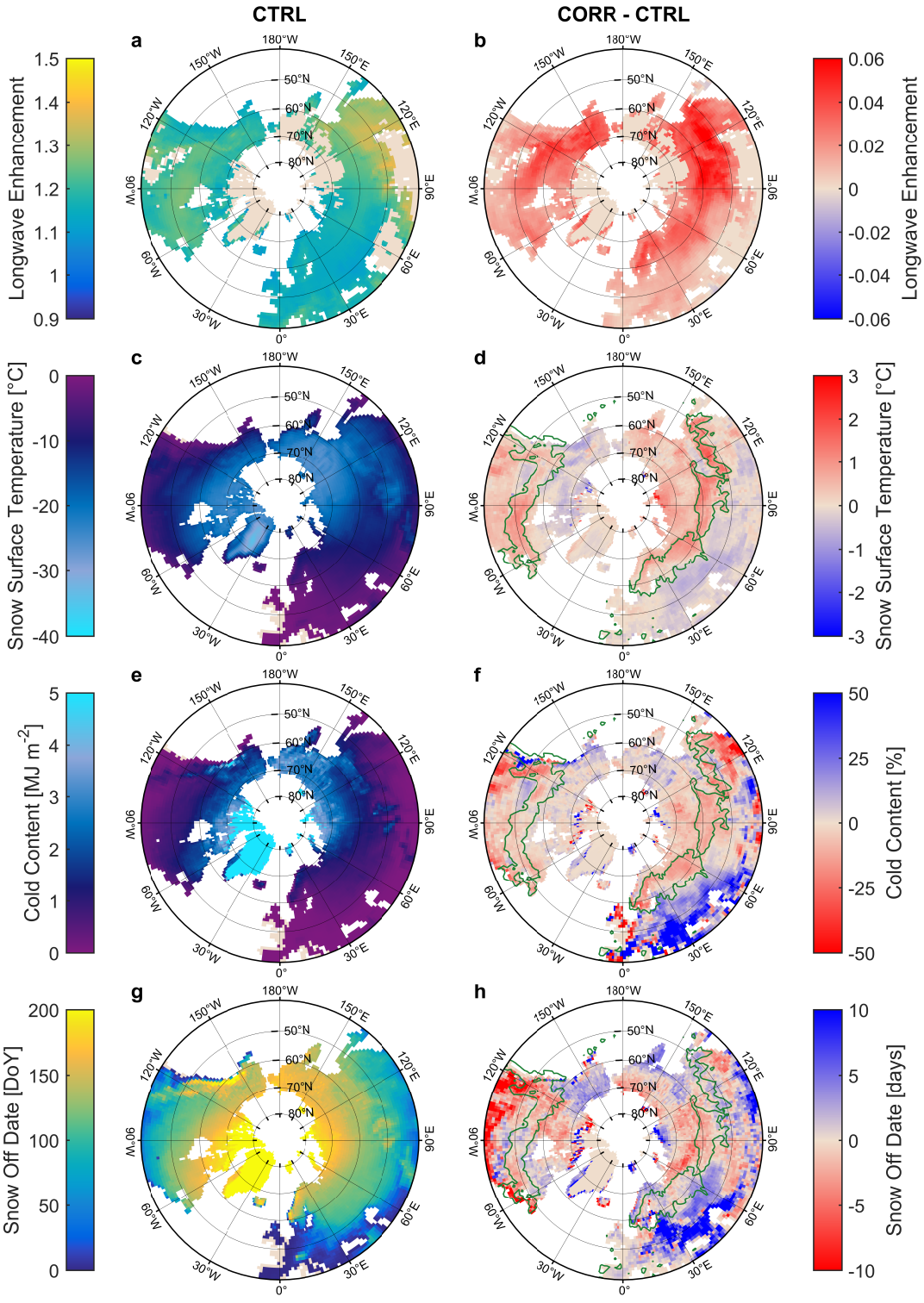

Figure 6.1: Averages in coupled CTRL (**a**, **c**, **e**, **g**) and differences between coupled CORR and coupled CTRL (**b**, **d**, **f**, **h**) for longwave enhancement beneath evergreen needleleaf trees (**a**, **b**), snow surface temperature (**c**, **d**), cold content (**e**, **f**), and snow off date (**g**, **h**). Longwave enhancement is averaged over December to May while snow surface temperature and cold content are averaged over entire snow cover seasons. Differences CORR - CTRL are calculated as averages of differences between each individual snow cover season. For panels **c**-**h**, a mask is applied to filter out grid cells that are not perennially snow-covered. Green lines demarcate areas with coverage by evergreen needleleaf trees of at least 50%.

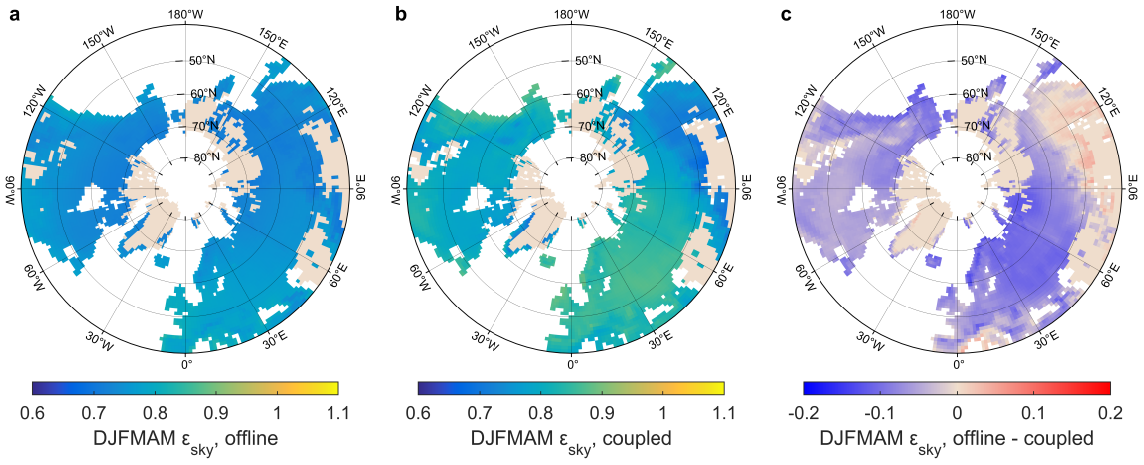

Figure 6.2: Averages over December to May for effective emissivity of the sky in offline simulation CTRL (**a**) and coupled simulation CTRL (**b**) as well as difference between offline and coupled simulation (**c**). Averages are calculated over all years available for the particular simulation but only for grid cells that feature NEBTs and/or NETTs. Note that the range of colours corresponds to the range of ε_{sky} measured at the forest stand near Alptal, Switzerland (Figure 5.6).

ability of ε_{sky} in coupled simulations, which indicates a more realistic representation of meteorological conditions (Figure 6.2). While offline simulations only display a range in average ε_{sky} of about 0.7 to 0.8 with slightly higher ε_{sky} over western Eurasia than eastern Eurasia, average ε_{sky} in coupled simulations reaches up to 0.9 over Europe while falling below 0.7 in southeastern Siberia. Similarly, spatial differences in ε_{sky} are increased over North America in coupled simulations compared to offline simulations.

Higher spatial variability in meteorological conditions also features a distinct influence on the impact of correction on longwave enhancement in coupled simulations (Figure 6.1b). While the change in longwave enhancement from CTRL to CORR displayed a clear latitudinal dependence in offline simulations, as insolation was the major driver due to the lack of variability in ε_{sky}, continentality displays a higher impact than latitude for coupled simulations. Longwave enhancement is higher in coupled CORR than coupled CTRL across snow-covered areas of the Northern Hemisphere, but increases range from less than 0.02 over central and eastern Europe as well as mid-latitude North America to 0.06 in eastern Siberia. Across Eurasia, there is a clear increase in change of longwave enhancement from west to east, while change in longwave enhancement increases from east to west across boreal forests in North America. Spatial differences in both longwave enhancement and increase of longwave enhancement due to correction are in accordance with spatial variability of meteorological conditions, which highlights the theoretical background of vegetation enhancing longwave radiation that is described in Chapter 2.1.

Coupled CTRL displays the same patterns in snow surface temperature and cold content

compared to offline CTRL (Figures 6.1c and 6.1e, respectively), but snow temperatures are generally warmer in coupled simulations, especially over Europe, western Siberia, and central and eastern North America. Across evergreen boreal forests, snow surface temperatures increase from coupled CTRL to coupled CORR (Figure 6.1d). These increases range from less than 0.5°C over northeastern Europe and western North America to about 2°C in southeastern Siberia and increase with clearer skies. Cold content is reduced from coupled CTRL to coupled CORR with less spatial differences across evergreen boreal forests than for snow surface temperature (Figure 6.1f). Reductions in cold content are less than 10% over North American evergreen boreal forests, apart from the west coast where reductions reach up to 30%, and range from 10% to 15% over Eurasian evergreen boreal forests. In comparison to offline simulations, changes in snow surface temperature and cold content due to correction are smaller over Europe, western Siberia, and eastern North America, as meteorological conditions are more overcast and consequently, longwave enhancement values are smaller. Changes in snow surface temperature and cold content are similar over central Siberia and slightly larger over eastern Siberia in coupled simulations compared to offline simulations. In contrast to offline simulations, coupling to the atmosphere results in an impact of correction on snow temperatures in regions with little or no coverage by evergreen needleleaf forests. Correction generally results in increasing (decreasing) snow surface temperatures north (south) of evergreen boreal forests over Eurasia and decreasing (increasing) snow surface temperatures north (south) of evergreen boreal forests over North America. Largest relative changes in cold content can be seen for mid-latitudes, despite a lack of evergreen needleleaf forests, due to small total values of cold content. Relative changes in cold content broadly exhibit the same pattern seen for snow surface temperature, but spatial variability is enhanced due to spatial differences in total cold content.

Higher snow temperatures in coupled simulations compared to offline simulations translate to snow off date (Figure 6.1g), as warmer snow leads to earlier meltout, which might explain earlier reduction of snow cover fraction across boreal forests in coupled simulations than in offline simulations (*Thackeray et al.*, 2014, 2015). While relative reductions in cold content from CTRL to CORR translated to earlier snow off dates for offline simulations, this is not consistently the case for coupled simulations (Figure 6.1h). Meltout is advanced by 2 to 5 days over boreal forests in western North America and central Siberia, which is in agreement with reductions of cold content and increasing snow surface temperatures. However, meltout is slightly delayed over boreal forests in central North America and slightly accelerated over boreal forests in eastern North America, although relative reductions in cold content are consistent across these regions. Meltout

over boreal forests in northeastern Europe and western Siberia displays both slight accelerations and slight delays due to correction in coupled simulations, despite consistent increases in snow surface temperatures and consistent reductions in cold content. Meltout is slightly delayed over boreal forests in eastern Siberia due to correction despite substantially increasing snow surface temperatures and reduction of cold content. There is a clear latitudinal dependence of change in meltout from CTRL to CORR over boreal forests in central and eastern Siberia, which is reminiscent of the impact seen in offline simulations. As clear-sky conditions are prevalent over these regions in both coupled and offline simulations, correction factors are largely determined by insolation and comparable between simulation types. Over regions with little or no coverage by evergreen needleleaf forests, changes in meltout from CTRL to CORR broadly agree with relative changes in cold content, which indicates a consistent impact of changes in meteorological forcing on snow cover.

Changes in snow off dates from coupled CTRL to coupled CORR are too small for a substantial influence on deficient snow cover timing found by *Thackeray et al.* (2014, 2015). However, quantifying the impact of corrected sub-canopy longwave radiation on snow cover is less straightforward for coupled simulations compared to offline simulations due to the interaction between land and atmosphere. Multiple variables that differ between coupled CTRL and coupled CORR affect snow cover and their impacts interfere with each other. Firstly, correction changes sub-canopy longwave radiation and leads to changes in snow temperature and subsequently in ground cover by snow. Secondly, snow cover interacts with the atmosphere and changes in snow surface temperature or fractional snow cover can lead to differences in meteorological forcing between CTRL and CORR, which subsequently affect snow cover. Thirdly, correction changes above-canopy longwave radiation and thus interaction with the atmosphere, which can also lead to a change in meteorological forcing that subsequently affects snow cover. Therefore, it is hard to disentangle the effect on snow cover due to changes in sub-canopy longwave radiation from the effect due to changes in meteorological forcing. Moreover, there is less translation of patterns from snow temperatures to snow off dates for coupled simulations than for offline simulations. This might suggest a higher impact of changing meteorology than of corrected longwave enhancement as meltout is a rather immediate quantity compared to average snow temperatures, in the sense that a single snowfall event can delay meltout by several days, while snow surface temperature and cold content averaged over the entire snow season are not affected much by a single event. Nevertheless, snow surface temperature is generally underestimated and cold content is generally overestimated over boreal forests in coupled simulations.

In order to highlight this agreement between offline and coupled simulations, changes in snow surface temperature, cold content, and snow off date from coupled CTRL to coupled CORR are compared against coverage by evergreen needleleaf forests (Figure 6.3). There is a clear increase in snow surface temperature difference between CORR and CTRL with higher coverage by evergreen needleleaf forests, which indicates increased sub-canopy longwave radiation dominates the impact on snow surface temperature beneath forests in comparison to changes in meteorological forcing. This translates from snow surface temperatures to cold content, which displays a clear increase in difference between CTRL and CORR with coverage by evergreen needleleaf forests. Absolute reduction in average cold content reaches roughly 0.15 MJm^{-2} for forest coverage higher than 90%, which equates to relative reductions ranging from 10% to 15% seen in Figure 6.1f. Although increasing snow surface temperature and decreasing cold content do not clearly result in earlier snow off date, there is a slight decrease in meltout difference between CORR and CTRL with higher coverage by evergreen needleleaf forests, which indicates an increasing impact of sub-canopy longwave radiation on grid cell-wide snowmelt. While magnitudes of increases in snow temperatures are generally lower for coupled simulations than for offline simulations, as more overcast conditions lead to less underestimation of longwave enhancement, and spatial variability is enhanced in coupled simulations due to more realistic meteorological forcing, offline and coupeld simulations agree in general underestimation of snow temperatures by CLM4.5 due to overestimated diurnal cycles of sub-canopy longwave radiation.

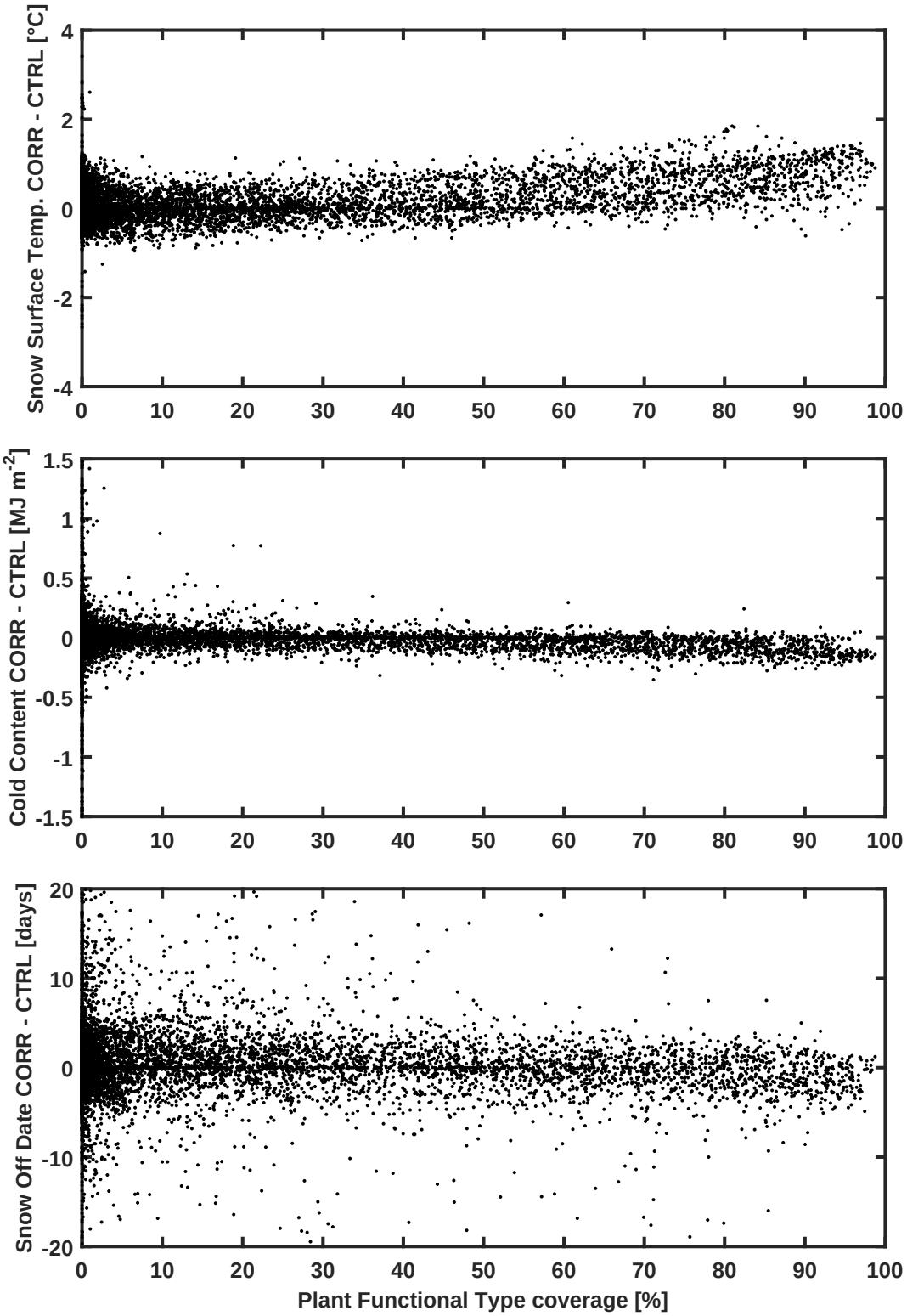

Figure 6.3: Differences between coupled CORR and coupled CTRL as a function of coverage by evergreen needleleaf trees for snow surface temperature (**top panel**), cold content (**centre panel**), and snow off date (**bottom panel**). Differences CORR - CTRL are calculated as averages of differences between each individual snow cover season with snow surface temperature and cold content being averages over entire snow cover seasons. Each data point represents one grid cell of the land-covered Northern Hemisphere. Absolute differences in cold content are shown in contrast to Figure 6.1.

7 Discussion and outlook

Shortwave radiation generally provides a higher energy input to the surface energy balance than longwave radiation, however, the importance of radiation components changes throughout a snow season (*Wang et al.*, 2015). Longwave radiation can determine snowmelt within forests when melt occurs early (*Sicart et al.*, 2004; *Strasser et al.*, 2011; *Lundquist et al.*, 2013) and when snow albedo is high (*Yamazaki and Kondo*, 1992; *Sicart et al.*, 2004), as enhancement of longwave radiation by forest canopies outweighs shading under these conditions. Despite this influence of sub-canopy longwave radiation on snowmelt and lower skill in modelling snow cover for forested than open areas (*Essery et al.*, 2009; *Rutter et al.*, 2009), simulation of sub-canopy longwave radiation and its impact on snowmelt by global climate models had not been assessed so far. As warming will result in an earlier onset of snowmelt, when less energy is available due to lower solar elevation angles, melt rates are likely to decrease in the future (*Musselman et al.*, 2017). Consequently, longwave radiation should become a more prominent driver of snowmelt, which further emphasizes the need for accurate simulation of sub-canopy longwave radiation in global climate models.

Studies have so far demonstrated the enhancement of longwave radiation beneath forest canopies for individual forest stands and/or short observation periods (*Rowlands et al.*, 2002; *Sicart et al.*, 2004; *Essery et al.*, 2008; *Pomeroy et al.*, 2009; *Howard and Stull*, 2013; *Webster et al.*, 2016b). Gathering measurements of sub-canopy longwave radiation in order to assess simulations also allowed for a comparison of longwave enhancement across varying vegetation types and densities as well as over changing meteorological conditions. This comparison shows a clear dependence of longwave enhancement on cloudiness, approximated by effective emissivity of the sky. Longwave enhancement increases continuously for decreasing cloudiness at each forest stand indicating that canopy coverage damps variations in longwave radiation and shelters lower canopy components and the ground. Longwave enhancement values increase from about 1 for overcast conditions, demonstrating little to no effect of the vegetation, to varying values for clear skies. The slope of this curve depends on vegetation density, which scales the respective contributions from atmosphere and vegetation so that longwave enhancement increases with vegetation density for constant cloudiness. However, forest stands at Alptal and Seehornwald display little difference in longwave enhancement for the same range of effective emissivity of the sky as canopies are sufficiently dense to contribute almost exclusively to sub-canopy longwave radiation. Smaller values of effective emissivity of the sky at Seehornwald result in higher maximum values of longwave enhancement compared to Alptal, which reach up to 2 representing a doubling of atmospheric forcing. Even at the (largely)

deciduous forest stands of Borden and Yakutsk, longwave enhancement can reach hourly averages of 1.6 indicating longwave radiation is a substantial contribution to the surface energy balance beneath forest canopies.

Deciduous or predominately deciduous forest stands, as in the case of Borden, cover a wide range of vegetation density, from sparse, small trees at Abisko to tall, rather dense trees at Yakutsk, and consequently, clear-sky longwave enhancement values range from 1.2 up to 1.6, respectively. However, measurements were available from only three evergreen coniferous forest stands, two of which feature high vegetation densities, and longwave enhancement values reported in past studies can help fill gaps in the spectrum of vegetation density. Longwave enhancement values reach up to 1.4 for clear skies at the medium-density pine forest near Sodankylä, which is supported by measurements in North American pine forest stands. Clear-sky longwave enhancement values of 1.2 to 1.4 and little to no longwave enhancement for overcast days have been found for similar vegetation densities compared to Sodankylä (*Rowlands et al.*, 2002; *Essery et al.*, 2008). Additionally, measurements from a Canadian spruce forest revealed mean daytime longwave enhancement values of about 1.5 for clear-sky conditions (*Sicart et al.*, 2004). Both longwave enhancement as well as the plant area index (PAI) value given for this forest stand, 3.3 $\mathrm{m^2 m^{-2}}$, lie in between those for Sodankylä and the two dense Swiss forest stands, thus confirming the dependence of longwave enhancement on vegetation density.

Single-layer vegetation schemes have been found to overestimate diurnal cycles in sub-canopy longwave radiation (*Gouttevin et al.*, 2015), which was confirmed for the Community Land Model version 4.5 (CLM4.5) across forest stands. Diurnal cycles of sub-canopy longwave radiation are overestimated by CLM4.5 for all vegetation types and densities, with daytime overestimations and nighttime underestimations being similar in magnitude, indicating a substantial deficiency in representing vegetation by a single layer. In reality, forest canopies shade lower components of the vegetation, which in turn do not heat up as much as the uppermost components that are directly exposed to insolation, while the canopy shelters lower components from radiative cooling at night. Therefore, vertical vegetation structure, in addition to suppressed turbulent fluxes, is crucial in limiting diurnal variations in vegetation temperatures, sub-canopy air temperatures, and consequently in sub-canopy longwave radiation. Representation of vegetation by a single layer eliminates the effect of upper on lower vegetation components and consequently, the single vegetation layer passes on the atmospheric signal to the ground without much damping, as the vegetation layer is directly exposed to atmospheric forcing while the ground is directly exposed to the vegetation layer. Decreasing cloudiness leads to increasing diurnal variations in meteorological forcing, due to increasing insolation and nighttime cooling,

which result in increasing diurnal cycles of sub-canopy longwave radiation simulated by the single-layer vegetation. In contrast, observed diurnal ranges of sub-canopy longwave radiation do not show substantial differences between overcast and clear-sky conditions and consequently, simulation errors increase for clearer skies highlighting the lack of shading and sheltering of a single-layer vegetation. As longwave enhancement values are highest for clear skies, simulation errors increase the more important the impact of canopy cover becomes. Simulation errors also increase with vegetation density, since atmospheric longwave radiation is an input variable to CLM4.5 and vegetation density determines contributions to sub-canopy longwave radiation from atmosphere and vegetation. Consequently, simulation errors are emphasized for dense forests and under clear skies, which are conditions that generally apply to boreal forests in CLM4.5.

Vegetation density appears to impact how vegetation responds to meteorological forcing, which necessitates a correct representation of vegetation and its density in climate models. Observations indicate higher ranges of vegetation temperatures at sparse sites compared to dense sites, reaffirming past observational studies (*Rowlands et al.*, 2002; *Pomeroy et al.*, 2009; *Webster et al.*, 2016a). In contrast, CLM4.5 simulates similar ranges in vegetation temperatures across forest stands (except for Abisko, for which evaluation period is limited to 9 days). This indicates that vegetation density is crucial in sheltering lower vegetation components by damping meteorological forcing, with sparse canopies being less able to self-shade and insulate sufficiently, and suggests that single-layer vegetation simulates a behaviour of sparser canopies even when vegetation density is high.

The two-layer version of SNOWPACK had been calibrated using data from Alptal (*Gouttevin et al.*, 2015) and was used for comparison with CLM4.5 for forest stands at Alptal, Seehornwald, and Sodankylä without adjustment of calibration parameters. Although differences in vegetation density compared to Alptal led to biases for Seehornwald and Sodankylä, SNOWPACK consistently simulated a small spread in sub-canopy longwave radiation, contrasting simulations by CLM4.5. This signifies the consistent impact of the upper on the lower layer by shading and sheltering from radiative cooling, which is highlighted by a substantially smaller diurnal cycle of vegetation temperatures simulated by SNOWPACK compared to CLM4.5 even at the low-density forest stand near Sodankylä.

A means to affect the response of vegetation temperatures to meteorological forcing is the parameterization of thermal inertia due to biomass, which is not included in CLM4.5. Implementation of biomass heat storage was found to reduce simulation errors as cooling in the afternoon and at night is delayed, which results in a net increase of sub-canopy longwave radiation. However, cooling is not delayed sufficiently in order to stop underestimations of nighttime sub-canopy longwave radiation and consequently, biomass heat

storage has little impact on overestimated diurnal ranges. *Gouttevin et al.* (2015) tested the impact on sub-canopy longwave radiation due to implementing biomass heat storage and subdividing vegetation into two separate layers in SNOWPACK and noted that biomass had to be overestimated in the one-layer version to optimize model performance. However, impact of biomass heat storage on model performance was minimal for the two-layer version. This confirms what has been found for CLM4.5 in test runs of the Toy Model used in this thesis. Biomass heat storage reduces the overestimated diurnal cycle of sub-canopy longwave radiation, but physically realistic values are not sufficient to correct simulation errors due to single-layer vegetation. Diurnal cycles are further reduced when exceeding measured values for biomass, however, they are also further delayed, which eventually results in a decrease of model skill. Moreover, the net positive impact of biomass on sub-canopy longwave radiation additionally reduces model skill when exceeding physically realistic values of biomass. For a multi-layer vegetation, diurnal cycles in sub-canopy longwave radiation are already reduced by the sheltering upper layer(s), so that biomass mostly affects the timing rather than the amplitude of diurnal cycles.

Assessment of forest stand-scale simulations revealed systematic errors in sub-canopy longwave radiation simulated by the single-layer vegetation in CLM4.5. In order to quantify the impact of this deficiency on snow cover, sub-canopy longwave radiation was corrected in global simulations of CLM4.5. Development and implementation of a second vegetation layer in addition to stand-scale studies was beyond the scope of this thesis and generally leads to considerably increased computational costs, which necessitated a shortcut to avoid changing energy balance calculations of the vegetation and deterioration of model performance. An empirical correction was developed based on the systematic dependence of simulation errors on insolation and cloudiness, which are the major governing variables. This reiterates the shading and sheltering effect of a multi-layer canopy and its consequent damping of variations in sub-canopy longwave radiation and highlights that, although a simple scaling, correction is based on physical processes.

Similar vegetation densities of forest stand and grid cell in CLM4.5 allow for a comparison of longwave enhancement at Alptal. This comparison showed that correction succeeded in scaling the diurnal range of sub-canopy longwave radiation to a realistic value, reducing both daytime overestimations and nighttime underestimations. While stand-scale simulations revealed similar magnitudes of overestimations and underestimations by CLM4.5's single-layer vegetation, longer nights than days throughout the snow cover season result in nighttime underestimations outweighing daytime overestimations. For Alptal, this amounted to an underestimation of daily average sub-canopy longwave radiation by about 5 Wm^{-2} over the snowmelt season, which is the equivalent of 1.3 mm

of snow water equivalent melting over a day or $20\mathrm{cm}$ of snow water equivalent being warmed by $1\ \mathrm{K}$ over a day. Averaged over the snow cover season, nighttime underestimations outweigh daytime overestimations of sub-canopy longwave radiation across temperate and boreal forests, which results in a uniform underestimation of average snow surface temperatures in land-only simulations. However, this does not translate to a spatially constant delay of meltout, as impact on meltout depends on when snowmelt occurs. The impact of overestimated diurnal cycles on daily averages of sub-canopy longwave radiation changes throughout the snow cover season as lengths of day and night vary and consequently, the immediate impact on snow cover changes throughout the snow season. The majority of the snow cover season is confined by autumn and spring equinoxes, with longer nights than days and consequently nighttime underestimations outweighing daytime overestimations. For snowmelt that occurs prior to the spring equinox, daily average sub-canopy longwave radiation is consistently underestimated by CLM4.5 and meltout is delayed. Past the spring equinox, daytime overestimations can outweigh nighttime underestimations, which leads to overestimated daily averages of sub-canopy longwave radiation that eventually begin to cancel out the impact of underestimated sub-canopy longwave radiation prior to the spring equinox. Consequently, delay of meltout in land-only simulations decreases with later occurrence of snowmelt, and overestimated sub-canopy longwave radiation past the spring equinox can eventually result in accelerated meltout despite an underestimation of snow temperatures averaged over the entire snow cover season. Simply put, the average night is longer than the average day while snow is on the ground, which leads to a net underestimation of sub-canopy longwave radiation due to single-layer vegetation and thus to underestimated energy input to snow in CLM4.5. The consequent impact on meltout depends on whether days or nights are longer during the snowmelt season. Early snowmelt occurs while nights are longer than days, so that energy input is underestimated and meltout is substantially delayed. When snowmelt happens past the spring equinox, days are longer than nights and consequently, energy input is overestimated and meltout can eventually be accelerated due to the single-layer vegetation.

The impact of single-layer vegetation on snowmelt and its spatial differences indicate a varying effect on melt rates by the single-layer vegetation in CLM4.5. The highest impact of deficient simulation of sub-canopy longwave radiation on snowmelt in land-only simulations is found for regions where snowmelt occurs early. Longwave radiation contributes to a higher degree to early snowmelt when solar angles are still low (*Sicart et al.*, 2004; *Strasser et al.*, 2011; *Lundquist et al.*, 2013). This suggests that CLM4.5 might generally underestimate melt rates in forests but underestimations are highest early in the snowmelt

season. Moreover, forest coverage has been found to accelerate snowmelt compared to open areas in regions of warm winters where mid-winter melt events happen (*Lundquist et al.*, 2013), and CLM4.5 might underestimate those melt events due to underestimated energy input to snow during winter. As snowmelt will occur earlier in a warmer world, energy input to snow will change and likely result in reduced melt rates (*Musselman et al.*, 2017), which is supported by observations of snow water equivalent over the period 1980-2017 (*Wu et al.*, 2018). Earlier snowmelt will occur at times when solar angles are lower, so that energy input will be reduced and longwave radiation will become more important. As earlier snowmelt also implies more asymmetrical lengths of night and day during the snowmelt season, overestimated diurnal cycles of sub-canopy longwave radiation are likely to result in a higher underestimation of sub-canopy longwave radiation and thus further underestimated melt rates.

Spatial differences in impact of overestimated diurnal cycles of sub-canopy longwave radiation on meltout indicate a shortened snowmelt season across boreal forests in land-only simulations. Both CLM4 and CCSM4, precursor versions of CLM4.5 and CESM1.2, respectively, display a deficient simulation of meltout timing across boreal forests (*Thackeray et al.*, 2014, 2015). CLM4 overestimates meltout from March to May and underestimates meltout before and after that period, representing a shortened snowmelt season. Overestimated diurnal cycles of sub-canopy longwave radiation can cause a compressed snowmelt duration and could therefore contribute to the deficient simulation of meltout timing. Similarly, snow accumulation in autumn occurs too early across boreal forests in CLM4 and CCSM4 (*Thackeray et al.*, 2014, 2015). As snow accumulation occurs past the autumn equinox, overestimated diurnal cycles of sub-canopy longwave radiation result in an underestimation of energy input and might thus accelerate snow accumulation, potentially contributing to this deficiency in simulation of snow cover timing as well.

Land-only simulations use prescribed meteorological forcing, which displays a lack of both spatial and temporal variability in meteorological conditions. In turn, longwave enhancement and the diurnal range of sub-canopy longwave radiation display little spatial variability, and spatial differences in impact on snow cover and snowmelt are solely due to location (latitude and insolation) and time of year. As prescribed meteorological conditions indicate rather clear skies on average, simulated diurnal cycles of sub-canopy longwave radiation are generally high and result in substantially underestimated snow temperatures. In order to assess the impact of overestimated diurnal cycles of sub-canopy longwave radiation under more realistic meteorological forcing, the correction was implemented in coupled simulations. These display higher and more realistic spatial variability in meteorological conditions, with more overcast skies in Europe and western Siberia

as well as at both coasts of North America. Generally, differences in average cloudiness across Eurasia as well as across North America are higher in coupled simulations than in land-only simulations. Consequently, underestimation of longwave enhancement by CLM4.5 displays more spatial variability, with less underestimation in more overcast regions, and is generally lower compared to land-only simulations. Nevertheless, longwave enhancement is underestimated by CLM4.5 across the snow-covered Northern Hemisphere in coupled and land-only simulations, and underestimation of longwave enhancement is only slightly reduced from land-only to coupled simulations over boreal forests in eastern Siberia and over much of North America. This confirms findings of land-only simulations that CLM4.5 underestimates the energy input to snow in boreal forests due to overestimated diurnal cycles of sub-canopy longwave radiation.

Identifying the impact of correction on snow cover is less straightforward for coupled simulations compared to land-only simulations. It is difficult to disentangle the effect on snow cover due to corrected sub-canopy longwave radiation from the effect due to changes in meteorological forcing that result from interaction between land and atmosphere. The impact of correction on snow temperature features lower magnitudes for coupled simulations, due to mostly smaller longwave enhancement values, as well as enhanced spatial variability due to more realistic meteorological conditions. Nevertheless, snow surface temperatures are clearly underestimated and cold content is clearly overestimated in land-only simulations and coupled simulations over boreal forests in Siberia and eastern North America. Again, this confirms findings of land-only simulations that underestimated energy input from forest cover results in underestimated snow temperatures.

Despite underestimated snow temperatures across boreal forests, snow off dates do not show a spatially consistent delay in coupled simulations. Magnitudes in delay or acceleration of meltout are higher in regions of little or no forest coverage, which suggests a substantial impact of changing meteorology on snow cover that interferes with the impact of corrected sub-canopy longwave radiation. Nevertheless, correction generally results in advanced meltout for densely forested regions in coupled simulations, indicating some translation of corrected sub-canopy longwave radiation into acceleration of snow off date. In contrast to land-only simulations, correction of sub-canopy longwave radiation does not clearly indicate a shortened snowmelt season across boreal forests in coupled simulations, which is due to higher spatial variability of meteorological conditions. This is in accordance with differences in snow cover timing across boreal forests that had been found for land-only CLM4 and coupled CCSM4 (*Thackeray et al.*, 2014, 2015).

The change in meteorological forcing due to implementation of correction in coupled simulations is likely not only caused by changes in snow temperature and fractional snow

cover. In order to conserve energy without changing the vegetation energy balance, sub-canopy longwave radiation was corrected by redistributing longwave radiation emitted from vegetation upward and downward. In doing so, diurnal variability in sub-canopy longwave radiation was reduced and consequently, diurnal variability in above-canopy longwave radiation was enhanced. However, an upper(most) canopy layer likely does not exhibit higher variations in emitted longwave radiation than the single vegetation layer, since both are exposed to atmospheric forcing to the same degree. Therefore, total longwave radiation emitted from actual multi-layer vegetation, i.e. upward plus downward, likely differs from longwave radiation emitted from a single layer, and the vertical average temperature of multi-layer vegetation differs from the temperature of single-layer vegetation. While this has an impact on the atmosphere and subsequently on meteorological forcing in coupled simulations, it does not affect land-only simulations, as longwave radiation emitted upward is not used in any form. Consequently, land-only simulations solely display changes in snow cover due to corrected sub-canopy longwave radiation. The correction developed in this thesis instantaneously redistributes energy vertically, which guarantees conservation of energy. However, forest canopies feature a temporal redistribution via shading and sheltering, as lower layers take longer to react to meteorological forcing, as well as via thermal inertia due to biomass. Without multiple vegetation layers to delay the atmospherical signal passing through to the ground, heat storage via biomass is the only physical means to delay the reaction of vegetation temperatures while conserving energy. However, biomass alone is not sufficient to create physically realistic diurnal cycles. While unrealistically high values of biomass can be used to scale diurnal ranges of sub-canopy longwave radiation to realistic values, thermal inertia consequently causes unrealistically delayed diurnal cycles and eventually results in decreasing model skill. This reaffirms findings for SNOWPACK that show realistic values of biomass have little impact on diurnal ranges of sub-canopy longwave radiation (*Gouttevin et al.*, 2015) and indicates multiple vegetation layers are indispensable in order to sufficiently simulate sub-canopy and above-canopy longwave radiation.

While implementation of the correction resulted in realistic diurnal ranges of sub-canopy longwave radiation, comparison of global simulations and forest stand measurements for the location of Alptal suggests that diurnal cycles of sub-canopy longwave radiation are still slightly overestimated and daily averages could be underestimated. Implementation of heat storage by biomass results in slightly reduced diurnal ranges and a net increase of sub-canopy longwave radiation, reaffirming findings by *Gouttevin et al.* (2015). Therefore, the combination of biomass and multiple layers could resolve the deficient simulation of sub-canopy longwave radiation. Past studies have already explored advancing

the complexity of vegetation representation in CLM by subdividing the roughness layer, which improved the simulation of both turbulent fluxes and radiative temperature (*Bonan et al.*, 2014, 2018). Forests can act as cold air sinks due to reduced wind speed and thus suppressed turbulent fluxes (*Price*, 1988; *Link and Marks*, 1999b; *Webster et al.*, 2016a), which is crucial as air temperature is the major driver of snowmelt. However, vertical profiles of air temperature within the canopy space cannot be resolved by a single-layer vegetation. Moreover, vertical vegetation structure has been found to impact interception by forest canopies and consequent evaporation and sublimation of snow, which further indicates the necessity of multiple vegetation layers in land models (*McGowan et al.*, 2016). Therefore, this study contributes to the growing evidence of limitations in modelling vegetation as a single layer by assessing the deficiency in simulated longwave enhancement and consequent impact on snow cover and snowmelt while expanding from stand-scale studies.

8 Summary

Boreal forests cover about a fifth of perennially snow-covered land over the Northern Hemisphere. Therefore, assessment of vegetation-snow-atmosphere processes in global climate models is important for accurate simulation of global snow cover. One of these processes is the enhancement of longwave radiation beneath forest canopies, which has been found to impact the surface energy balance and rates of snowmelt. Forest canopies exhibit an enhancement of longwave radiation for clear skies, when atmospheric longwave radiation decreases and insolation heats up the vegetation, and little to no effect for overcast conditions. These variations in longwave enhancement result in damped variability of longwave radiation reaching the ground beneath forest canopies compared to open areas. Measurements across several forest stands show hourly values of longwave enhancement of up to 2, i.e. a doubling of sub-canopy compared to atmospheric longwave radiation, beneath dense, evergreen forests and hourly values of up to 1.6 even beneath dense, (predominately) deciduous forests. This reaffirms the importance of longwave enhancement for the surface energy balance beneath forest canopies and indicates that longwave enhancement is a crucial process across boreal forest types.

Although skill in modelling snow cover has been shown to be lower for forests than for open areas, model intercomparisons and evaluations of model parameterizations have not yet focused on longwave enhancement. Single-layer vegetation schemes have been found to overestimate diurnal cycles in radiative temperature and sub-canopy longwave radiation, however, the consequent impact on snow cover and longwave enhancement on a global scale is still unknown. A global model that represents vegetation by a single layer is Community Land Model version 4.5 (CLM4.5), the land component of National Center for Atmospheric Research's (NCAR) Community Earth System Model (CESM) version 1.2, whose precursor version was part of Climate Model Intercomparison Project's fifth phase (CMIP5) suite of models. In order to assess the simulation of longwave enhancement by CLM4.5, forcing and evaluation data were aggregated for forest stands of varying vegetation types, structures, and densities across perennially snow-covered regions. CLM4.5 is found to overestimate diurnal cycles of sub-canopy longwave radiation and longwave enhancement with overestimations during day and underestimations during night that display similar magnitudes. Simulation errors increase with vegetation density, which determines contributions from vegetation and atmosphere to sub-canopy longwave radiation, and decrease with increasing cloudiness. As insolation and radiative cooling at night increase for clearer skies, this dependency of simulation errors indicates a lack of self-shading and sheltering by single-layer vegetation. While implementation of biomass heat storage improves simulations, realistic values of biomass are not sufficient to cor-

rect the overestimated diurnal range of sub-canopy longwave radiation. In contrast to CLM4.5, SNOWPACK, a one-dimensional snow model with a two-layer forest canopy, is found to simulate realistic diurnal ranges of sub-canopy longwave radiation and longwave enhancement across the range of vegetation density.

Based on the systematic simulation errors revealed by stand-scale simulations of CLM4.5, a correction was developed that scales sub-canopy longwave radiation by redistributing upward and downward longwave radiation emitted from vegetation. Subsequently, the correction was implemented for evergreen forests in CLM4.5 in order to quantify the impact of deficient longwave enhancement on snow cover in global simulations. CLM4.5 underestimates longwave enhancement over the snow cover season across boreal and temperate forests, as longer nights than days lead to nighttime underestimation outweighing daytime overestimation. Consequently, energy input to snow cover and snow temperatures are underestimated across forests, which is found for both land-only and coupled simulations of CLM4.5. Underestimation of snow temperatures generally causes delayed meltout, but impact on snowmelt differs spatially depending on meteorological conditions and duration of snow on the ground. More overcast conditions lead to less longwave enhancement and thus to less underestimation of longwave enhancement by CLM4.5. Early snowmelt occurs during winter, when nights are substantially longer than days, which results in a substantial underestimation of daily average longwave enhancement. This suggests that mid-winter melt events, when solar angles are low and longwave enhancement outweighs shading by forest canopies, might be underestimated by CLM4.5. As future warming will result in earlier melt and more asymmetric lengths of day and night during snowmelt, this deficiency is likely to become more important. Insolation and day length increase throughout the snowmelt season and consequently, daytime overestimations of longwave enhancement eventually outweigh nighttime underestimations. This results in spatial differences in impact of overestimated diurnal cycles of longwave enhancement on meltout, which suggests a deficient duration of snowmelt across forests in CLM4.5. Overall, single-layer vegetation results in underestimation of longwave enhancement over the snow season and consequently in underestimated snow temperatures and a general delay of meltout beneath forests in CLM4.5. Therefore, this study strengthens the case for representation of vegetation by multiple layers in global climate models.

References

Alexander, H. D., M. C. Mack, S. Goetz, M. M. Loranty, P. S. A. Beck, K. Earl, S. Zimov, S. Davydov, and C. C. Thompson (2012), Carbon Accumulation Patterns During Post-Fire Succession in Cajander Larch (Larix cajanderi) Forests of Siberia, *Ecosystems*, *15*(7), 1065–1082, doi:10.1007/s10021-012-9567-6.

Bartelt, P., and M. Lehning (2002), A physical SNOWPACK model for the Swiss avalanche warning Part I: Numerical model, *Cold Regions Science and Technology*, *35*(3), 123–145, doi:10.1016/S0165-232X(02)00074-5.

Bartlett, P. A., and D. L. Verseghy (2015), Modified treatment of intercepted snow improves the simulated forest albedo in the Canadian Land Surface Scheme, *Hydrological Processes*, *29*, 3208–3226, doi:10.1002/hyp.10431.

Betts, A. K., and J. H. Ball (1997), Albedo over the boreal forest, *Journal of Geophysical Research: Atmospheres*, *102*(D24), 28,901–28,909, doi:10.1029/96JD03876.

Bonan, G. B., S. Levis, L. Kergoat, and K. W. Oleson (2002), Landscapes as patches of plant functional types: An integrating concept for climate and ecosystem models, *Global Biogeochemical Cycles*, *16*(2), 5.1–5.23, doi:10.1029/2000GB001360.

Bonan, G. B., M. Williams, R. A. Fisher, and K. W. Oleson (2014), Modeling stomatal conductance in the earth system: linking leaf water-use efficiency and water transport along the soil–plant–atmosphere continuum, *Geoscientific Model Development*, *7*(5), 2193–2222, doi:10.5194/gmd-7-2193-2014.

Bonan, G. B., E. G. Patton, I. N. Harman, K. W. Oleson, J. J. Finnigan, Y. Lu, and E. A. Burakowski (2018), Modeling canopy-induced turbulence in the Earth system: a unified parameterization of turbulent exchange within plant canopies and the roughness sublayer (CLM-ml v0), *Geoscientific Model Development*, *11*(4), 1467–1496, doi:10.5194/gmd-11-1467-2018.

Boone, A., P. Samuelsson, S. Gollvik, A. Napoly, L. Jarlan, E. Brun, and B. Decharme (2017), The interactions between soil–biosphere–atmosphere land surface model with a multi-energy balance (ISBA-MEB) option in SURFEXv8 – Part 1: Model description, *Geoscientific Model Development*, *10*(2), 843–872, doi:10.5194/gmd-10-843-2017.

Brutel-Vuilmet, C., M. Ménégoz, and G. Krinner (2013), An analysis of present and future seasonal Northern Hemisphere land snow cover simulated by CMIP5 coupled climate models, *The Cryosphere*, *7*, 67–80, doi:10.5194/tc-7-67-2013.

Chen, F., M. Barlage, M. Tewari, R. Rasmussen, J. Jin, D. Lettenmaier, B. Livneh, C. Lin, G. Miguez-Macho, G.-Y. Niu, L. Wen, and Z.-L. Yang (2014), Modeling seasonal snowpack evolution in the complex terrain and forested Colorado Headwaters region: A model intercomparison study, *Journal of Geophysical Research: Atmospheres*, *119*(24), 13,795–13,819, doi:10.1002/2014JD022167.

Chen, Y., J. Ryder, V. Bastrikov, M. J. McGrath, K. Naudts, J. Otto, C. Ottlé, P. Peylin, J. Polcher, A. Valade, A. Black, J. A. Elbers, E. Moors, T. Foken, E. van Gorsel, V. Haverd, B. Heinesch, F. Tiedemann, A. Knohl, S. Launiainen, D. Loustau, J. Ogée, T. Vessala, and S. Luyssaert (2016), Evaluating the performance of land surface model ORCHIDEE-CAN v1.0 on water and energy flux estimation with a single- and multi-layer energy budget scheme, *Geoscientific Model Development*, *9*(9), 2951–2972, doi:10.5194/gmd-9-2951-2016.

Croft, H., J. M. Chen, N. J. Froelich, B. Chen, and R. M. Staebler (2015), Seasonal controls of canopy chlorophyll content on forest carbon uptake: Implications for GPP modeling, *Journal of Geophysical Research G: Biogeosciences*, *120*(8), 1576–1586, doi:10.1002/2015JG002980.

Derksen, C., and R. Brown (2012), Spring snow cover extent reductions in the 2008–2012 period exceeding climate model projections, *Geophysical Research Letters*, *39*, L19,504, doi:10.1029/2012GL053387.

Ellis, C. R., J. W. Pomeroy, T. Brown, and J. MacDonald (2010), Simulation of snow accumulation and melt in needleleaf forest environments, *Hydrology and Earth System Sciences*, *14*, 925–940, doi:10.5194/hess-14-925-2010.

Essery, R. (2013), Large-scale simulations of snow albedo masking by forests, *Geophysical Research Letters*, *40*, 5521–5525, doi:10.1002/grl.51008.

Essery, R. (2015), A factorial snowpack model (FSM 1.0), *Geoscientific Model Development*, *8*, 3867–3876, doi:10.5194/gmd-8-3867-2015.

Essery, R., J. Pomeroy, C. Ellis, and T. Link (2008), Modelling longwave radiation to snow beneath forest canopies using hemispherical photography or linear regression, *Hydrological Processes*, *22*, 2788–2800, doi:10.1002/hyp.6930.

Essery, R., N. Rutter, J. Pomeroy, R. Baxter, M. Stähli, D. Gustafsson, A. Barr, P. Bartlett, and K. Elder (2009), SnowMIP2: An evaluation of forest snow process simulation, *Bulletin of the American Meteorological Society*, *90*(8), 1130–1135, doi:10.1175/2009BAMS2629.1.

Essery, R., S. Morin, Y. Lejeune, and C. B. Ménard (2013), A comparison of 1701 snow models using observations from an alpine site, *Advances in Water Resources*, *55*, 131–148, doi:10.1016/j.advwatres.2012.07.013.

Essery, R., A. Kontu, J. Lemmetyinen, M. Dumont, and C. B. Ménard (2016), A 7-year dataset for driving and evaluating snow models at an Arctic site (Sodankylä, Finland), *Geoscientific Instrumentation, Methods and Data Systems*, *5*(1), 219–227, doi:10.5194/gi-5-219-2016.

Flanner, M. G., and C. S. Zender (2005), Snowpack radiative heating:Influence on Tibetan Plateau climate, *Geophysical Research Letters*, *32*, L06,501, doi:10.1029/2004GL022076.

Flanner, M. G., K. M. Shell, M. Barlage, D. K. Perovich, and M. A. Tschudi (2011), Radiative forcing and albedo feedback from the Northern Hemisphere cryosphere between 1979 and 2008, *Nature Geoscience*, *4*, 151–155, doi:10.1038/NGEO1062.

Flato, G., J. Marotzke, B. Abiodun, P. Braconnot, S. C. Chou, W. Collins, P. Cox, F. Driouech, S. Emori, V. Eyring, C. Forest, P. Gleckler, E. Guilyardi, C. Jakob, V. Kattsov, C. Reason, and M. Rummukainen (2013), Evaluation of Climate Models , in *Climate Change 2013: The Physical Science Basis. Contribution of Working Group I to the Fifth Assessment Report of the Intergovernmental Panel on Climate Change*, edited by T. F. Stocker, D. Qin, G.-K. Plattner, M. Tignor, S. K. Allen, J. Boschung, A. Nauels, Y. Xia, V. Bex, and P. M. Midgley, Cambridge University Press, Cambridge, United Kingdom and New York, NY, USA.

Froelich, N., H. Croft, J. M. Chen, A. Gonsamo, and R. M. Staebler (2015), Trends of carbon fluxes and climate over a mixed temperate-boreal transition forest in southern Ontario, Canada, *Agricultural and Forest Meteorology*, *211-212*, 72–84, doi:10.1016/j.agrformet.2015.05.009.

Gates, W. L., J. S. Boyle, C. Covey, C. G. Dease, C. M. Doutriaux, R. S. Drach, M. Fiorino, P. J. Gleckler, J. J. Hnilo, S. M. Marlais, T. J. Phillips, G. L. Potter, B. D. Santer, K. R. Sperber, K. E. Taylor, and D. N. Williams (1999), An Overview of the Results of the Atmospheric Model Intercomparison Project (AMIP I), *Bulletin of the American Meteorological Society*, *80*(1), 29–56.

Gent, P. R., G. Danabasoglu, L. J. Donner, M. M. Holland, E. C. Hunke, S. R. Jayne, D. M. Lawrence, R. B. Neale, P. J. Rasch, M. Vertenstein, P. H. Worley, Z.-L. Yang,

and M. Zhang (2011), The Community Climate System Model Version 4, *Journal of Climate*, *24*, 4973–4991, doi:10.1175/2011JCLI4083.1.

Giesbrecht, M. A., and M. Woo (2000), Simulation of snowmelt in a subarctic spruce woodland: 2. Open woodland model, *Water Resources Research*, *36*(8), 2287–2295, doi:10.1029/2000WR900093.

Gouttevin, I., M. Lehning, T. Jonas, D. Gustafsson, and M. Mölder (2015), A two-layer canopy model with thermal inertia for an improved snowpack energy balance below needleleaf forest (model SNOWPACK, version 3.2.1, revision 741), *Geoscientific Model Development*, *8*, 2379–2398, doi:10.5194/gmd-8-2379-2015.

Hancock, S., R. Essery, T. Reid, J. Carle, R. Baxter, N. Rutter, and B. Huntley (2014), Characterising forest gap fraction with terrestrial lidar and photography: An examination of relative limitations, *Agricultural and Forest Meteorology*, *189–190*, 105–114, doi:10.1016/j.agrformet.2014.01.012.

Harding, R. J., and J. W. Pomeroy (1996), The energy balance of the winter boreal landscape, *Journal of Climate*, *9*(11), 2778–2787, doi:10.1175/1520-0442(1996)009⟨2778:TEBOTW⟩2.0.CO;2.

Hardy, J. P., R. E. Davis, R. Jordan, X. Li, C. Woodcock, W. Ni, and J. C. McKenzie (1997), Snow ablation modeling at the stand scale in a boreal jack pine forest, *Journal of Geophysical Research: Atmospheres*, *102*, 29,397–29,405, doi:10.1029/96JD03096.

Hedstrom, N. R., and J. W. Pomeroy (1998), Measurements and modelling of snow interception in the boreal forest, *Hydrological Processes*, *12*, 1611–1625, doi:10.1002/(SICI)1099-1085(199808/09)12:10/11⟨1611::AID-HYP684⟩3.0.CO;2-4.

Henderson-Sellers, A., A. J. Pitman, P. K. Love, P. Irannejad, and C. T. H. (1995), The Project for Intercomparison of Land Surface Parameterization Schemes (PILPS): Phases 2 and 3, *Bulletin of the American Meteorological Society*, *76*(4), 489–503.

Howard, R., and R. Stull (2013), IR Radiation from Trees to a Ski Run: A Case Study, *Journal of Applied Meteorology and Climatology*, *52*, 1525–1539, doi:10.1175/JAMC-D-12-0222.1.

Hurrell, J. W., J. J. Hack, D. Shea, J. M. Caron, and J. Rosinski (2008), A New Sea Surface Temperature and Sea Ice Boundary Dataset for the Community Atmosphere Model, *Journal of Climate*, *21*(19), 5145–5153, doi:10.1175/2008JCLI2292.1.

Jeffries, M. O., J. E. Overland, and D. K. Preovich (2013), The Arctic shifts to a new normal, *Physics Today*, *66*(10), 35–40, doi:10.1063/PT.3.2147.

Keller, H. M., and T. Strobel (1977), Predicting snow accumulation under subalpine forest stands, in *Proceedings of the Joint Scientific Meeting on Mountain Meteorology and Biometeorology*, pp. 87–104, AMS, SGBB, SSG, 10-14 June 1976. Interlaken, Switzerland.

Kropp, H. (2018), Siberian boreal forest energy balance (ViPER project), Cherskiy, Sakha Republic, Russia, 2016 - 2017, doi:10.18739/A2BG2H890.

Lafaysse, M., B. Cluzet, M. Dumont, Y. Lejeune, V. Vionnet, and S. Morin (2017), A multiphysical ensemble system of numerical snow modelling, *Cryosphere*, *11*(3), 1173–1198, doi:10.5194/tc-11-1173-2017.

Lawrence, P. J., and T. N. Chase (2007), Representing a new MODIS consistent land surface in the Community Land Model (CLM 3.0), *Journal of Geophysical Research: Biogeosciences*, *112*(G1), doi:10.1029/2006JG000168.

Lehning, M., P. Bartelt, B. Brown, C. Fierz, and P. Satyawali (2002a), A physical SNOWPACK model for the Swiss avalanche warning Part II. Snow microstructure, *Cold Regions Science and Technology*, *35*(3), 147–167, doi:10.1016/S0165-232X(02)00073-3.

Lehning, M., P. Bartelt, B. Brown, and C. Fierz (2002b), A physical SNOWPACK model for the Swiss avalanche warning Part III: Meteorological forcing, thin layer formation and evaluation, *Cold Regions Science and Technology*, *35*(3), 169–184, doi:10.1016/S0165-232X(02)00072-1.

Li, Y., T. Wang, Z. Zeng, S. Peng, X. Lian, and S. Piao (2016), Evaluating biases in simulated land surface albedo from CMIP5 global climate models, *Journal of Geophysical Research: Atmospheres*, *121*(11), 6178–6190, doi:10.1002/2016JD024774.

Link, T., and D. Marks (1999a), Distributed simulation of snowcover mass- and energy-balance in the boreal forest, *Hydrological Processes*, *13*, 2439–2452, doi:10.1002/(SICI)1099-1085(199910)13:14/15⟨2439::AID-HYP866⟩3.0.CO;2-1.

Link, T. E., and D. Marks (1999b), Point simulation of seasonal snow cover dynamics beneath boreal forest canopies, *Journal of Geophysical Research: Atmospheres*, *104*, 27,841–27,857, doi:10.1029/1998JD200121.

Loranty, M. M., L. T. Berner, S. J. Goetz, Y. Jin, and J. T. Randerson (2014), Vegetation controls on northern high latitude snow-albedo feedback: observations and CMIP5 model simulations, *Global Change Biology*, *20*, 594–606, doi:10.1111/gcb.12391.

Lundquist, J. D., S. E. Dickerson-Lange, J. A. Lutz, and N. C. Cristea (2013), Lower forest density enhances snow retention in regions with warmer winters: A global framework developed from plot-scale observations and modeling, *Water Resources Research*, *49*, 6356–6370, doi:10.1002/wrcr.20504.

McGowan, L., K. T. Paw U, H. Dahlke, S.-H. Chen, and D. Pyles (2016), The Effect of the Vertical Canopy Structure on Snow Processes Scenarios: Simulations of the Vertical Resolved Energy Fluxes and Snow Using a Higher-Order Closure Multi-Layer Soil-Vegetation-Atmospheric Model, in *84th Annual Western Snow Conference, Seattle, Washington, USA*, https://westernsnowconference.org/files/PDFs/2016McGowan.pdf.

McGrath, M. J., J. Ryder, B. Pinty, J. Otto, K. Naudts, A. Valade, Y. Chen, J. Weedon, and S. Luyssaert (2016), A multi-level canopy radiative transfer scheme for ORCHIDEE (SVN r2566), based on a domain-averaged structure factor, *Geoscientific Model Development Discussions*, *2016*, 1–22, doi:10.5194/gmd-2016-280.

Moeser, D., M. Stähli, and T. Jonas (2015), Improved snow interception modeling using canopy parameters derived from airborne LiDAR data, *Water Resources Research*, *51*(7), 5041–5059, doi:10.1002/2014WR016724.

Moeser, D., G. Mazzotti, N. Helbig, and T. Jonas (2016), Representing spatial variability of forest snow: Implementation of a new interception model, *Water Resources Research*, *52*(2), 1208–1226, doi:10.1002/2015WR017961.

Mudryk, L. R., P. J. Kushner, and C. Derksen (2014), Interpreting observed northern hemisphere snow trends with large ensembles of climate simulations, *Climate Dynamics*, *43*, 345–359, doi:10.1007/s00382-013-1954-y.

Mudryk, L. R., P. J. Kushner, C. Derksen, and C. Thackeray (2017), Snow cover response to temperature in observational and climate model ensembles, *Geophysical Research Letters*, *44*(2), 919–926, doi:10.1002/2016GL071789.

Musselman, K. N., M. P. Clark, C. Liu, K. Ikeda, and R. Rasmussen (2017), Slower snowmelt in a warmer world, *Nature Climate Change*, *7*(3), 214–219, doi:10.1038/nclimate3225.

Neumann, H. H., G. Den Hartog, and R. H. Shaw (1989), Leaf area measurements based on hemispheric photographs and leaf-litter collection in a deciduous forest during autumn leaf-fall, *Agricultural and Forest Meteorology*, *45*(3-4), 325–345, doi: 10.1016/0168-1923(89)90052-X.

Ohta, T., T. Hashimoto, and H. Ishibashi (1990), Basic study on the effects of forests for the surface snow melt, *Journal of the Japanese Society of Snow and Ice*, *52*, 289–296, doi:10.5331/seppyo.52.289.

Ohta, T., T. Hiyama, H. Tanaka, T. Kuwada, T. C. Maximov, T. Ohata, and Y. Fukushima (2001), Seasonal variation in the energy and water exchanges above and below a larch forest in eastern Siberia, *Hydrological Processes*, *15*(8), 1459–1476, doi:10.1002/hyp.219.

Oleson, K. W., D. M. Lawrence, G. B. Bonan, B. Drewniak, M. Huang, C. D. Koven, S. Levis, F. Li, W. J. Riley, Z. M. Subin, S. C. Swenson, P. E. Thornton, A. Bozbiyik, R. Fisher, E. Kluzek, J.-F. Lamarque, P. J. Lawrence, L. R. Leung, W. Lipscomb, S. Muszala, D. M. Ricciuto, W. Sacks, Y. Sun, J. Tang, and Z.-L. Yang (2013), Technical Description of version 4.5 of the Community Land Model (CLM), *Tech. rep.*, National Center for Atmospheric Research, doi:10.5065/D6RR1W7M.

Perket, J., M. Flanner, D. Lawrence, and M. Clark (2015), Reducing CLM Albedo Biases in Snow-Effected Forests with Improved Canopy Scheme, in *Land Model and Biogeochemistry Working Group Meeting*, http://www.cesm.ucar.edu/events/wg-meetings/2015/presentations/bgcwg+lmwg/perket.pdf.

Pithan, F., and T. Mauritsen (2014), Arctic amplification dominated by temperature feedbacks in contemporary climate models, *Nature Geoscience*, *7*, 181–184, doi: 10.1038/NGEO2071.

Pomeroy, J. W., D. M. Gray, K. R. Shook, B. Toth, R. L. H. Essery, A. Pietroniro, and N. Hedstrom (1998), An evaluation of snow accumulation and ablation processes for land surface modelling, *Hydrological Processes*, *12*, 2339–2367, doi:10.1002/(SICI)1099-1085(199812)12:15⟨2339::AID-HYP800⟩3.0.CO;2-L.

Pomeroy, J. W., D. M. Gray, N. R. Hedstrom, and J. R. Janowicz (2002), Prediction of seasonal snow accumulation in cold climate forests, *Hydrological Processes*, *16*(18), 3543–3558, doi:10.1002/hyp.1228.

Pomeroy, J. W., D. Marks, T. Link, C. Ellis, J. Hardy, A. Rowlands, and R. Granger (2009), The impact of coniferous forest temperature on incoming longwave radiation to melting snow, *Hydrological Processes*, *23*, 2513–2525, doi:10.1002/hyp.7325.

Price, A. G. (1988), Prediction of snowmelt rates in a deciduous forest, *Journal of Hydrology*, *101*(1), 145–157, doi:10.1016/0022-1694(88)90032-7.

Qu, X., and A. Hall (2007), What Controls the Strength of Snow-Albedo Feedback?, *Journal of Climate*, *20*(15), 3971–3981, doi:10.1175/JCLI4186.1.

Qu, X., and A. Hall (2014), On the persistent spread in snow-albedo feedback, *Climate Dynamics*, *42*(1), 69–81, doi:10.1007/s00382-013-1774-0.

Rayner, N. A., D. E. Parker, E. B. Horton, C. K. Folland, L. V. Alexander, D. P. Rowell, E. C. Kent, and A. Kaplan (2003), Global analyses of sea surface temperature, sea ice, and night marine air temperature since the late nineteenth century, *Journal of Geophysical Research: Atmospheres*, *108*(D14), doi:10.1029/2002JD002670.

Reid, T. D., R. L. H. Essery, N. Rutter, and M. King (2014a), Data-driven modelling of shortwave radiation transfer to snow through boreal birch and conifer canopies, *Hydrological Processes*, *28*(6), 2987–3007, doi:10.1002/hyp.9849.

Reid, T. D., M. Spencer, B. Huntley, S. Hancock, R. L. H. Essery, J. Carle, R. Holden, R. Baxter, and N. Rutter (2014b), Spatial quantification of leafless canopy structure in a boreal birch forest, *Agricultural and Forest Meteorology*, *188*, 1–12, doi:10.1016/j.agrformet.2013.12.005.

Robinson, D. A., and G. Kukla (1985), Maximum Surface Albedo of Seasonally Snow-Covered Lands in the Northern Hemisphere, *Journal of Climate and Applied Meteorology*, *24*(5), 402–411, doi:10.1175/1520-0450(1985)024⟨0402:MSAOSS⟩2.0.CO;2.

Roesch, A. (2006), Evaluation of surface albedo and snow cover in AR4 coupled climate models, *Journal of Geophysical Research: Atmospheres*, *111*(D15), doi:10.1029/2005JD006473.

Rowlands, A., J. Pomeroy, J. Hardy, D. Marks, K. Elder, and R. Melloh (2002), Small-Scale Spatial Variability of Radiant Energy for Snowmelt in a Mid-Latitude Sub-Alpine Forest, in *Proceedings of the 59th Eastern Snow Conference*, pp. 109–117, Stowe, Vermont, USA, available online at http://www.easternsnow.org/proceedings/2002/010_Rowlands.pdf.

Rupp, D. E., P. W. Mote, N. L. Bindoff, P. A. Stott, and D. A. Robinson (2013), Detection and Attribution of Observed Changes in Northern Hemisphere Spring Snow Cover, *Journal of Climate*, *26*, 6904–6914, doi:10.1175/JCLI-D-12-00563.1.

Rutter, N., R. Essery, J. Pomeroy, N. Altimir, K. Andreadis, I. Baker, A. Barr, P. Bartlett, A. Boone, H. Deng, H. Douville, E. Dutra, K. Elder, C. Ellis, X. Feng, A. Gelfan, A. Goodbody, Y. Gusev, D. Gustafsson, R. Hellström, Y. Hirabayashi, T. Hirota, T. Jonas, V. Koren, A. Kuragina, D. Lettenmaier, W.-P. Li, C. Luce, E. Martin, O. Nasonova, J. Pumpanen, R. D. Pyles, P. Samuelsson, M. Sandells, G. Schädler, A. Shmakin, T. G. Smirnova, M. Stähli, R. Stöckli, U. Strasser, H. Su, K. Suzuki, K. Takata, K. Tanaka, T. Thompson, E. Vesala, P. Viterbo, A. Wiltshire, K. Xia, Y. Xue, and T. Yamazaki (2009), Evaluation of forest snow processes models (SnowMIP2), *Journal of Geophysical Research: Atmospheres*, *114*, D06,111, doi:10.1029/2008JD011063.

Ryder, J., J. Polcher, P. Peylin, C. Ottlé, Y. Chen, E. van Gorsel, V. Haverd, M. J. McGrath, K. Naudts, J. Otto, A. Valade, and S. Luyssaert (2016), A multi-layer land surface energy budget model for implicit coupling with global atmospheric simulations, *Geoscientific Model Development*, *9*(1), 223–245, doi:10.5194/gmd-9-223-2016.

Schmidt, R. A., and D. R. Gluns (1991), Snowfall interception on branches of three conifer species, *Canadian Journal of Forest Research*, *21*(8), 1262–1269, doi:10.1139/x91-176.

Sellers, P. J. (1985), Canopy reflectance, photosynthesis and transpiration, *International Journal of Remote Sensing*, *6*(8), 1335–1372, doi:10.1080/01431168508948283.

Sicart, J. E., J. W. Pomeroy, R. L. H. Essery, J. Hardy, T. Link, and D. Marks (2004), A Sensitivity Study of Daytime Net Radiation during Snowmelt to Forest Canopy and Atmospheric Conditions, *Journal of Hydrometeorology*, *5*(5), 774–784, doi:10.1175/1525-7541(2004)005⟨0774:ASSODN⟩2.0.CO;2.

Stähli, M., and D. Gustafsson (2006), Long-term investigations of the snow cover in a subalpine semi-forested catchment, *Hydrological Processes*, *20*(2), 411–428, doi:10.1002/hyp.6058.

Stähli, M., T. Jonas, and D. Gustafsson (2009), The role of snow interception in wintertime radiation processes of a coniferous sub-alpine forest, *Hydrological Processes*, *23*, 2498–2512, doi:10.1002/hyp.7180.

Storck, P., D. P. Lettenmaier, and S. M. Bolton (2002), Measurement of snow interception and canopy effects on snow accumulation and melt in a mountainous maritime climate, Oregon, United States, *Water Resources Research*, *38*(11), 5–1–5–16, doi: 10.1029/2002WR001281.

Strasser, U., M. Warscher, and G. E. Liston (2011), Modeling snow-canopy processes on an idealized mountain, *Journal of Hydrometeorology*, *12*(4), 663–677, doi:10.1175/2011JHM1344.1.

Suzuki, K., and T. Ohta (2003), Effect of Larch Forest Density on Snow Surface Energy Balance, *Journal of Hydrometeorology*, *4*(6), 1181–1193, doi:10.1175/1525-7541(2003)004⟨1181:EOLFDO⟩2.0.CO;2.

Suzuki, R., K. Yoshikawa, and T. C. Maximov (2001), Pheonological photographs of Siberian larch forest from 1997 to 2000 at Spasskaya Pad, Republic of Sakha, Russia, http://www.jamstec.go.jp/iorgc/hcorp/data/database/products/phenol/index.htm (Internet website distribution).

Swenson, S. C., and D. M. Lawrence (2012), A new fractional snow-covered area parameterization for the Community Land Model and its effect on the surface energy balance, *Journal of Geophysical Research: Atmospheres*, *117*(D21), doi:10.1029/2012JD018178.

Taylor, K. E., D. L. Williamson, and F. Zwiers (2000), AMIP II Sea Surface Temperature and Sea Ice Concentration Boundary Conditions, *PCMDI Report*, *60*.

Teklemariam, T., R. M. Staebler, and A. G. Barr (2009), Eight years of carbon dioxide exchange above a mixed forest at Borden, Ontario, *Agricultural and Forest Meteorology*, *149*(11), 2040–2053, doi:10.1016/j.agrformet.2009.07.011.

Thackeray, C. W., C. G. Fletcher, and C. Derksen (2014), The influence of canopy snow parameterizations on snow albedo feedback in boreal forest regions, *Journal of Geophysical Research: Atmospheres*, *119*, 9810–9821, doi:10.1002/2014JD021858.

Thackeray, C. W., C. G. Fletcher, and C. Derksen (2015), Quantifying the skill of CMIP5 models in simulating seasonal albedo and snow cover evolution, *Journal of Geophysical Research: Atmospheres*, *120*, 5831–5849, doi:10.1002/2015JD023325.

Thackeray, C. W., C. G. Fletcher, L. R. Mudryk, and C. Derksen (2016), Quantifying the Uncertainty in Historical and Future Simulations of Northern Hemisphere Spring Snow Cover, *Journal of Climate*, *29*(23), 8647–8663, doi:10.1175/JCLI-D-16-0341.1.

Todt, M., N. Rutter, C. G. Fletcher, L. M. Wake, P. A. Bartlett, T. Jonas, H. Kropp, M. M. Loranty, and C. Webster (2018), Simulation of Longwave Enhancement in Boreal and Montane Forests, *Journal of Geophysical Research: Atmospheres*, *123*(24), 13,731–13,747, doi:10.1029/2018JD028719.

Todt, M., N. Rutter, C. G. Fletcher, and L. M. Wake (2019), Simulated single-layer forest canopies delay Northern Hemisphere snowmelt, *The Cryosphere Discussions*, doi:10.5194/tc-2018-270, in review.

Viovy, N. (2018), CRUNCEP Version 7 - Atmospheric Forcing Data for the Community Land Model, Research Data Archive at the National Center for Atmospheric Research, Computational and Information Systems Laboratory, http://rda.ucar.edu/datasets/ds314.3/, Accessed 01 May 2018.

Wang, L., C. Derksen, R. Brown, and T. Markus (2013), Recent changes in pan-Arctic melt onset from satellite passive microwave measurements, *Geophysical Research Letters*, *40*, 522–528, doi:10.1002/grl.50098.

Wang, L., J. N. S. Cole, P. Bartlett, D. Verseghy, C. Derksen, R. Brown, and K. von Salzen (2016), Investigating the spread in surface albedo for snow-covered forests in CMIP5 models, *Journal of Geophysical Research: Atmospheres*, *121*, doi:10.1002/2015JD023824.

Wang, T., S. Peng, C. Ottlé, and P. Ciais (2015), Spring snow cover deficit controlled by intraseasonal variability of the surface energy fluxes, *Environmental Research Letters*, *10*(2), 024,018, doi:10.1088/1748-9326/10/2/024018.

Webster, C., N. Rutter, F. Zahner, and T. Jonas (2016a), Modeling subcanopy incoming longwave radiation to seasonal snow using air and tree trunk temperatures, *Journal of Geophysical Research: Atmospheres*, *121*(3), 1220–1235, doi:10.1002/2015JD024099.

Webster, C., N. Rutter, F. Zahner, and T. Jonas (2016b), Measurement of Incoming Radiation below Forest Canopies: A Comparison of Different Radiometer Configurations, *Journal of Hydrometeorology*, *17*, 853–864, doi:10.1175/JHM-D-15-0125.1.

Woo, M., and M. A. Giesbrecht (2000), Simulation of snowmelt in a subarctic spruce woodland: 1. Tree model, *Water Resources Research*, *36*(8), 2275–2285, doi:10.1029/2000WR900094.

Wu, X., T. Che, X. Li, N. Wang, and X. Yang (2018), Slower Snowmelt in Spring Along With Climate Warming Across the Northern Hemisphere, *Geophysical Research Letters*, *45*(22), 12,331–12,339, doi:10.1029/2018GL079511.

Yamazaki, T. (2001), A one-dimensional land surface model adaptable to intensely cold regions and its applications in Eastern Siberia, *Journal of the Meteorological Society of Japan*, *79*(6), 1107–1118, doi:10.2151/jmsj.79.1107.

Yamazaki, T., and J. Kondo (1992), The snowmelt and heat balance in snow-covered forested areas, *Journal of Applied Meteorology*, *31*(11), 1322–1327, doi:10.1175/1520-0450(1992)031⟨1322:TSAHBI⟩2.0.CO;2.

Yamazaki, T., J. Kondo, T. Watanabe, and T. Sato (1992), A heat-balance model with a canopy of one or two layers and its application to field experiments, *Journal of Applied Meteorology*, *31*(1), 86–103, doi:10.1175/1520-0450(1992)031⟨0086:AHBMWA⟩2.0.CO;2.

Zeng, X., M. Shajkh, Y. Dai, R. E. Dickinson, and R. Myneni (2002), Coupling of the Common Land Model to the NCAR Community Climate Model, *Journal of Climate*, *15*(14), 1832–1854, doi:10.1175/1520-0442(2002)015⟨1832:COTCLM⟩2.0.CO;2.

Zweifel, R., M. Haeni, N. Buchmann, and W. Eugster (2016), Are trees able to grow in periods of stem shrinkage?, *New Phytologist*, *211*(3), 839–849, doi:10.1111/nph.13995.